
Vibration Analysis of the SA349/2 Helicopter

Ruth Heffernan, Dominique Precetti,
and Wayne Johnson

(NASA-TM-102794) VIBRATION ANALYSIS OF THE
SA349/2 HELICOPTER (NASA) 102 p CSCL 01B

N91-31078

G3 Unclass
3/01 0036818

January 1991



Vibration Analysis of the SA349/2 Helicopter

Ruth Heffernan, Dominique Precetti, and Wayne Johnson
Ames Research Center, Moffett Field, California

January 1991



National Aeronautics and
Space Administration

Ames Research Center
Moffett Field, California 94035-1000

VIBRATION ANALYSIS OF THE SA349/2 HELICOPTER

Ruth Heffernan
NASA Ames Research Center

Dominique Precetti
Service Technique des Programmes Aéronautiques

and

Wayne Johnson
Johnson Aeronautics

SUMMARY

Helicopter airframe vibration is examined using calculations and measurements for the SA349/2 research helicopter. The hub loads, which transmit excitations to the fuselage, are predicted using a comprehensive rotorcraft analysis and correlated with measured hub loads. The predicted and measured hub loads are then coupled with finite-element models representing the SA349/2 fuselage. The resulting vertical acceleration at the pilot seat is examined. Adjustments are made to the airframe structural models to examine the sensitivity of predicted vertical acceleration to the model. Changes of a few percent to the damping and frequency of specific modes lead to large reductions in predicted vibration, and to major improvements in the correlations with measured pilot-seat vertical acceleration.

NOMENCLATURE

A_n	cosine coefficient of the n^{th} harmonic
B_n	sine coefficient of the n^{th} harmonic
C	transformation matrix between the aircraft principal axes and F-frame (fig. 1(a))
cg	center of gravity
C_T/σ	thrust coefficient to solidity ratio
F_E	excitation load to fuselage model at the hub, F-frame (fig.1(a)), N

F_{hub}	combined hub load (blade root forces plus hub inertial load), N
$f_{\text{tx}}, f_{\text{ty}}, f_{\text{tz}}$	total rotating frame hub forces, N (fig. 4)
F_X, F_Y, F_Z	total nonrotating frame hub forces, N (fig. 4)
H	drag force at the hub, positive aft, N
i	$\sqrt{-1}$
I_{xx}, I_{yy}, I_{zz}	aircraft principal moments of inertia, kg-m ²
I_{xy}, I_{xz}, I_{yz}	aircraft products of inertia, kg-m ²
m	number of elastic modes
M_{at}	advancing tip Mach number
M_r	rotor mass, kg
$m_{\text{tx}}, m_{\text{ty}}, m_{\text{tz}}$	total rotating frame hub moments, Nm (fig. 4)
M_x	rolling moment, positive roll to the right (pilot's perspective), Nm
M_X, M_Y, M_Z	total nonrotating frame hub moments, Nm (fig. 4)
M_y	pitching moment, positive nose up, Nm
n	harmonic number
Q	torque positive counterclockwise from the top, Nm
q_k	generalized displacement, m
Q_k	generalized forces, N
r	airframe coordinates relative to the cg, F-frame, m
T	rotor thrust, positive up, N
t	time, sec
U	spatial perturbation of a point on the airframe, m
Y	lateral hub force, positive toward the advancing side, N

μ	advance ratio
φ	angular perturbation about the x_F axis, F-frame, rad
θ	angular perturbation about the y_F axis, F-frame, rad
Ω	rotor rotation frequency, rad/s
ω	modal frequency of the structure, rad/s
ξ	translation mode shape vector in the F-frame, m/m
γ	rotation mode shape vector in the F-frame, rad/m
Ψ	blade azimuth angle, measured from the tail boom toward the advancing side of the rotor disk, rad
ψ	angular perturbation about the z_F axis, F-frame, rad
$[]$	matrix
$\{\}$	vector

Subscripts

cg	center of gravity
F	F-frame; body axis system (x_F, y_F, z_F) , (fig. 1(a))
h	hub
k	number of k^{th} mode
p	pilot seat
R	R-frame; rotor axis system (x_R, y_R, z_R) , (fig. 1(b))
r	rigid modes
S	S-frame; shaft axis system (x_S, y_S, z_S) , (fig. 1(c))

1 INTRODUCTION

The ability to calculate fuselage vibration is a major consideration in the design and development of helicopters. Despite large reductions in vibration achieved through improved helicopter designs developed over the past 30 years, the current overall levels (approximately 0.05 to 0.1 g) remain significantly higher than those of jet-engine aircraft, which are below 0.01g (ref. 1). Until production helicopters can achieve comparably low vibration levels, vibration analysis will continue to remain an important topic for rotorcraft.

Many studies of helicopter vibration have been conducted in recent years. Reference 1, a survey of rotorcraft dynamics, summarizes the helicopter vibration problem and methods of vibration control. Other studies have focused on the development and correlation of structural dynamic models, which are required to calculate vibrations (refs. 2,3). These papers state that improved structural models will rely in large part on developing analytical methods of determining the structural damping. A review of helicopter vibration control, discussed in reference 4, points out that modeling the rotor, engine, gearbox, and mounting structure of a fuselage strongly influences the transmission of rotor-hub forces and moments to the airframe. References 5 and 6 discuss vibration control research which has demonstrated the potential for reducing airframe vibrations through higher harmonic control.

To fully address the helicopter vibration problem, the entire system must be examined. In general, rotor airloads cause hub loads, hub loads generate airframe vibrations (neglecting fuselage aerodynamics), and airframe vibrations in turn influence the hub loads. Accurate prediction of vibration relies not only on a fully representative airframe structural model, but also on correct modeling of the rotor aerodynamics and dynamics, and of the rotor/ fuselage coupling.

To the extent possible, this study addressed the complete fuselage vibration problem. The oscillatory hub loads transmitted to the fuselage were predicted using a comprehensive rotorcraft analysis and correlated with the measured hub loads. Finite-element models representing the SA349/2 fuselage were excited by measured and predicted hub loads, and the resulting vertical acceleration at the pilot seat was compared with the measured acceleration. The results revealed both the degree of correlation between predicted and measured hub loads and the accuracy of the fuselage finite-element models for predicting vibration. Minor adjustments were made to the airframe structural models to examine the sensitivity of the predicted vibration.

This research has been carried out under a cooperative agreement between the National Aeronautics and Space Administration (NASA) and the French Ministry of Defense to study the aerodynamic and dynamic behavior of helicopters. SA349/2 helicopter flight test data and current rotorcraft analyses developed in the United States and in France have been used to conduct the studies. Reference 7 includes a summary of previous studies completed through this joint agreement.

2 SA349/2 FLIGHT TEST DATA

The flight test data used in this analysis were obtained from the SA349/2 Gazelle Helicopter. The SA349/2 aircraft, fully described in reference 8, has an advanced geometry main rotor with three Grande Vitesse (high speed) blades. Table 1 lists the general aircraft information, including moments of inertia, shaft angle, and center of gravity location for the helicopter. Reference axes for aircraft loads, shown in figure 1, are the F-frame (body axes), the R-frame (rotor axes), and the S-frame (shaft axes). The instrumentation of interest in this study, shown in figure 2, included six shaft strain gages on the main rotor (see detail in fig. 2) and a vertical accelerometer at the pilot seat. The hub forces and moments were obtained from the rotor shaft strain-gage measurements, as described in reference 9. The pilot-seat accelerometer measured vertical vibration. Table 1 includes the location of the pilot-seat accelerometer. Measurements were made for four level-flight cases and two turning-flight cases. Table 2 lists parameters for these six flight conditions. All six conditions were examined in this study. The measured data were recorded as harmonic series with fundamental frequency Ω , the rotor rotation rate.

3 VIBRATION OF A SINGLE-MAIN-ROTOR HELICOPTER

There are four primary sources of airframe vibration on a single-main-rotor helicopter in steady-state flight: the main rotor, the tail rotor, the engine and the airloads. The main rotor is generally assumed to be the major source of fuselage vibration. As a result, excitations from only the main rotor are considered here. The fuselage is excited by the periodic rotor loads, and the rotor, in turn, is excited by the hub motions. A schematic of this rotor/fuselage coupling is shown in figure 3. In this study, we first predict and correlate the hub loads which cause airframe vibration. We then develop the airframe vibration model, and predict and correlate the vertical acceleration at the pilot seat.

3.1 Hub Loads

In steady-state flight, the blades are subject to a complex flowfield influenced by the rotor wake. The motion of the blades caused by the airloads, the control inputs, and the blade root loads are all functions of azimuth and can be expanded as harmonic series, with fundamental frequency Ω . These periodic aerodynamic and structural loads are summed over all blades to obtain the hub loads. The experimental and theoretical derivation of the hub loads is described below.

3.1.1 Derivation of the Measured Hub Loads– The in-plane rotating frame forces (f_{tx} , f_{ty}) and moments (m_{tx} , m_{ty}) at the hub are calculated from measurements of the shaft-bending moment by assuming the shaft is a beam isolated from other external forces and moments (ref. 9). The x-components are computed from the measured shaft-bending loads, and the y-components are obtained by introducing a 90° phase shift. The corresponding in-plane hub forces and moments in the nonrotating frame (F_X , F_Y , and M_X , M_Y) are obtained through the following coordinate transformation, shown in figure 4:

$$\begin{aligned}
F_X &= f_{tx} \cos(\Psi) + f_{ty} \sin(\Psi) \\
F_Y &= -f_{tx} \sin(\Psi) + f_{ty} \cos(\Psi) \\
M_X &= m_{tx} \cos(\Psi) + m_{ty} \sin(\Psi) \\
M_Y &= -m_{tx} \sin(\Psi) + m_{ty} \cos(\Psi)
\end{aligned} \tag{1}$$

Two other shaft gages measured the rotor thrust and rotor torque, which are the same in both the rotating and fixed frame ($f_{tz} = F_Z$ and $m_{tz} = M_Z$).

When the rotating frame hub loads are computed by summing the root loads over all three blades, only the $3n \pm 1$ harmonics of the in-plane loads (f_{tx} , f_{ty} , m_{tx} , m_{ty}), and the $3n$ harmonics of the out-of-plane loads (f_{tz} and m_{tz}) are nonzero. All other harmonics cancel because of the geometric symmetry of the rotor and the relative angle between the blades. When transforming the in-plane loads (F_X , F_Y and M_X , M_Y) to the nonrotating frame, the $3n + 1$ and $3n - 1$ harmonics combine to yield nonzero $3n$ harmonics only. For the out-of-plane loads, only the $3n$ harmonics exist in either reference frame.

In the nonrotating frame, therefore, the combined hub loads, F_{hub} , can be expressed as a series of complex $3n/\text{rev}$ harmonics and written in the shaft axis system (S-frame) as follows:

$$\{F_{hub}\}_S = F_{hub_0} + \sum_{n=-\infty}^{+\infty} \{A_{3n} \cos(3n\Psi) + B_{3n} \sin(3n\Psi)\} \tag{2}$$

where F_{hub_0} represents the mean hub loads, and A_{3n} and B_{3n} are the harmonic coefficients. The six force and moment components of F_{hub} can be expressed as follows:

$$\{F_{hub}\}_S = \begin{bmatrix} F_X \\ F_Y \\ -F_Z \\ M_X \\ M_Y \\ M_Z \end{bmatrix}_S = \begin{bmatrix} H \\ -Y \\ T \\ -M_x \\ M_y \\ Q \end{bmatrix}_S \tag{3}$$

where the first column of equation 3 shows the sign conventions of the data, while the second column represents the sign conventions for the hub loads of a clockwise rotating rotor (see fig. 5). The measured hub loads, which were obtained up to the 9th harmonic for the six flight conditions listed in table 2, are published in appendix D of reference 9. However, since the largest contribution to the hub loads occurs at the $3/\text{rev}$, only $3/\text{rev}$ hub loads and the corresponding $3/\text{rev}$ fuselage vibrations are examined here. Table 3 lists the harmonic coefficients (cosine and sine) of the $3/\text{rev}$ hub loads, using the nomenclature of figure 5. The corresponding $3/\text{rev}$ pilot-seat vertical acceleration is also listed in table 3 for the six flight conditions.

3.1.2 CAMRAD/JA Hub Loads Analysis– In addition to the measured hub loads, calculated hub loads were also used as excitations in the vibration analysis. Calculations were made using CAMRAD/JA (ref. 10), a comprehensive rotorcraft analysis designed to examine a variety of two-rotor helicopters. In this study, CAMRAD/JA predicted hub loads, which were applied to the fuselage to obtain the pilot-seat accelerations. Care was taken to ensure that the calculated hub loads were consistent with the measured loads, which included inertial forces caused by hub motion. To accomplish this, the mass of the hub was added at the blade roots, simulating the configuration of the measured hub loads.

The CAMRAD/JA model of the SA349/2 was trimmed to each flight condition in free flight. Free-flight trim was achieved by iterating on initial control settings until aircraft force and moment equilibrium was reached. For most cases, two inflow models were used in the analysis: uniform inflow, and nonuniform inflow with prescribed wake geometry. For the lowest speed condition, a nonuniform inflow, free wake geometry model was used. The CAMRAD/JA analysis modeled each blade with five bending and three torsion modes. Predictions were made for cases both with and without feedback of the fuselage motion to the rotor, in order to evaluate the sensitivity of hub loads to hub motion.

3.2 Fuselage Vibration Analysis

Having identified the hub loads responsible for the airframe vibration, we will now identify and model this vibratory behavior. The purpose here is to compute the spatial perturbations at the pilot seat U_p , the hub U_h , and the center of gravity U_{cg} , which can be written in the F-frame as

$$\{U_p\} = \begin{bmatrix} x_p \\ y_p \\ z_p \\ \phi_p \\ \theta_p \\ \psi_p \end{bmatrix}_F \quad \{U_h\} = \begin{bmatrix} x_h \\ y_h \\ z_h \\ \phi_h \\ \theta_h \\ \psi_h \end{bmatrix}_F \quad \{U_{cg}\} = \begin{bmatrix} x_{cg} \\ y_{cg} \\ z_{cg} \\ \phi_{cg} \\ \theta_{cg} \\ \psi_{cg} \end{bmatrix}_F$$

The structure considered in a helicopter modal analysis generally includes the fuselage and a concentrated mass at the hub to account for the rotor inertia. The classical eigenvalue representation was used to model the fuselage. The motion of a structure can be described by six rigid modes and an infinite number of elastic modes. However, the high frequency modes do not contribute significantly to the body motion. As a result, only the low frequency modes are essential for developing a structural model. Finite-element modal analysis was used to predict the low frequency modal degrees of freedom.

The rigid and elastic motion of a body is described by a second-order matrix equation for the body degrees of freedom. This system equation can be normalized, neglecting damping, using eigen analysis to determine the generalized displacements, q_k , where k is the mode number.

The normalized system can be excited by generalized external forces, Q_k . By subsequently adding proportional damping to the normalized system, we obtain the following equation:

$$[GM]\{\ddot{q}\} + 2[\omega][GD]\{\dot{q}\} + [\omega]^2\{q\} = \{Q\} \quad (4)$$

where $[GM]$ is an $m \times m$ diagonal generalized mass matrix (derived), $[GD]$ is an $m \times m$ diagonal generalized damping coefficient matrix (estimated), $[\omega]$ is an $m \times m$ diagonal frequency matrix (derived), and m is the number of modes. The generalized forces, which are applied at the hub, are obtained from the airframe excitation force, F_E , and the $6 \times m$ matrix of natural mode shapes expressed at the hub, $[MS_h]$:

$$\{Q\} = [MS_h]^t \{F_E\}_F \quad (5)$$

The excitation force, which is also applied at the hub, is given by

$$\{F_E\}_F = \begin{bmatrix} F_{Ex} \\ F_{Ey} \\ F_{Ez} \\ M_{Ex} \\ M_{Ey} \\ M_{Ez} \end{bmatrix}_F$$

The spatial perturbations are obtained by multiplying the generalized displacement of each mode by the corresponding mode shapes expressed at the point of interest on the airframe:

$$\begin{aligned} \{U_h\} &= [MS_h]\{q\} \\ \{U_p\} &= [MS_p]\{q\} \end{aligned}$$

where $[MS_p]$ is the natural mode shape matrix at the pilot seat. The acceleration of a point on the airframe is then found by twice differentiating the spatial perturbations,

$$\begin{aligned} \{\ddot{U}_h\} &= [MS_h]\{\ddot{q}\} \\ \{\ddot{U}_p\} &= [MS_p]\{\ddot{q}\} \end{aligned} \quad (6)$$

The measured and calculated hub loads identified in section 3.1 can now be related to the excitation force, F_E , which is applied to the fuselage vibration model. The hub forces and moments must first be transformed to the F-frame:

$$\{F_{hub}\}_F = [R_{sf}]\{F_{hub}\}_S \quad (7)$$

where

$$[R_{sf}] = \begin{bmatrix} \begin{bmatrix} -c & 0 & -s \\ 0 & 1 & 0 \\ s & 0 & -c \end{bmatrix} & 0 \\ 0 & \begin{bmatrix} -c & 0 & -s \\ 0 & 1 & 0 \\ s & 0 & -c \end{bmatrix} \end{bmatrix}$$

and c and s are, respectively, the cosine and sine of the shaft angle given in table 1.

As mentioned in section 3.1, the hub forces (F_{hub}) were measured on the rotor shaft right below the hub, as shown in figure 6. Thus F_{hub} includes the hub and blade inertial loads. The finite-element analysis modeled the rotor (including hub and blade mass) as a point mass at the hub; therefore it included the rotor inertia as well. If the measured and calculated hub forces and moments were directly applied to the airframe vibration model, then the rotor inertial loads would be included twice in the analysis. To avoid this situation, the rotor inertial loads were subtracted from the measured and calculated hub loads, thereby obtaining the proper hub excitations, F_E , which are applied at the hub (see fig. 6).

The inertial loads are generated by the rotor mass (hub and blades) multiplied by the acceleration of the hub. Multiplying the hub acceleration from equation 6 by minus the rotor mass matrix, $-[M_r]$, gives the rotor inertial force. The fuselage excitation force is therefore written as

$$\{F_E\}_F = [R_{sf}]\{F_{hub}\}_S + [M_r][MS_h]\{\ddot{q}\} \quad (8)$$

Since the rotor mass was represented as a point mass at the hub in the finite element model of the fuselage, the mass matrix of the rotor, $[M_r]$, in the F-frame is a 6x6 matrix where M_r is input as the first three values of the diagonal and the rest of the matrix is zero. Substituting for $\{F_E\}_F$ in equation 5, and then for $\{Q\}$ in equation 4 yields a new system equation:

$$[GM]\{\ddot{q}\} + 2[\omega][GD]\{\dot{q}\} + [\omega]^2\{q\} = [MS_h]^t[R_{sf}]\{F_{hub}\}_S + [MS_h]^t[M_r][MS_h]\{\ddot{q}\} \quad (9)$$

Regrouping equation 9 by shifting the inertial forces to the left-hand side gives the following system of linear equations for the degrees of freedom of the system excited by the hub loads:

$$\left([GM] - [MS_h]^t[M_r][MS_h] \right) \{\ddot{q}\} + 2[GM][\omega][GD]\{\dot{q}\} + [GM][\omega]^2\{q\} = [MS_h]^t[R_{sf}]\{F_{hub}\}_S \quad (10)$$

Equation 10 indicates that the effect of shifting the inertial forces from the right-hand side of the equation to the left has been to remove the hub mass from the airframe modes. Thus the elastic modes are no longer orthogonal because the new mass matrix $([GM] - [MS_h]^t[M_r][MS_h])$ is no longer diagonal. Consequently, the system equations are now coupled. This system can be

normalized, thus eliminating the coupling, by diagonalizing equation 10 using eigen analysis techniques. Appendix A outlines the procedure for diagonalizing the system.

The next objective is to solve equation 10 for the generalized degrees of freedom, in order to compute the response of the fuselage to the hub loads. Because the structure undergoes 3/rev excitations from the hub loads, it also vibrates at 3/rev. Hence $\{q\}$ and its time derivatives are also at 3/rev. Thus, they can be written

$$\{q\} = \{q_3\}e^{i3\Omega t} \quad , \quad \{\dot{q}\} = 3i\Omega\{q_3\}e^{i3\Omega t} \quad , \quad \{\ddot{q}\} = -9\Omega^2\{q_3\}e^{i3\Omega t} \quad (11)$$

In addition, the hub forces can be similarly expressed:

$$\{F_{hub}\}_S = \{F_{hub3}\}_S e^{i3\Omega t} \quad (12)$$

Substituting equations 11 and 12 into equation 10, and solving for the 3/rev generalized displacements yields

$$\{q_3\} = (-9\Omega^2([GM] - [MS_h]^t[M_r][MS_h] + 6i\Omega[GM][\omega][GD] + [GM][\omega]^2) - [MS_h]^t[R_{sf}]\{F_{hub3}\}_S) \quad (13)$$

The pilot-seat acceleration is also periodic with 3/rev and may be written

$$\{\ddot{U}_p\} = -9\Omega^2\{U_{3p}\}e^{i3\Omega t} \quad (14)$$

Therefore, by substituting equations 11 and 14 into equation 6, the 3/rev pilot-seat vertical acceleration becomes an algebraic expression:

$$\{U_{p3}\} = [MS_p]\{q_3\} \quad (15)$$

3.3 The Forced Response Analysis

The analysis described above was used to develop a forced response program in order to directly predict fuselage vibrations from either measured or predicted hub loads. Two Aerospatiale finite-element airframe vibration models were used in the forced response analysis: an S02 model and a SAMCEF model. They are described in section 4. The baseline generalized damping for both airframe models was assumed to be 3% critical. The forced response program solves for the fuselage degrees of freedom at a specific frequency, or for a range of frequencies. The computational tasks of the forced response program are given in figure 7.

Together the forced response analysis and CAMRAD/JA provide three methods of obtaining vibration predictions. These three methods are outlined in the schematic of figure 8. Airframe accelerations can be computed using measured hub loads in the forced response analysis (fig. 8(a)), using only CAMRAD/JA (fig. 8(b)), or using hub loads from CAMRAD/JA in the forced response analysis (fig. 8(c)).

4 DESCRIPTION OF THE FINITE-ELEMENT VIBRATION MODELS FOR THE SA349/2 HELICOPTER

The two linear finite-element airframe models examined were developed using analyses at Aerospatiale Division Hélicoptères. In 1984, a finite-element model of the SA341 Gazelle was obtained with the S02 finite-element code. The SA341 airframe configuration preceded that of the SA349/2. In 1989, an upgraded finite-element model more representative of the SA349/2 was developed, and a new modal analysis was performed using the SAMCEF finite element code. Both models are discussed here.

The development of a structural model for a 3-bladed helicopter typically involves four phases. First, a finite-element model of the fuselage is generated, as shown in figure 9. Second, a modal analysis is performed on this model. For example, figure 10 shows the SA349/2 airframe in the undeflected and deflected state, as computed using SAMCEF. Third, correlations are generally made with shake test results. Finally, the finite-element model is subsequently revised and damping is estimated from the correlation results. Although these last two steps can be important in establishing the validity of vibration models, they were not part of the S02 and SAMCEF model development. No shake test data are available for correlation with the finite-element models, and no attempt has been made to improve the accuracy of the model or improve the damping estimates. These two models thus rely completely on the inherent accuracy of the finite-element analyses.

The finite-element model generated using the S02 analysis includes 10 substructures, 730 nodes, and 1063 elements (bars, beams, triangles, quadrangles, composite sandwiches). The mass distribution was modeled by 51 concentrated masses, and the frequencies were represented up to 3.25/rev. The finite-element model generated using the SAMCEF analysis is a modified version of the one developed for the SA341. For the SAMCEF model, frequencies were calculated up to 4/rev. The SAMCEF model also included the 15.29-kg rotating instrumentation assembly mounted on top of the hub, which the S02 model did not. Also, both the lateral and longitudinal mast suspension, designed to reduce the net moments on the fuselage which contribute significantly to the pilot-seat vertical acceleration, were modeled using SAMCEF, whereas only the lateral suspension was modeled using S02. Although the SAMCEF analysis provided a somewhat improved representation of the airframe, certain components were not modeled by either analysis. In particular, a 192-kg data acquisition bay, located in the cabin behind the pilot seats during the SA349/2 flight tests, was not included. Also, the fuel amount was assumed to be 370 kg for all cases; however it actually varied from 242 to 296 kg. Thus, despite certain improvements, the SAMCEF model of the SA349/2 still did not model every aspect of the complete aircraft.

4.1 S02 Vibration Model of the SA341 Fuselage

The S02 analysis yielded 15 airframe modes, listed in table 4. The first six are the rigid modes, which have been transformed into rigid body translations and rotations in the F-frame according to the analysis of appendix B. The elastic modes (7 through 15) are identified by their frequency, generalized mass, and mode shape characteristics. The hub and pilot-seat translation and rotation mode shapes are written in the F-frame. The baseline damping for each elastic mode is assumed to be 3% critical.

The structural model was characterized by plotting the frequency response of the pilot seat to unit hub loads. Figure 11 presents the magnitude and phase response at the pilot seat to each of the six unit hub load components. The 3/rev frequency (19.35 Hz), which is marked on the plots, is close to modes 14 (17.75 Hz, fuel tank mode) and 15 (20.92 Hz, 2nd fuselage vertical bending mode). By examining the shape of the response near 3/rev, we note that the model appears to be partially tuned. The local minimum response to unit H (fig. 11(a)) and M_y (fig. 11(e)) are centered on 3/rev, yielding the minimum response. The response can be reduced by adjusting the damping and frequency. The response to unit H and unit M_y are similar in phase and amplitude. The response to unit Y (fig. 11(b)) and unit M_x (fig. 11(d)) are similar in amplitude but opposite in phase.

4.2 SAMCEF Vibration Model of the SA349/2 Fuselage

The SAMCEF analysis yielded 20 modes, listed in table 5. The first six are the rigid modes, which have been transformed into rigid-body translations and rotations in the F-frame according to the analysis of appendix B. The elastic modes (7 through 20) are identified by their frequency, generalized mass and mode shape characteristics. The modal deflections were studied in order to identify each mode. For example, the deflection of the first vertical bending mode is pictured in figure 10. The hub and pilot-seat mode shapes, written in the F-frame are shown in table 5. Since the SAMCEF data set provided did not include the rotation mode shapes at the hub, they were derived from the translation mode shapes. This derivation is summarized in appendix C. The baseline damping for each elastic mode was assumed to be 3% critical.

The SAMCEF vibration model was characterized by plotting the frequency response at the pilot seat to unit hub loads. Figure 12 presents the magnitude and phase response at the pilot seat to each of the six unit hub load components. The 3/rev frequency, which is marked on the plots, is close to modes 14 (16.86 Hz) through 18 (20.76 Hz). Compared to the S02 model, the response of the SAMCEF vibration model is generally lower, indicating the influence of the additional modes. Although the frequency response indicates that the fuselage vibration could benefit from further tuning of the structural dynamics, in general the 3/rev response is small, and not greatly influenced by the proximity of the higher modes.

5 RESULTS

5.1 Hub Loads Correlations

Since the hub loads produced the airframe vibration, they were examined first. Ten configurations of the aircraft model in CAMRAD/JA were used for predicting the hub loads, which were then correlated with measured hub loads. Table 6 summarizes features of the different model configurations. The parameters studied include the type of finite-element model: S02 or SAMCEF; whether or not rotation mode shapes were included; the type of inflow model used—uniform, non-uniform with a prescribed wake geometry, or nonuniform with a free wake geometry; and whether or not feedback of the airframe motion was used in the analysis. Predictions were made for all six flight conditions listed in table 2.

5.1.1 Correlation of the Hub Forces and Moments (Magnitude Only)— The amplitudes of the hub forces and moments vs. advance ratio and thrust-to-solidity ratio were plotted in figures 13-15, in order to compare the different model configurations. Figure 13 shows, as a function of advance ratio, the measured loads and those predicted using the SAMCEF and S02 models, both with and without angular mode shapes (configurations 4, 5, 9, and 10 in table 6). Omitting the rotation mode shapes meant omitting both the hub moment excitation and the hub angular motion feedback to the rotor. These predictions were made using a nonuniform inflow wake model in the CAMRAD/JA analysis, as well as feedback of the airframe motion to the rotor.

The most noticeable result is that only the in-plane forces and moments (figs. 13(a), (b), (d), and (e)) are affected by the model configuration changes. In addition, when the angular mode shapes are not included (configurations 5 and 10), the S02 and SAMCEF results are similar for the in-plane loads, except H , the drag force. When all mode shapes are included (configurations 4 and 9), the SAMCEF model leads to lower hub loads, except for Y and M_y at high speed. The reductions in H (fig. 13(a)) and M_y (fig. 13(e)) suggest there is less reaction from the hub along the x_S - and y_S -axes for the SAMCEF model than for the S02 model. This may be the result of the longitudinal suspension, which was modeled in SAMCEF but not in S02. Including longitudinal suspension led to lower hub stiffness in the x_S - and y_S -axes. Decreased stiffness allowed greater hub motions, and thus increased the 3/rev inertial component of the longitudinal force and pitching moment of the hub. If the excitation force, F_E , is held constant, then an increase in the inertial components must be accompanied by a decrease in the net hub longitudinal force and hub pitching moment (see eq. 8).

The S02 model matches the trends of the data better for H and M_y . However, figure 13 shows that the trends in magnitude of the in-plane hub loads are slightly better predicted using the SAMCEF model with rotation mode shapes (configuration 4). As a result, the remaining hub load correlations were made using the SAMCEF finite-element model.

Figures 14 and 15 show, as a function of advance ratio and thrust-to-solidity ratio, the effects on predicted hub loads of hub/airframe motion coupling, and of different rotor wake models (configurations 1-4 in table 6). A uniform inflow model and a nonuniform inflow, prescribed wake model

were studied. For the lowest-speed condition ($\mu = 0.14$), a free wake analysis was used instead of a prescribed wake model. The predictions were made using the SAMCEF model with rotation mode shapes. Examining the trends with advance ratio, we notice in figure 14 that the out-of-plane loads are mainly influenced by the inflow model, while the in-plane loads are affected by both the inflow model and feedback. The thrust (fig. 14(c)) and torque (fig. 14(f)) correlations improved when a nonuniform inflow wake model was used. The forces (figs. 14(a)-(c)) were best predicted using a nonuniform inflow wake model with airframe motion feedback, although at high speed the predictions began to diverge from the data. The moments (figs. 14(d)-(f)) were more difficult to analyze, because few consistent effects were observed with the configuration changes. However, using a nonuniform inflow wake model did improve the trends of the M_x and Q correlations.

Figure 15 examines, as a function of C_T/σ , the effect on the hub loads of model configurations 1 to 4. The in-plane forces (figs. 15(a) and (b)) are mostly affected by the presence of airframe motion feedback, which slightly improves the correlation of Y but not H . The thrust (fig. 15(c)) is primarily influenced by the inflow wake model, as are both M_y and Q (figs. 15(e) and (f)). Here, however, the nonuniform-inflow wake model didn't really improve the correlations, and even reversed the trend of T and Q at high thrust. The rolling moment, M_x , was best predicted using configuration 4.

Although no single configuration clearly yielded the best results in every case, configuration 4 (the SAMCEF model, with rotation mode shapes, a nonuniform-inflow wake model, and airframe motion feedback) was responsible for the majority of the correlation improvements. However, figures 13-15 show hub load magnitudes only, providing no information concerning the phase. Detailed magnitude and phase correlations are presented in the next section, which examines the same configurations studied in figures 13-15.

5.1.2. Phase Correlations of the Hub Loads— Magnitude and phase correlations are shown in figures 16-33 for each hub load component. The figures contain separate vector plots for each flight condition. Each plot contains vectors representing various model configurations from table 6, and a data vector (solid arrow). Note that the scale used for the different plots of figures 16-33 varies.

Figures 16-21 correspond to the plots of figure 13 discussed above (e.g., figs. 16(a)-(d) show the magnitude and phase information for fig. 13(a)). A glance through these figures reveals a wide variation in the phase correlations from one plot to another. Only the out-of-plane loads (figs. 18 and 21) provide some consistency; they are unaffected by the different model configurations, and correlate fairly well with the measured phase angles. The thrust and torque are independent of the fuselage model because neither the drive train nor the shaft rotation were modeled. Thus, torque predictions were not affected by the motion feedback to the rotor. Thrust was not affected by the different models because the shaft was very stiff axially, thereby limiting the response of the z -degree of freedom.

The phase correlations of the in-plane forces are influenced by both the finite-element model and the rotation mode shapes. At low speed, the SAMCEF model with rotation mode shapes (configuration 4) provides the best match to the data. The in-plane moment phase correlations are affected

by the airframe model only when rotation mode shapes are included. For the in-plane loads, the effect of the various configurations on the correlation was mixed. The S02 model yielded slightly better correlations with phase than the SAMCEF model.

Figures 22-27, which correspond to figure 14, and figures 28-33, which correspond to figure 15, present plots correlating the measured hub loads with the CAMRAD/JA hub loads predicted with and without feedback, and with various inflow models (configurations 1-4 in table 6). The vectors are labeled as uniform inflow model (UI), nonuniform inflow with prescribed wake model (NUI), or free wake analysis (FW) for the lowest speed case. Figures 22-27 present each hub load component for the four speed-sweep cases (V3101, V3103, V3105, V3106), at approximately constant thrust ($C_T/\sigma = 0.066$), and figures 28-33 show each component for the three thrust-sweep cases (V3103, V3109, V3111) at approximately constant advance ratio ($\mu = 0.26$).

A cursory review of figures 22-27 reveals some patterns in the responses. For example, the phase correlations of the in-plane forces are primarily influenced by airframe motion feedback, while the in-plane moments are not much changed by either feedback or the inflow model. The out-of-plane loads are affected mostly by the inflow model. The nonuniform inflow wake model notably improved the phase correlations of thrust and torque.

For the thrust-sweep cases (figs. 28-33), the phase correlations of the out-of-plane loads are similar to the speed-sweep cases. They are affected primarily by the inflow model. Torque correlations improve with a nonuniform-inflow wake model. Phase correlations of the in-plane forces generally improved with feedback and a nonuniform-inflow wake model. The in-plane moments showed little difference in phase among the different models.

Figures 16-33 show that phase is generally not well predicted, and can vary widely depending on the model used to predict hub loads. Overall, however, using SAMCEF with rotation mode shapes in CAMRAD/JA provided somewhat better correlations of both magnitude and phase than the other model configurations.

5.2 Prediction of the Pilot-Seat Acceleration

The forced-response program was run according to the schematic in figure 7, using measured and predicted hub loads to calculate vibration. This program predicted 3/rev vertical pilot-seat accelerations, using the S02 and SAMCEF vibration models of the fuselage. The measured and predicted hub loads for the six flight cases presented in table 2 constituted the fuselage excitations. Analysis of the predictions was performed in four steps:

1. Examine the contribution of each hub load. The forced-response analysis calculated the transfer function matrix of the vibration model with the rotor inertia removed. This matrix, which related 3/rev hub forces and moments to 3/rev vertical pilot-seat acceleration, is applied to each component of the measured hub loads to calculate the contribution of each load to the acceleration.
2. Examine the contribution of each mode. The degrees of freedom q_k were obtained by using the forced-response analysis, and multiplied by each mode shape coefficient in the z-direction

at the pilot seat. This gave the contribution of each mode to the acceleration. The high speed case V3106 ($\mu = 0.37$, $C_T/\sigma = 0.066$), which had the greatest measured pilot-seat vertical acceleration, was chosen for this step.

3. Examine the sensitivity of acceleration to the generalized damping and modal frequencies. The generalized damping of all modes was varied from 1 to 10% critical, keeping the frequencies constant. Then the frequencies of all modes were varied from 95 to 105% of baseline, keeping the baseline damping of 3% critical constant. Condition V3106 was chosen for this step.

4. Reduce the predicted acceleration through modifications to the vibration model. The generalized damping and frequencies of specific modes were altered in an attempt to achieve a reduction in the total acceleration. Condition V3106 was chosen for this step.

5.2.1 Correlation with Vibration Predicted from Measured Hub Loads– The airframe vibration caused by the measured hub loads was calculated and examined extensively. Overall predictions of the pilot-seat vertical acceleration for the four level-flight cases are shown in figure 34. The figure shows the predicted vibration for the S02 and SAMCEF models (without rotor inertia) both with and without rotation mode shapes. The different configurations used for the predictions are summarized in table 7. Removing the rotation mode shapes has a larger effect on the SAMCEF model than on the S02 model. Both models significantly overpredict the measured vibrations at high speed.

Figures 35 and 36 examine the contribution of each measured hub load to the amplitude of the predicted acceleration for the S02 and SAMCEF models. The four level flight conditions were examined. Both figures show that the moments contribute no more than 20% to the magnitude of the total acceleration. Both S02 and SAMCEF behave similarly, differing primarily in the reaction to thrust. As a result, the remainder of this section will focus on the more complete SAMCEF model. Figure 36 shows that at low speed, the contribution of each force is significant, whereas at high speed, sideforce produces the most response. At high speed the increase in magnitude of the total acceleration is due to the increase in magnitude of the sideforce.

Figure 37 shows the contribution of each mode to the acceleration. The main contributions are from modes 15 (18.61 Hz, 2nd fuselage vertical bending) and 19 (21.9 Hz, fuselage + fuel tank). Mode 15 is important because its frequency is near 3/rev (19.35 Hz). Mode 19 is important because its response at the pilot seat and at the hub is large (see table 5).

The effect on vertical acceleration of varying the generalized damping linearly from 1 to 10% is plotted in figure 38. The result shown in figure 38(a) is primarily a decrease in magnitude. The modal contribution plots for the damping extremes shown in figures 38(b) and 38(c) reveal that the vibration response of mode 15 is highly influenced by changes in damping, both in magnitude and phase. This was expected, since the frequency of that mode is near the 3/rev frequency of the rotor.

The effect of varying the frequency of all modes $\pm 5\%$ is plotted in figure 39. The evolution shown in figure 39(a), is mainly a linear phase change of 80° . The modal contribution plots shown in figures 39(b) and 39(c) reveal that mode 15 is again primarily responsible for the overall change.

Reducing the predicted acceleration through modal modification is shown in figure 40. First, the frequencies of modes 15 and 19 were adjusted so that their net vibratory contribution was reduced. This was achieved by increasing the frequency of mode 15 by 25% to 23.3 Hz and reducing the frequency of mode 19 by 5% to 20.8 Hz. The result is shown in figure 40(b). Next the damping of each of the significant modes was independently adjusted. A further reduction of acceleration was achieved for a generalized damping of 3% for all modes except modes 15 and 19, whose damping was increased to 9% (fig. 38(c)). Table 8 summarizes the specific changes in modal frequency and damping. The overall changes to the total acceleration is shown in figure 40(d). Clearly, tuning the model improves the correlation, particularly with respect to magnitude.

5.2.2 Correlation with Vibration Predicted from Calculated Hub Loads– Airframe vibration caused by predicted hub loads was also calculated, and examined in the same manner as above. Figure 41 shows the amplitude of the pilot seat acceleration versus advance ratio predicted with CAMRAD/JA using different airframe models. The pilot seat vertical accelerations correspond to the predicted hub loads shown in figure 13. The measured accelerations are included also. In figure 41, a nonuniform inflow wake model with rotor/fuselage feedback was used in the CAMRAD/JA analysis.

In all cases, the vibration is overpredicted, but the SAMCEF model yields the closest results. The effect of setting the hub rotation mode shapes to zero decreases the acceleration predicted using SAMCEF and increases the acceleration predicted using S02. The S02 predictions increase by 0.5 g for all speeds. This constant 0.5 g increase in acceleration can be related to the constant increase in H caused by turning off the hub rotation mode shapes as shown in figure 13. Comparing figure 41 with figure 34 reveals that the predicted hub loads yield lower vibration than the measured loads, particularly at high speed. Differences, primarily with phase, in the hub loads correlations account for this.

Figure 42 shows the pilot-seat vertical acceleration predicted with uniform inflow and nonuniform inflow wake models, and with and without airframe motion feedback to the rotor, for the SAMCEF model. The influence of feedback for constant C_T/σ (fig. 42(a)) is to reduce the vibration. The inclusion of nonuniform inflow in the model increases vibrations, especially at low speed. Although this results in worse correlation with magnitude, the trend of magnitude versus advance ratio is actually better matched. At high thrust (fig. 42(b)), the introduction of nonuniform inflow actually reverses the trend of the uniform inflow predictions and results in a reduction of pilot-seat acceleration at high thrust, better matching the data.

As with the measured hub loads, the calculated hub loads were used in the forced response program. The hub loads used in this section were those predicted by CAMRAD/JA with feedback, using both fuselage vibration models. The rotation mode shapes in this case were set to zero to ensure that both CAMRAD/JA and the forced response analysis were calculating the same vibration for a given hub excitation. The aerodynamic loads calculated by CAMRAD/JA (and used to evaluate the hub forces and moments) are operated on by a smoothing function, in order to make them consistent with the Fourier analysis used in the equations of motion (see ref. 10, pp. 448-9). Because of the application of this smoothing function, which aids convergence of the analysis, the hub loads provided in the CAMRAD/JA output differ somewhat from the internally calculated hub loads CAMRAD/JA uses directly to predict fuselage accelerations. The differences are manifested primarily in the hub moments. As a result, in order to achieve the same vibration using either

CAMRAD/JA or the forced response analysis, the influence of the moments on the acceleration was eliminated. This was accomplished by suppressing the rotation mode shapes at the hub.

Figure 43 shows the contributions of the three predicted hub forces to the total acceleration predicted by CAMRAD/JA using S02. For the S02 model, H is the main contribution to the acceleration. Comparing figures 43 and 35 indicates that the measured hub forces contribute differently to pilot-seat acceleration than the predicted hub forces. In figure 35, H has a small component at high speed, whereas Y and T produce much larger response than in figure 43.

Figure 44 shows the contributions of the three predicted hub forces to the total acceleration predicted using SAMCEF. The acceleration is of smaller amplitude than that calculated using S02, yielding much better correlations. The contribution of Y is small at low speed, while H and T are important at all speeds. Comparing figures 44 and 36 indicates that the measured hub forces contribute differently to the acceleration than the predicted hub forces, as discussed above for S02 model.

The sensitivity of the vibration predicted using the calculated hub loads is plotted in figures 45-47. The SAMCEF model was used in this analysis. The main contributions to the pilot seat acceleration again come from modes 15 and 19. The effect of varying the generalized damping from 1% to 10% linearly is plotted in figures 45(a). The total vector changed only slightly with the damping. However figures 43(b) and (c) show that the contribution of mode 15 is fairly sensitive to the damping, especially in phase, reflecting its proximity to 3/rev.

The effect of varying the modal frequencies $\pm 5\%$ linearly is plotted in figure 46. Figure 46(a) shows that the result is primarily a phase change. Again, the contribution of mode 15 is highly sensitive, both in magnitude and phase, to slight changes in frequency, as seen by comparing figures 46(b) and (c).

The SAMCEF model was modified to reduce vibration predicted using CAMRAD/JA hub forces. The result is shown in figure 47. Figure 47(a) shows the original vibration, along with the major modal contributions. The frequencies of certain modes were altered (see table 9), reducing the vibration (fig. 47(b)). The modal damping was then changed according to table 9 to yield the final reduced vibration plotted in figure 47(c). Figure 47(d) compares the total vectors of figures 47(a)-(c), along with the data. This study shows that even relatively small, well placed changes in the characteristics of the vibration model have a large effect on the predicted vibration, and hence on the correlation.

6 CONCLUDING REMARKS

Accurate and consistent prediction of airframe acceleration relies primarily on two factors: accurate predictions of the hub forces and moments, and an accurate finite-element model representing the elastic behavior of the airframe. This study examined both factors using the SA349/2 Gazelle helicopter. The intent was to determine the current capability to predict vibration, and to shed some light on the degree of accuracy required for the airframe model in order to achieve good results.

Hub loads correlations:

The best correlations were achieved using the most sophisticated analysis. This analysis included a nonuniform inflow wake model, the more complex fuselage model (SAMCEF), and airframe motion feedback to the rotor. Predictions of magnitude were relatively close; however, correlations with phase varied widely.

Finite-element airframe model:

Predictions of pilot-seat vertical acceleration using either measured or predicted hub loads were well above the measured vibration, indicating that the finite-element model did not fully account for the structural properties of the airframe. To substantially improve the model, a shake test of the SA349/2 is required. This would remove a major uncertainty from the vibration predictions, and allow a much more rigorous critique of the hub loads and airframe vibration calculations.

Airframe accelerations:

The trend of the measured accelerations with changing flight condition was well captured by the predictions, although in general magnitude was greatly overestimated. The vibration resulted mainly from the hub forces, rather than the hub moments, and only two of the airframe modes contributed most of the response. The most significant modes had either a frequency near 3/rev or large responses at both the hub and pilot seat.

Sensitivity of vibrations to modal characteristics:

Relatively small variations of the characteristics of selected airframe modes can lead to large changes in the acceleration, demonstrating that appropriate tuning the modes can lead to reduced vibrations on a helicopter. This exercise also indicated that structural models must be accurate to within a few percent in both frequency and damping to yield good results. Even a 5% error in frequencies, for example, can effect a large change in the response.

APPENDIX A

Diagonalizing the Fuselage Degrees of Freedom Without Rotor Inertia

As described in section 3.2, in order to apply the measured hub loads to the structural model, which included the rotor (hub and blades) mass concentrated at the hub, it was necessary to subtract the rotor inertial loads. Equivalently, the rotor inertia could be removed from the vibration model, rather than from the hub loads, as shown in equation 10. Removing the rotor mass from the model, however, alters the frequencies and modes of the system. To note the effect on the frequency of each mode, plots of frequency versus amount of rotor mass removed were made for both models (fig. A1). The vertical lines on each plot mark the point at which the total rotor mass was removed from the math model. The rotor mass for the S02 model was 219.71 kg; that for the SAMCEF model was 235 kg, reflecting the additional weight of the rotating-frame instrumentation assembly above the rotor hub. Certain modes were significantly affected, as evinced by the sharp changes in frequency as more mass is removed.

These changes resulted from strong coupling among some of the modes. Thus, the effect of subtracting the rotor inertial loads from the finite element model was to introduce coupling into the system. This coupling can be removed by solving equation 10 for the eigenvalues, ω_i , and eigenvectors, $\{V_i\}$. The uncoupled equations are determined by solving the undamped, homogeneous version of equation 10, in the following form,

$$\left(\omega_i^2 \left([GM] - [MS_h]^t [M_r] [MS_h] \right) - [GM][\omega]^2 \right) \{V_i\} = [0] \quad (A1)$$

Equation A1 determines a new set of orthogonal modes (i.e., diagonalizes eq. 10). Solving this eigenvalue problem yields a diagonal matrix of m new eigen frequencies $[\omega^*]$, a matrix of m eigenvectors $[V]$, and a new $m \times m$ diagonal mass matrix, $[GM^*]$. The new generalized mass and frequencies can be used to express the following new set of generalized system equations, neglecting damping,

$$[GM^*] \{ \ddot{q}^* \} + [\omega^*]^2 \{ q^* \} = \{ Q^* \} \quad (A2)$$

Adding a proportional damping matrix, $[GD^*]$, to equation A2 yields,

$$[GM^*] \{ \ddot{q}^* \} + 2[\omega^*][GD^*] \{ \dot{q}^* \} + [\omega^*]^2 \{ q^* \} = \{ Q^* \} \quad (A3)$$

where the starred terms retain the same general definitions as their unstarred counterparts.

The modal characteristics of the new system are related to the natural modes of the fuselage with the rotor mass through the matrix of eigenvectors, $[V]$,

$$\begin{aligned} [GM^*] &= [V]^t [GM] [V] \\ [\omega^*]^2 &= [V]^t [\omega]^2 [V] \end{aligned} \quad (A4)$$

The generalized damping of the new model, however, is not related to the original damping. In equation A3, $[GD^*]$ was specified to be diagonal, not a function of $[GD]$. The new generalized displacements, $\{q^*\}$, and forces, $\{Q^*\}$, are related to $\{q\}$ and $\{Q\}$, respectively, through the eigenvectors,

$$\begin{aligned} \{q^*\} &= [V]^t \{q\} \\ \{Q^*\} &= [V]^t \{Q\} \end{aligned} \quad (A5)$$

The new mode shape matrices can also be derived from the original mode shape matrices through the eigenvectors,

$$\begin{aligned} [MS_h^*] &= [MS_h] [V] \\ [MS_p^*] &= [MS_p] [V] \end{aligned} \quad (A6)$$

The excitation force vector, $\{F_E\}_F$, is related to the new generalized force vector through the new mode shape matrix expressed at the hub,

$$\{Q^*\} = [MS^*]^t \{F_E\}_F \quad (A7)$$

The spatial perturbations are related to the new generalized displacements through the appropriate mode shape matrices,

$$\begin{aligned} \{U_h\} &= [MS_h^*] \{q^*\} \\ \{U_p\} &= [MS_p^*] \{q^*\} \end{aligned} \quad (A8)$$

Again considering only the third harmonic of the degrees of freedom, we find that

$$\{q^*\} = \{q_3^*\} e^{i3\Omega t} \quad \{\dot{q}^*\} = 3i\Omega \{q_3^*\} e^{i3\Omega t} \quad \{\ddot{q}^*\} = -9\Omega^2 \{q_3^*\} e^{i3\Omega t} \quad (A9)$$

Substituting equations A9 into equation A3, and solving for $\{q_3^*\}$, we obtain,

$$\{q_3^*\} = \left([MG^*] (-9\Omega^2 + 6i\Omega [\omega^*] [GD^*] + [\omega^*]^2) \right)^{-1} [MS_h^*]^t [R_{sf}] \{F_{hub3}\}_S \quad (A10)$$

Taking the inverse of this system is now simplified because the modes are uncoupled, indicating diagonal matrices.

This system of new modes represents a different airframe than the one modeled in the finite element analyses. Equation A10 describes the airframe body only, not including the rotor. Therefore, one should keep in mind, if using these new modes, that they are not the same as the modes of the original system with the rotor mass included.

The acceleration vector, derived from the generalized 3/rev accelerations and the pilot-seat mode shapes, can be obtained from either the coupled (eq. 15) or the uncoupled (eq. A10) system,

$$\{U_{p3}\} = [MS_p]\{q_3\} = [MS_p^*]\{q_3^*\} \quad (A11)$$

APPENDIX B

Rigid-Body Modes

The aircraft weight, moments of inertia, and cg position, which can be used to derive the rigid-body modes, are known for the flight test conditions either from direct measurement or calculation (see tables 1 and 2). The aircraft weight and cg position for each flight were used to trim the helicopter in CAMRAD/JA, so that the calculated rotor thrust had the correct value. The finite element models, however, correspond to somewhat different values of gross weight, moments of inertia, and cg position, because not every component of the airframe was included in the analyses. Although the rigid-body modes were not directly excited by the 3/rev hub loads, they did influence the coupled system response when the rotor mass was removed (eq. 10 and appendix A). Hence the finite-element rigid-body modes were included in calculations of the fuselage vibration, both in the forced response program and in CAMRAD/JA. The internally calculated rigid mode shapes were not used in CAMRAD/JA. Instead, the finite-element rigid-body modes were input as the first six elastic modes in CAMRAD/JA, followed by the remaining elastic modes.

The uncoupled rigid modes from the finite-element codes can be used directly, but may not be easily interpreted. To interpret the rigid modes, it is desirable to transform them to pure translation and rotation of the aircraft center of gravity. Sometimes principal axes are used, but here the rigid modes will be transformed to the aircraft body axes (F-frame). The resulting values of gross weight, moments of inertia, and cg position (from the finite element codes) can be compared with the flight test values given in tables 1 and 2.

If the rigid mode shapes are known for at least three points on the body, $i \geq 3$, it is possible to transform them into a set of modes consisting of pure translations and pure rotations about the F-axes of the body. The rigid-body motion can be described by

$$\begin{Bmatrix} \vdots \\ \Delta r_i \\ \vdots \end{Bmatrix} = \Phi_r \begin{Bmatrix} \Delta u \\ \Delta \theta \end{Bmatrix} \quad (\text{B1})$$

where Δr_i is the displacement vector, Φ_r is the mode shape matrix, Δu and $\Delta \theta$ are the linear and angular perturbations of the body. Such motion has the following linear mode shapes:

$$\Phi_r = \begin{bmatrix} \vdots & & \\ I & -r_i \times & \\ \vdots & & \end{bmatrix} \quad (\text{B2})$$

where I is the 3x3 identity matrix and $-r_i \times$ is a 3x3 cross-product matrix. A point mass m_i , is associated with the linear modes at each r_i . These masses form a diagonal matrix,

$$M = \begin{bmatrix} \ddots & & & & & \\ & m_i & & & & \\ & & m_i & & & \\ & & & m_i & & \\ & & & & \ddots & \\ & & & & & \ddots \end{bmatrix} \quad (B3)$$

which is associated with the matrix of linear mode shapes. The modal mass, then, for rigid motion Φ_r is given by

$$M_{\Phi} = \Phi_r^T M \Phi_r \quad (B4)$$

If the points, r_i , are all referenced to the aircraft cg location, then the modal mass matrix will have the form

$$M_{\Phi} = \begin{bmatrix} [m] & 0 \\ 0 & [I_{cg}] \end{bmatrix} \quad (B5)$$

where $[m]$ is a 3×3 diagonal matrix of the aircraft mass, and $[I_{cg}]$ is a 3×3 matrix of the aircraft moments of inertia about the cg location. The objective is to derive the matrix M_{Φ} using the mode shapes and modal masses provided by the finite-element models.

Mode shape matrices, Ψ_r , provided by the finite element models can be related to Φ_r :

$$\Psi_r = [\dots \Psi_{rk} \dots] = [\dots \Phi_{rj} \dots] [C_{jk}] = \Phi_r C \quad (B6)$$

where C is a 6×6 transformation matrix, with independent columns. The transformation matrix C can be obtained by inverting equation B6. Since the matrices Φ_r and Ψ_r have dimension $3i \times 6$, where, in general, $3i > 6$ (i is the number of points on the body), then a least-squares inversion is necessary to find C :

$$C = (\Phi_r^T \Phi_r)^{-1} (\Phi_r^T \Psi_r) \quad (B7)$$

The mass matrix, M_{Ψ} , associated with Ψ_r can be related to the matrix of point masses as well:

$$M_{\Psi} = \Psi_r^T M \Psi_r \quad (B8)$$

Thus M_{Φ} can be determined by transforming M_{Ψ} into the F-frame:

$$M_{\Phi} = C^{-T} \Psi_r^T M \Psi_r C^{-1} = C^{-T} M_{\Psi} C^{-1} \quad (B9)$$

Transformation of SAMCEF rigid modes into the F-frame.

The SAMCEF finite-element output provided translation mode shapes and modal masses at three points (the hub, the pilot seat, and an arbitrary third point on the body) for each of the six rigid-body degrees of freedom:

$$\Psi_r = \begin{bmatrix} 1.0000 & 0.1912 & 0.0006 & -0.0009 & 0.0006 & -0.2173 \\ 0 & 0 & -0.8965 & -0.2061 & 0.0469 & 0.0023 \\ 0 & 0.6378 & 0.0031 & -0.0014 & -0.0005 & 0.0648 \\ 1.0000 & -0.0725 & 0.0419 & 0.0667 & -0.1057 & 0.0820 \\ 0 & 0 & 0.0594 & -0.8382 & 0.1374 & -0.0000 \\ 0 & 0.8258 & -0.3475 & 0.1628 & 0.0449 & -0.1478 \\ 1.0000 & 0.0401 & -0.0184 & -0.0293 & 0.0465 & -0.0453 \\ 0 & 0 & -0.3236 & -0.5288 & 0.0358 & 0.0007 \\ 0 & 0.6933 & 0.1542 & -0.0721 & -0.0201 & 0.0014 \end{bmatrix}$$

$$M_\Psi = \begin{bmatrix} 1907.7 & 0 & 0 & 0 & 0 & 0 \\ 0 & 851.8 & 0 & 0 & 0 & 0 \\ 0 & 0 & 316.4 & 0 & 0 & 0 \\ 0 & 0 & 0 & 738.6 & 0 & 0 \\ 0 & 0 & 0 & 0 & 69.7 & 0 \\ 0 & 0 & 0 & 0 & 0 & 89.7 \end{bmatrix}$$

The matrix Φ_r was determined for the SAMCEF model from the coordinates of the three points with respect to the cg (F-frame), and M_Φ was calculated from equation B9. The correct cg position was obtained by iterating on equations B2 and B9 until the upper right-hand and lower left-hand quadrants of M_Φ were zero.

For the SAMCEF model, the positions of the hub, pilot seat, and instrumentation rack, with respect to the cg (F-frame) were determined to be

Hub	Pilot seat	Instrumentation rack
$x_F = -0.036$	1.417	0.392
$y_F = -0.005$	0.680	-0.299
$z_F = -1.479$	0.561	-0.310

The corresponding M_Φ is

$$M_\Phi = \begin{bmatrix} 1907 & 0 & 0 & 0 & 0 & 0 \\ 0 & 1907 & 0 & 0 & 0 & 0 \\ 0 & 0 & 1907 & 0 & 0 & 0 \\ 0 & 0 & 0 & 1181 & 0 & -689 \\ 0 & 0 & 0 & 0 & 3839 & 0 \\ 0 & 0 & 0 & -689 & 0 & 3085 \end{bmatrix}$$

The hub and pilot-seat rigid modes in the F-frame, according to the SAMCEF model, are

$$MS_{hr} = \begin{bmatrix} 1.0000 & 0 & 0 & 0 & -1.4783 & 0.0051 \\ 0 & 1.0000 & 0 & 1.4783 & 0 & -0.0361 \\ 0 & 0 & 1.0000 & -0.0051 & 0.0361 & 0 \\ 0 & 0 & 0 & 1.0000 & 0 & 0 \\ 0 & 0 & 0 & 0 & 1.0000 & 0 \\ 0 & 0 & 0 & 0 & 0 & 1.0000 \end{bmatrix}$$

$$MS_{pr} = \begin{bmatrix} 1.0000 & 0 & 0 & 0 & 0.5608 & -0.6799 \\ 0 & 1.0000 & 0 & -0.5608 & 0 & 1.4174 \\ 0 & 0 & 1.0000 & 0.6799 & -1.4174 & 0 \\ 0 & 0 & 0 & 1.0000 & 0 & 0 \\ 0 & 0 & 0 & 0 & 1.0000 & 0 \\ 0 & 0 & 0 & 0 & 0 & 1.0000 \end{bmatrix}$$

Transformation of S02 rigid modes into the F-frame.

As with SAMCEF, the S02 finite-element output provided translation mode shapes and modal masses at three points (the hub, the pilot seat, and an arbitrary third point on the body) for each of the six rigid-body degrees of freedom:

$$\Psi_r = \begin{bmatrix} 0.0087 & -0.1322 & -0.0771 & -0.3201 & -0.0421 & 0.9868 \\ 0.1489 & 0.0480 & -0.9119 & 0.0694 & 0.1497 & -0.0983 \\ -0.0022 & 0.2429 & 0.0107 & -0.2175 & 0.0055 & -0.1664 \\ -0.0923 & 0.1350 & -0.0013 & 0.1033 & -0.1115 & 0.8468 \\ -0.1547 & -0.0260 & 0.0378 & -0.0362 & 0.4075 & 0.1109 \\ 0.1464 & 0.0703 & -0.2836 & -0.4949 & -0.0098 & -0.1209 \\ 0.0170 & 0.0203 & -0.0366 & -0.0783 & -0.0016 & 0.9295 \\ -0.3422 & 0.0140 & -0.3507 & 0.0212 & -0.0840 & -0.0896 \\ -0.0438 & 0.3854 & 0.1061 & 0.0083 & 0.0207 & -0.2200 \end{bmatrix}$$

$$M_\Psi = \begin{bmatrix} 206.8 & 0 & 0 & 0 & 0 & 0 \\ 0 & 178.6 & 0 & 0 & 0 & 0 \\ 0 & 0 & 337.1 & 0 & 0 & 0 \\ 0 & 0 & 0 & 260.1 & 0 & 0 \\ 0 & 0 & 0 & 0 & 151.5 & 0 \\ 0 & 0 & 0 & 0 & 0 & 1622.8 \end{bmatrix}$$

The matrix Ψ_r was determined for the S02 model from the coordinates of the three points with respect to the cg (F-frame), and M_Φ was calculated from equation B9. The correct cg position was obtained by iterating equations B2 and B9 until the terms in the upper right- and lower left-hand quadrants of M_Φ were zero.

For the S02 model, the positions of the hub, pilot seat, and a gearbox mount, with respect to the cg (F-frame) were determined to be:

	Hub	Pilot seat	Gearbox mount
$x_F =$	-0.045	1.408	-1.168
$y_F =$	-0.005	0.507	-0.123
$z_F =$	-1.492	0.547	-0.315

The corresponding M_{Φ} is:

$$M_{\Phi} = \begin{bmatrix} 1879 & 0 & 0 & 0 & 0 & 0 \\ 0 & 1879 & 0 & 0 & 0 & 0 \\ 0 & 0 & 1879 & 0 & 0 & 0 \\ 0 & 0 & 0 & 1142 & 0 & -683 \\ 0 & 0 & 0 & 0 & 3755 & 0 \\ 0 & 0 & 0 & -683 & 0 & 3050 \end{bmatrix}$$

The hub and pilot-seat rigid modes in the F-frame, according to the S02 model, are:

$$MS_{hr} = \begin{bmatrix} 1.0000 & 0 & 0 & 0 & -1.4922 & 0.0045 \\ 0 & 1.0000 & 0 & 1.4922 & 0 & -0.0452 \\ 0 & 0 & 1.0000 & -0.0045 & 0.0452 & 0 \\ 0 & 0 & 0 & 1.0000 & 0 & 0 \\ 0 & 0 & 0 & 0 & 1.0000 & 0 \\ 0 & 0 & 0 & 0 & 0 & 1.0000 \end{bmatrix}$$

$$MS_{pr} = \begin{bmatrix} 1.0000 & 0 & 0 & 0 & 0.5469 & -0.5070 \\ 0 & 1.0000 & 0 & -0.5469 & 0 & 1.4083 \\ 0 & 0 & 1.0000 & 0.5070 & -1.4083 & 0 \\ 0 & 0 & 0 & 1.0000 & 0 & 0 \\ 0 & 0 & 0 & 0 & 1.0000 & 0 \\ 0 & 0 & 0 & 0 & 0 & 1.0000 \end{bmatrix}$$

Table B1 shows a comparison of inertial properties for the different models. The aircraft masses for the finite-element models are lower than the flight test data. This reflects the fact that not all components in the aircraft were modeled (e.g., the data acquisition bay). As a result, aircraft moments of inertia and cg position differ noticeably as well. The differences between the two finite-element models are less pronounced. This exercise clearly indicates that the SAMCEF and S02 finite-element models could be improved.

Table B1. Comparison of SAMCEF, S02, and flight test rigid airframe inertial properties

	SAMCEF	S02	Flight test
Aircraft mass (kg)	1907	1879	1945-1999
Aircraft moments of inertia (kg-m ²)			
I _{xx}	1181	1142	800
I _{yy}	3839	3755	4200
I _{zz}	3085	3050	3600
I _{xy}	0	0	0
I _{xz}	689	683	680
I _{yz}	0	0	0
Center of gravity position, R-frame (m)			
FS	-0.036	-0.045	-0.090
WL	-1.479	-1.492	-1.320
BL	0.005	0.005	0

APPENDIX C

Derivation of the SAMCEF Rotation Mode Shapes

The calculated SAMCEF data set did not include the rotation mode shapes at the hub. The hub rotations were derived from the translation mode shapes at two locations on the mast. Assuming that the rotor mast is rigid, the rotation mode shapes of two nodes located on the mast are the same. For this analysis, two nodes were chosen sufficiently far from each other to avoid numerical inaccuracy, but sufficiently close to uphold the assumption of rigidity: the hub (node 667) and the midpoint of the rotor mast (node 668). The mode shape vectors of nodes 667 and 668 can be expressed in the F-frame as

$$\{MS_{667}\} = \begin{bmatrix} \xi_{667_x} \\ \xi_{667_y} \\ \xi_{667_z} \\ \gamma_{667_x} \\ \gamma_{667_y} \\ \gamma_{667_z} \end{bmatrix} \quad \{MS_{668}\} = \begin{bmatrix} \xi_{668_x} \\ \xi_{668_y} \\ \xi_{668_z} \\ \gamma_{668_x} \\ \gamma_{668_y} \\ \gamma_{668_z} \end{bmatrix}$$

where ξ represents the linear mode shapes, and γ the rotation mode shapes. Equating the rotation mode shapes yields

$$\begin{bmatrix} \gamma_{668_x} \\ \gamma_{668_y} \\ \gamma_{668_z} \end{bmatrix} = \begin{bmatrix} \gamma_{667_x} \\ \gamma_{667_y} \\ \gamma_{667_z} \end{bmatrix}$$

Assuming that the lateral and longitudinal hub perturbations, which are proportional to the mode shapes, are small compared to the distance (r_z) between the two nodes on the mast, we can write an expression for the rotation mode shapes in terms of the translation mode shapes:

$$\begin{aligned} \gamma_{667_y} &= (\xi_{668_x} - \xi_{667_x}) / r_z \\ \gamma_{667_x} &= -(\xi_{668_y} - \xi_{667_y}) / r_z \end{aligned}$$

Since the drive train is not modeled with SAMCEF, the rotation mode shape γ_{667_z} equals 0.

The results are listed in table 5. This procedure was validated by applying it to the S02 vibration model. The amplitude and direction of the resulting rotation mode shapes agreed with the S02 predictions to within 15% and 10°, respectively.

REFERENCES

1. Johnson, W.: Recent Developments in the Dynamics of Advanced Rotor Systems. NASA TM-86669, March 1985.
2. Cronkhite, J. D.: Development, Documentation, and Correlation of a NASTRAN Vibration Model of the AH-1G Helicopter Airframe. NASA TM-X-3428, Oct. 1976.
3. Gabel, R., Reed, D.; Ricks, R.; and Kesack, W.: Planning, Creating, and Documenting a NASTRAN Finite Element Model of a Modern Helicopter. American Helicopter Society Specialists' Meeting on Rotorcraft Dynamics, Moffett Field, California, Nov. 1984.
4. Reichert, G.: Helicopter Vibration Control – A Survey. Vertica, vol. 5, no. 1, 1981.
5. Polychroniadis, M.; and Achache, M.: Higher Harmonic Control: Flight Tests of an Experimental System on SA349 Research Gazelle. American Helicopter Society 42nd Annual National Forum, Washington, DC, June 1986.
6. Molusis, J. A.; Hammond, C. E.; and Cline, J. H.: A Unified Approach to the Optimal Design of Adaptive and Gain Scheduled Controllers to Achieve Minimum Helicopter Rotor Vibration. J. American Helicopter Society, vol 28, no. 2, April 1983.
7. Heffernan, R.; Yamauchi, G.; Gaubert, M.; and Johnson, W.: Hub Loads Analysis of the SA349/2 Helicopter. NASA TM-101061, Dec. 1988.
8. Heffernan, R.; and Gaubert, M.: Structural and Aerodynamic Loads and Performance Measurements of an SA349/2 Helicopter with an Advanced Geometry Rotor. NASA TM-88370, Nov. 1986.
9. Yamauchi, G.; Heffernan, R.; and Gaubert, M.: Hub and Blade Structural Loads Measurements of an SA349/2 Helicopter. NASA TM-101040, Dec. 1988.
10. Johnson, W.: CAMRAD/JA, A Comprehensive Analytical Model of Rotorcraft Aerodynamic and Dynamics, Vol. 1: Theory Manual. Johnson Aeronautics, 1988.

Table 1. SA349/2 helicopter data

Rotor radius (m):	5.25
Number of blades:	3
Rotor solidity:	0.0637
Design aircraft mass (kg):	2000.0
Design main rotor rotational speed (rpm):	387.0
Estimated aircraft moments of inertia (kg m ²): (referenced to F-frame, see fig. 1)	
I _{xx} =	800.0
I _{yy} =	4200.0
I _{zz} =	3600.0
I _{xy} =	0.0
I _{xz} =	680.0
I _{yz} =	0.0
Shaft angle of attack (deg): (positive rearward)	-4.0
Aircraft cg location (m): (referenced to R-frame, see fig. 1)	
FS (fuselage station) =	-0.09
BL (butt line) =	0.0
WL (water line) =	-1.32
Pilot seat accelerometer location (m): (referenced to R-frame, see fig. 1)	
FS (fuselage station) =	-1.63
BL (butt line) =	0.61
WL (water line) =	2.02

Table 2. Flight parameters for selected conditions

Flight condition	V3101	V3103	V3105	V3106	V3109	V3111
Altitude (m)	306.2	276.7	317.2	342.2	527.5	503.4
True air speed (m/s)	30.2	56.4	74.4	79.0	51.4	55.4
Load factor	1.0	1.0	1.0	1.0	1.5	1.9
μ	0.14	0.26	0.35	0.37	0.24	0.26
C_T/σ	0.066	0.066	0.063	0.066	0.096	0.125
Aircraft mass (kg)	1999.0	1991.0	1979.0	1973.0	1955.0	1945.0
M_{at}	0.73	0.81	0.86	0.87	0.79	0.80

Table 3. Measured 3/rev hub loads and pilot seat accelerations

Hub forces (N)-nonrotating frame

Flt. no.	H, 3/rev		Y, 3/rev		T, 3/rev	
	A ₃	B ₃	A ₃	B ₃	A ₃	B ₃
V3101	-296	123	-79	-167	1306	-1081
V3103	69	164	19	16	-801	-2293
V3105	122	-88	415	238	-115	-4593
V3106	52	-287	572	298	-290	-5594
V3109	-360	464	21	-278	-1836	-2305
V3111	-553	958	238	-451	-4085	-1616

Hub moments (Nm)-nonrotating frame

Flt. no.	M _x , 3/rev		M _y , 3/rev		Q, 3/rev	
	A ₃	B ₃	A ₃	B ₃	A ₃	B ₃
V3101	-7	-9	46	68	168	-39
V3103	-16	22	-10	-45	51	-176
V3105	-90	115	-79	-195	46	-430
V3106	-117	185	-114	-221	0	-565
V3109	56	-1	72	97	94	-143
V3111	224	59	7	208	68	-249

Pilot seat acceleration(g)

Flt. no.	Pilot accelerating (g)	
	A ₃	B ₃
V3101	0.0774	0.0374
V3103	0.0157	-0.0193
V3105	-0.0978	-0.0812
V3106	-0.1747	-0.0605
V3109	0.1227	0.0179
V3111	0.0135	0.021

Table 4. Vibration characteristics for an SA34 1 obtained with S02 code (F-frame)

a) General modal characteristics

Mode no.	Freq. (Hz)	Mass (Kg)	Mode identification
1	0	206.8	(coupled rigid modes)
2	0	178.6	
3	0	337.1	
4	0	260.1	
5	0	151.5	
6	0	1622.8	
7	4.97	235.5	Engine roll
8	7.96	85.4	1st fuselage vertical bending
9	9.79	185.1	Longitudinal suspension
10	9.99	63.8	1st fuselage lateral bending
11	11.22	276.6	Vertical engine
12	11.39	413.3	Lateral suspension
13	17.59	445.4	1st fuselage torsion
14	17.76	502.7	Fuselage + fuel tank
15	20.92	275.5	2nd fuselage vertical bending

b) Linear and rotation mode shapes at the hub

Mode no.	ζ_x m/m	ζ_y m/m	ζ_z m/m	γ_x rad/m	γ_y rad/m	γ_z rad/m
1	0.0089	0.14895	-0.00217	0.26	-0.01	0.16
2	-0.1322	0.04801	0.2429	0.03	0.13	0
3	-0.07712	-0.91187	0.01066	-0.47	0.04	-0.01
4	-0.32005	0.06936	-0.21753	0.05	0.21	-0.01
5	-0.04212	0.14975	0.00549	0.01	0.01	0.2
6	0.98681	-0.09828	-0.1664	-0.05	-0.05	0.06
7	-0.00132	-0.35295	0.00167	-0.34	0	0.03
8	-0.14217	0.01589	0.05841	0.02	0.15	-0.01
9	0.54224	0.02696	0.12235	0.06	-0.66	0
10	0.01819	-0.18382	0.00471	-0.43	-0.02	0.08
11	-0.44147	0.01097	0.11474	0.05	0.6	0.02
12	0.01331	0.51006	-0.02507	1.88	-0.02	0.22
13	-0.20366	-0.11493	0.01274	-1.04	0.49	0.09
14	0.20151	-0.10922	-0.04708	-1.07	-0.47	0.11
15	-0.16733	-0.00298	-0.55483	0.01	0.6	0.03

Table 4. Concluded

c) Linear mode shapes at the pilot seat

Mode no.	ζ_x m/m	ζ_y m/m	ζ_z m/m
1	-0.09232	-0.15469	0.14644
2	0.13503	-0.02599	0.0703
3	-0.00131	0.03784	-0.28357
4	0.10327	-0.03618	-0.49487
5	-0.11155	0.40751	-0.00982
6	0.84683	0.11092	-0.12089
7	-0.016	-0.00661	-0.03565
8	0.02515	-0.01509	-0.23152
9	-0.152	-0.01098	-0.35544
10	-0.08541	0.18196	-0.15547
11	0.04	0.03344	-0.04834
12	-0.11787	0.22746	-0.54042
13	-0.06691	-0.12607	-0.39674
14	-0.08599	-0.17019	-1
15	-0.11187	0.04341	0.38343

Table 5. Vibration characteristics for an SA349/2 obtained with SAMCEF code (F-frame)

a) General modal characteristics

Mode no.	Freq. (Hz)	Mass (Kg)	Mode identification
1	0	1907.7	(coupled rigid modes)
2	0	851.8	
3	0	316.4	
4	0	738.6	
5	0	69.7	
6	0	89.7	
7	5.31	59	Engine roll
8	7.46	186.5	Lateral suspension
9	8.04	86	1st fuselage vertical bending
10	9.46	98.9	1st fuselage lateral bending
11	9.57	182	Longitudinal mast bending
12	11.46	64.4	Vertical engine
13	14.97	330.7	Longitudinal Suspension
14	16.86	226.1	1st fuselage torsion
15	18.61	407.9	2nd fuselage vertical bending
16	20.03	85.8	2nd fuselage lateral bending
17	20.61	148.9	Lateral engine + mast
18	20.76	189.6	Fuel tank
19	21.9	335.1	Fuselage + fuel tank
20	25.06	75.6	2nd fuselage torsion

Table 5. Continued

b) Linear and rotation mode shapes at the hub

Mode no.	ζ_x m/m	ζ_y m/m	ζ_z m/m	γ_x rad/m	γ_y rad/m	γ_z rad/m
1	1	0	0	0	0	0
2	0.1912	0	0.6378	0	-0.1293	0
3	0.0006	-0.8965	0.0031	-0.5131	-0.0006	-0.0621
4	-0.0009	-0.2061	-0.0014	0.2402	0.0003	-0.0979
5	0.0006	0.0469	-0.0005	0.0665	0.0001	0.1556
6	-0.2173	0.0023	0.0649	0.0016	0.147	0.0006
7	0.002	0.1441	-0.0016	0.0919	0.0004	0
8	-0.2595	0.3814	0.018	1.2655	0.4798	0
9	0.084	0.1253	-0.063	0.5093	-0.0048	0
10	-0.1132	0.0027	-0.0091	0.3266	0.2055	0
11	-0.5375	-0.0822	-0.1173	-0.3096	0.6662	0
12	-0.175	-0.0315	0.0566	-0.0964	0.296	0
13	-0.2306	-0.1077	-0.1213	0.2044	1.2094	0
14	-0.1143	-0.0521	-0.0832	-0.7979	0.4651	0
15	-0.051	0.0435	-0.107	0.1517	-0.2688	0
16	0.012	0.0035	0.0083	0.2887	-0.0661	0
17	-0.0268	0.0059	-0.004	-0.3598	0.0679	0
18	-0.0032	-0.0001	0.0279	0.1418	-0.0216	0
19	-0.0372	-0.0049	0.6683	-0.0212	0.0432	0
20	-0.03	0.0035	0.0248	-0.0929	0.044	0

Table 5. Concluded

c) Linear mode shapes at the pilot seat

Mode no.	ζ_x m/m	ζ_y m/m	ζ_z m/m
1	1	0	0
2	-0.0725	0	0.8258
3	0.0419	0.0594	-0.3475
4	0.0667	-0.8382	0.1628
5	-0.1057	0.1374	0.0449
6	0.082	0	-0.1478
7	0.001	0.0161	0.0424
8	0.1143	-0.124	-0.489
9	-0.02	0.0058	0.0685
10	-0.1329	0.2271	-0.0034
11	0.1663	-0.0298	0.3995
12	0.0019	0.0039	0.0132
13	-0.1028	0.0677	0.5308
14	-0.1269	-0.1165	-0.5603
15	0.0652	0.0518	0.5436
16	0.0299	0.0613	-0.0025
17	-0.0343	-0.0596	-0.0729
18	0.0237	0.0223	-0.0301
19	0.0666	-0.022	-0.2649
20	-0.0339	0.0491	-0.0948

Table 6. Matrix of CAMRAD/JA model configurations for predicting hub loads and pilot seat vertical acceleration

Model configuration	1	2	3	4	5	6	7	8	9	10
S02 elastic fuselage model						x	x	x	x	x
SAMCEF elastic fuselage model	x	x	x	x	x					
WITH rotation mode shapes	x	x	x	x		x	x	x	x	
WITHOUT rotation mode shapes					x					x
Uniform Inflow	x		x			x		x		
Non-Uniform Inflow prescribed wake		x		x	x		x		x	x
WITH rotor/fuselage feedback			x	x	x			x	x	x
WITHOUT rotor/fuselage feedback	x	x				x	x			

Table 7. Matrix of forced response model configurations for predicting pilot seat vertical acceleration from the measured hub loads

Model configuration	a	b	c	d
S02 elastic fuselage model			x	x
SAMCEF elastic fuselage model	x	x		
WITH rotation mode shapes	x		x	
WITHOUT rotation mode shapes		x		x

Table 8. Summary of changes to SAMCEF model to reduce vibration from measured hub loads

Mode #	Frequency % change	Damping % critical
15	25	9
19	-5	9
all others	0	3

Table 9. Summary of changes to SAMCEF model to reduce vibration from calculated hub loads

Mode #	Frequency % change	Damping % critical
14	-10	9
15	-7	1.5
19	-15	6
all others	0	3

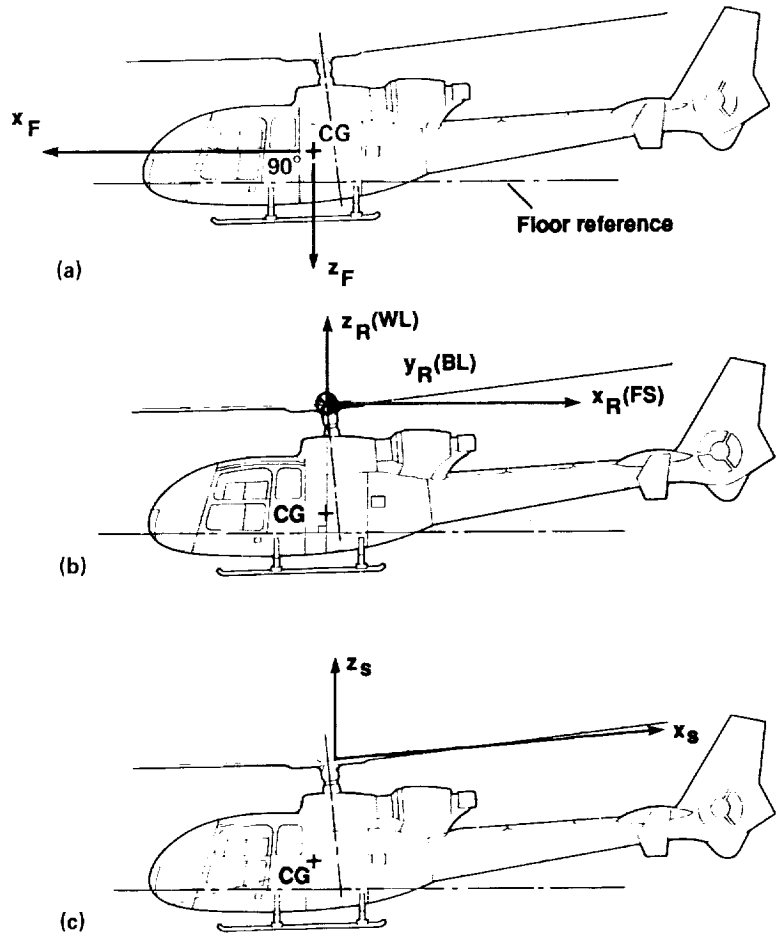


Figure 1. Aircraft reference axis systems. a) Body axes (F-frame), b) rotor axes (R-frame), c) shaft axes (S-frame).

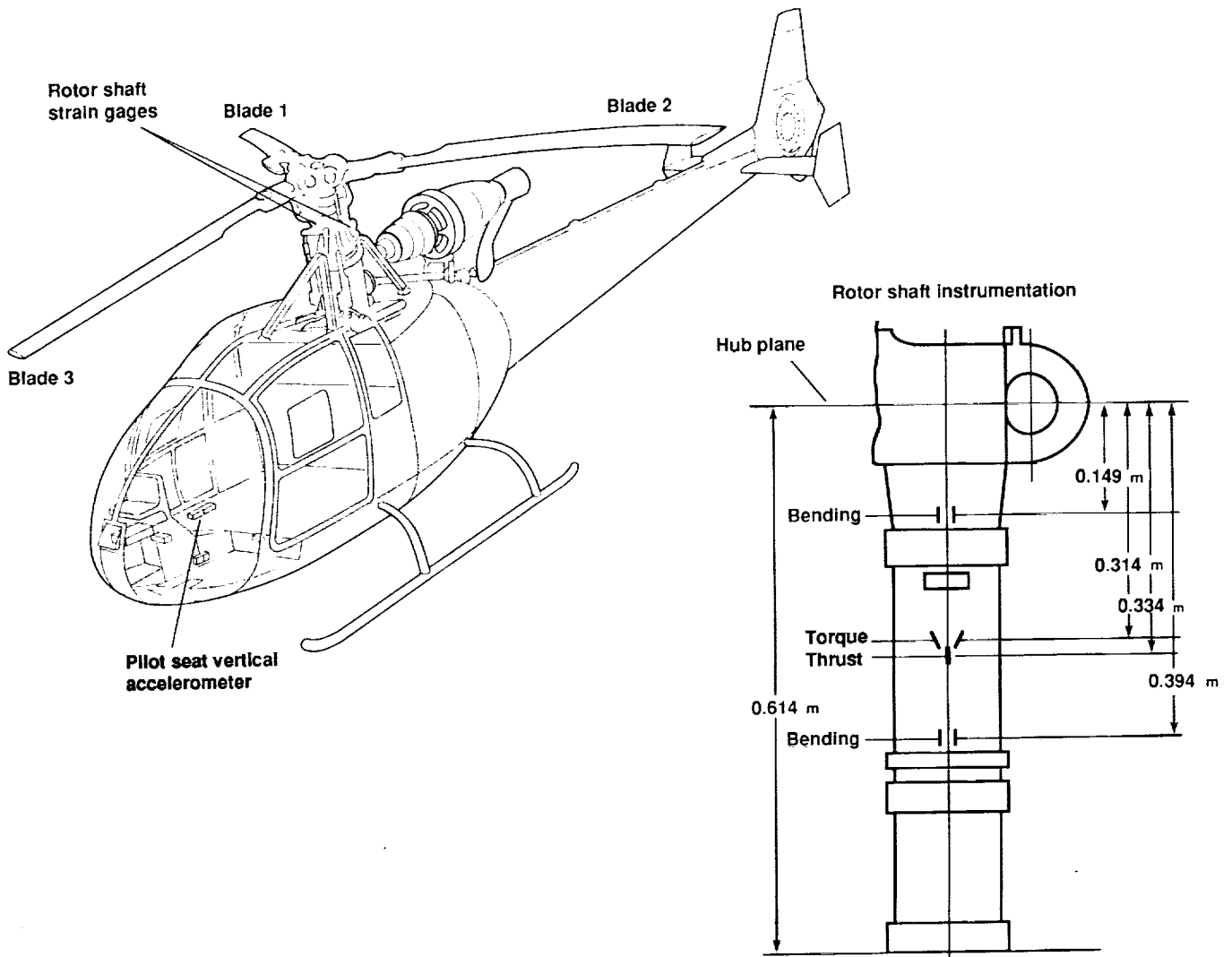


Figure 2. Aircraft instrumentation.

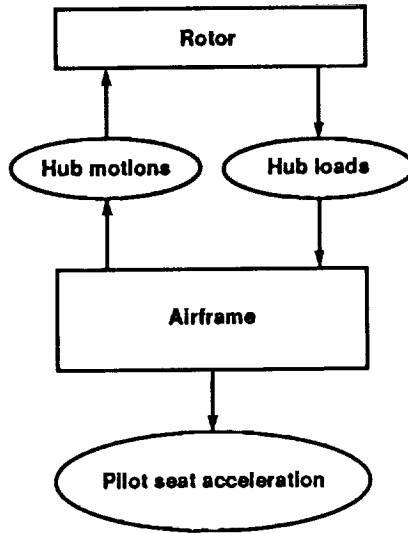


Figure 3. Schematic of the coupling between the rotor and fuselage.

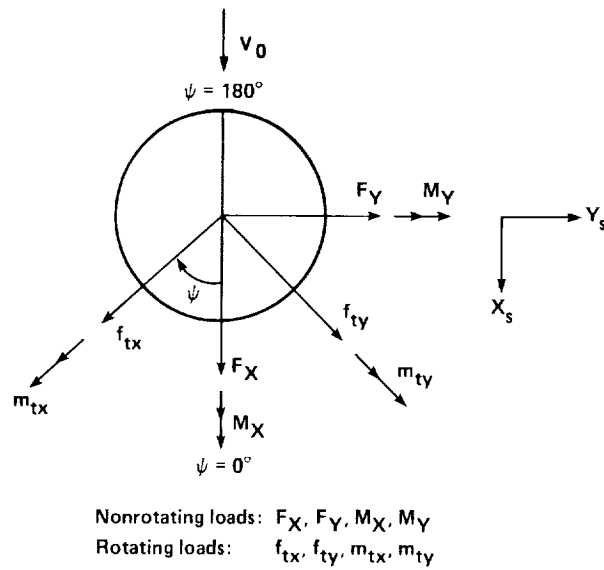


Figure 4. Relationship between rotating and nonrotating-frame hub loads. F_Z, f_{tz}, M_Z and m_{tz} point out of the page.

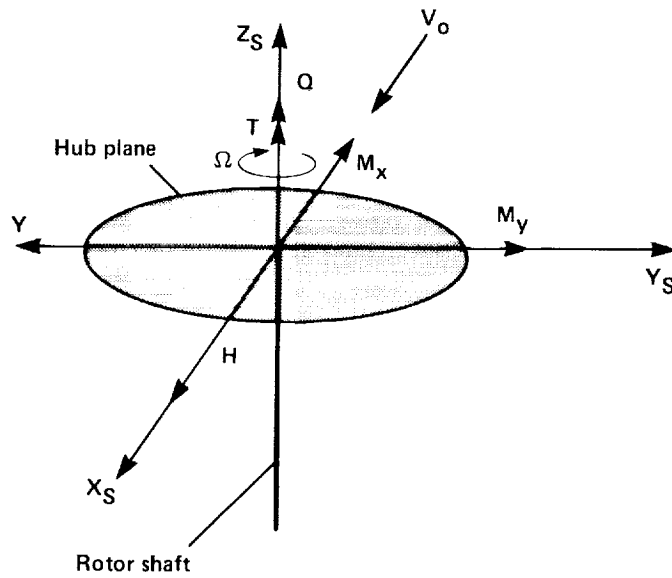


Figure 5. Hub force and moment diagram.

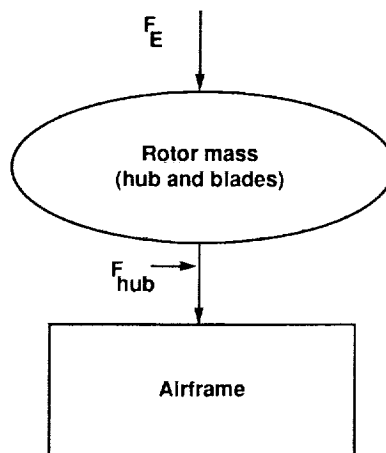


Figure 6. Schematic of helicopter structural model showing placement of hub loads, F_{hub} , and of the fuselage excitation input, F_E .

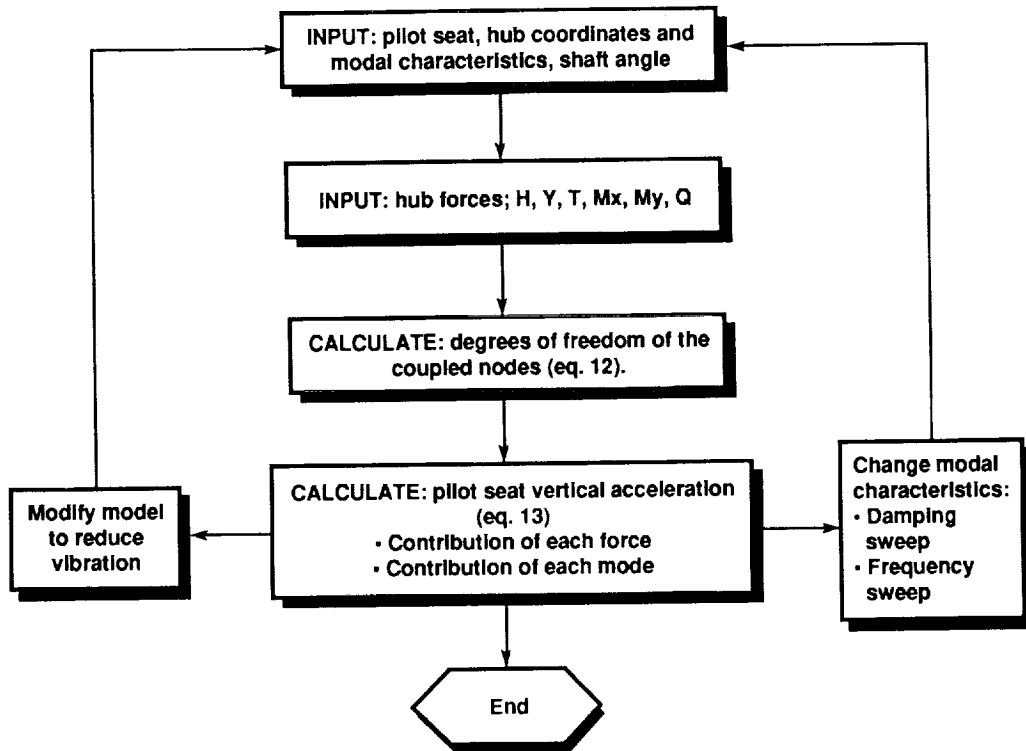


Figure 7. Schematic of the forced response program tasks.

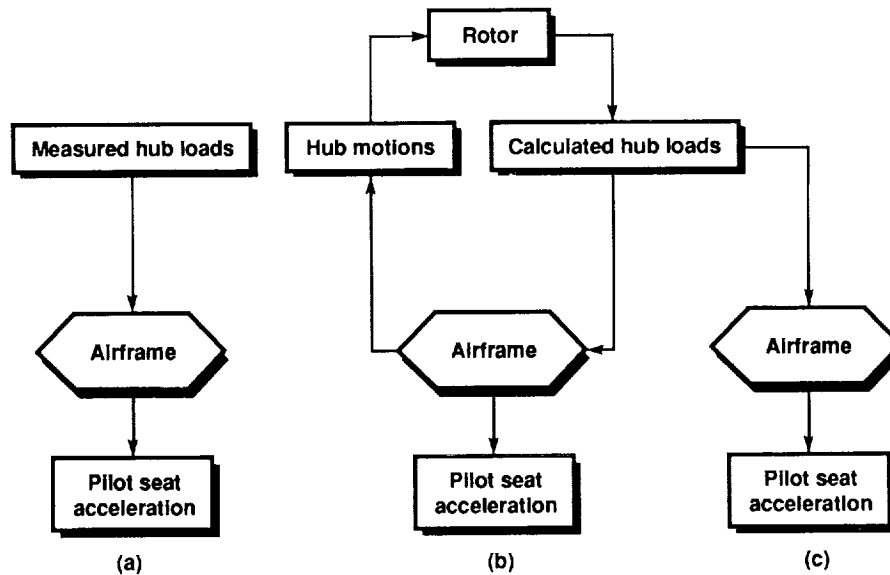


Figure 8. Schematic of three methods of obtaining the pilot-seat acceleration. a) measured hub loads input to the forced response program, b) hub loads and acceleration predicted by CAMRAD/JA, and c) predicted hub loads input to the forced response program.

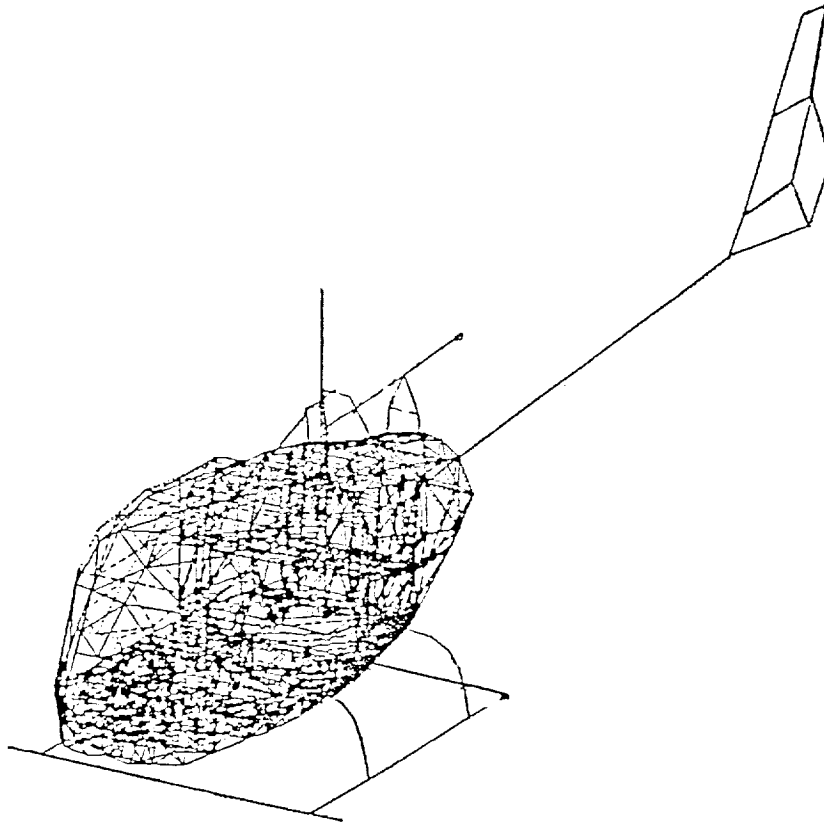


Figure 9. Finite-element model used in the SAMCEF analysis.

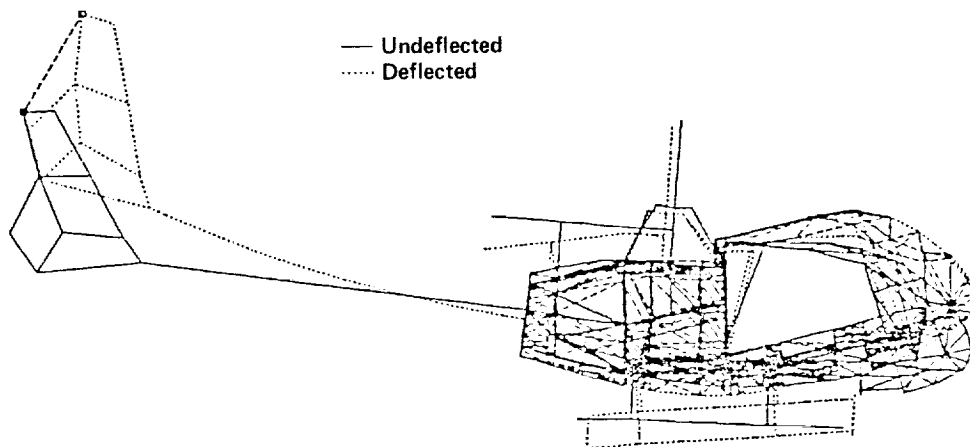


Figure 10. Deflection of the first vertical bending mode.

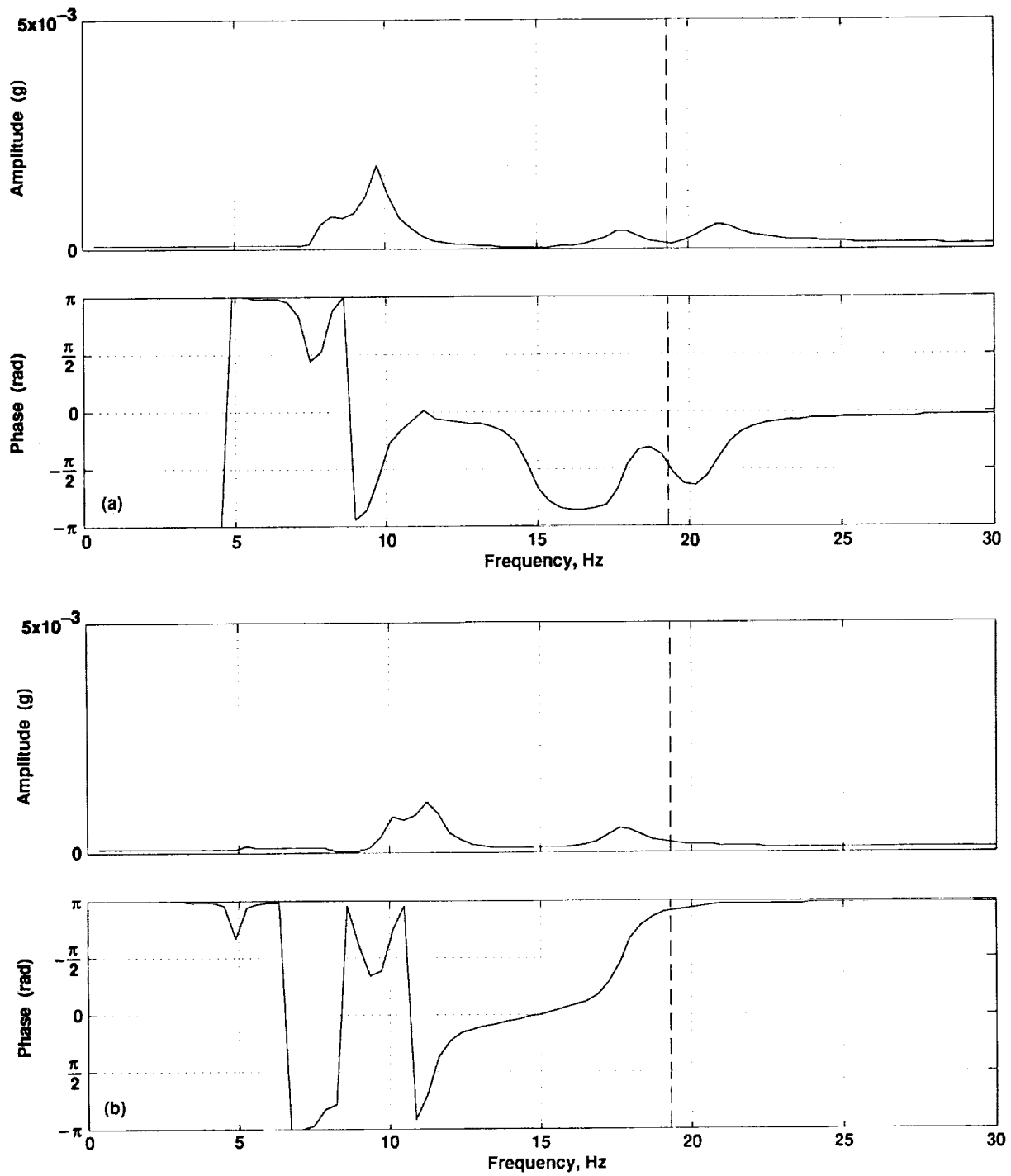


Figure 11. Frequency response (magnitude and phase) of the S02 model to unit hub forces and moments. a) H, b) Y.

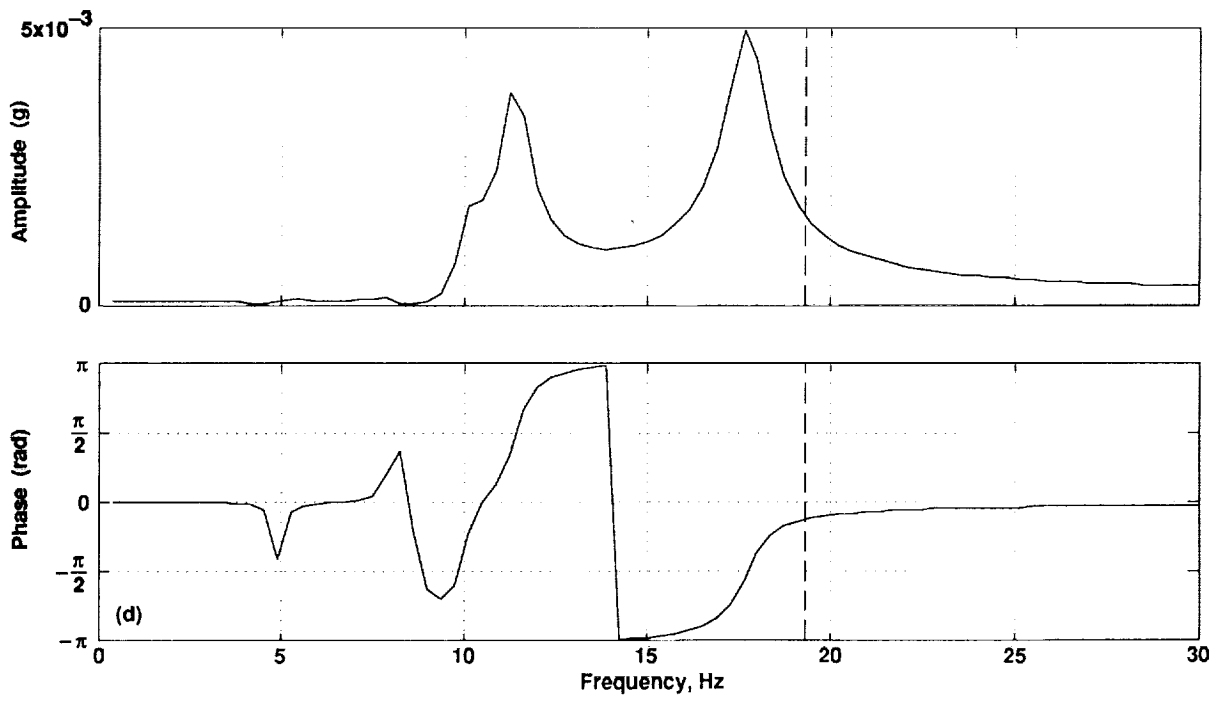
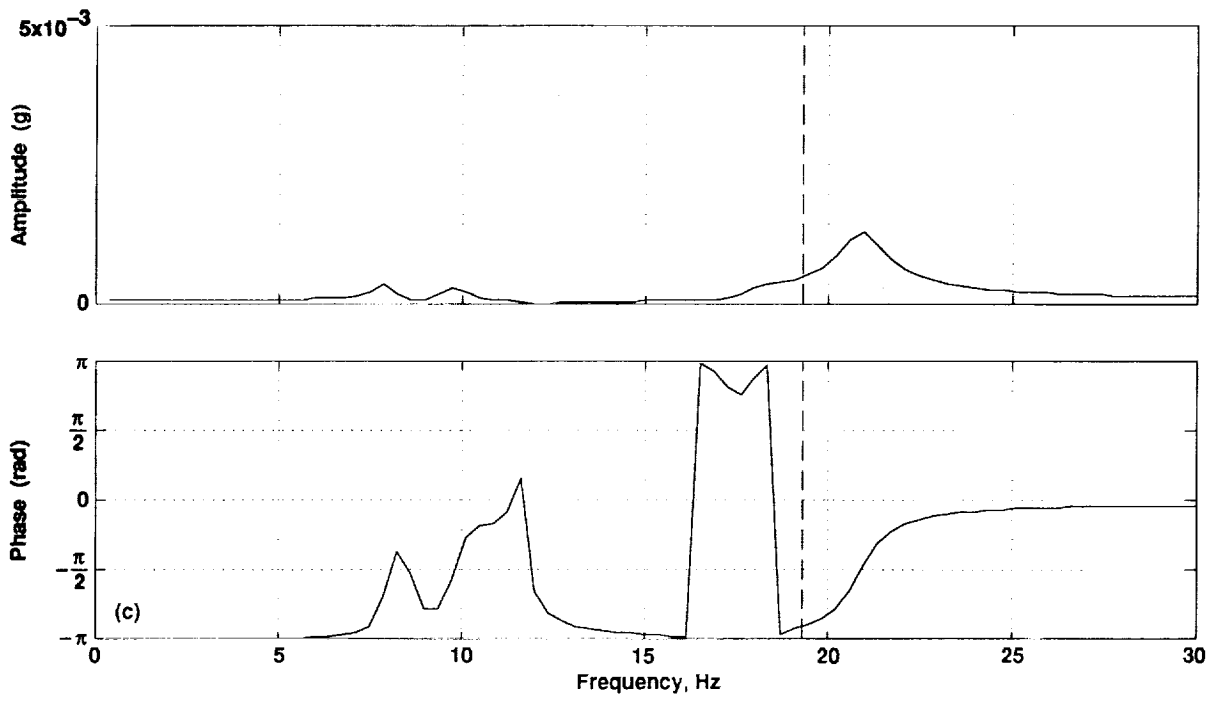


Figure 11. Continued. c) T, d) M_x .

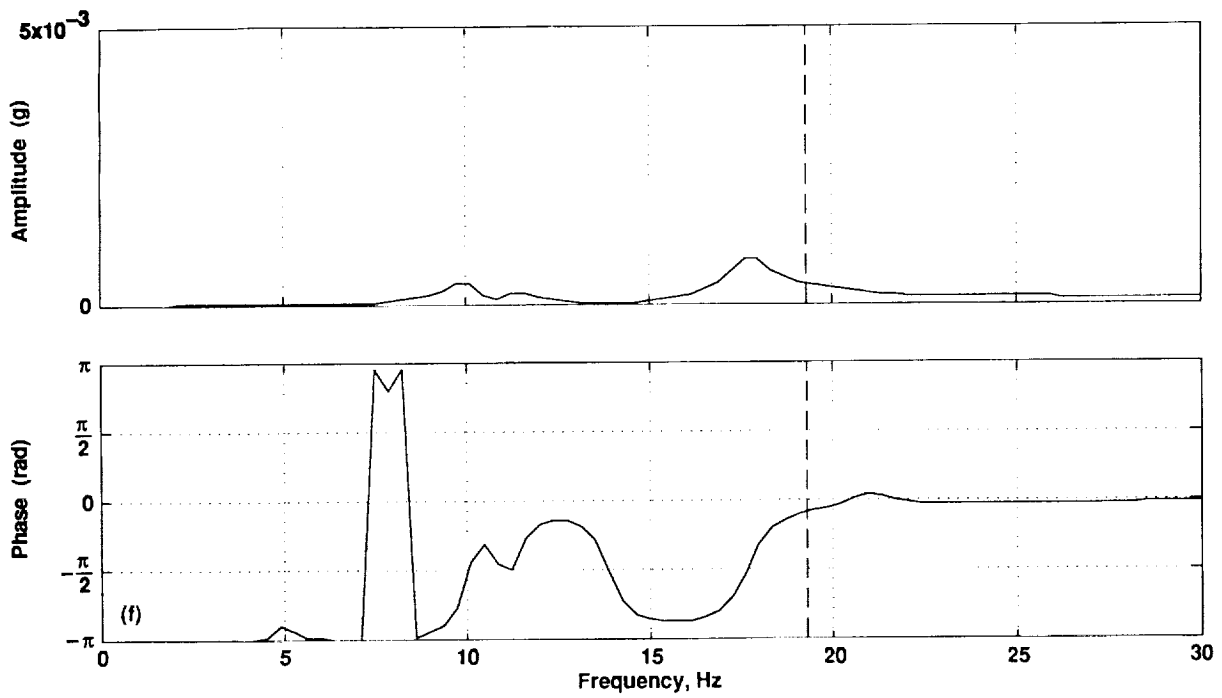
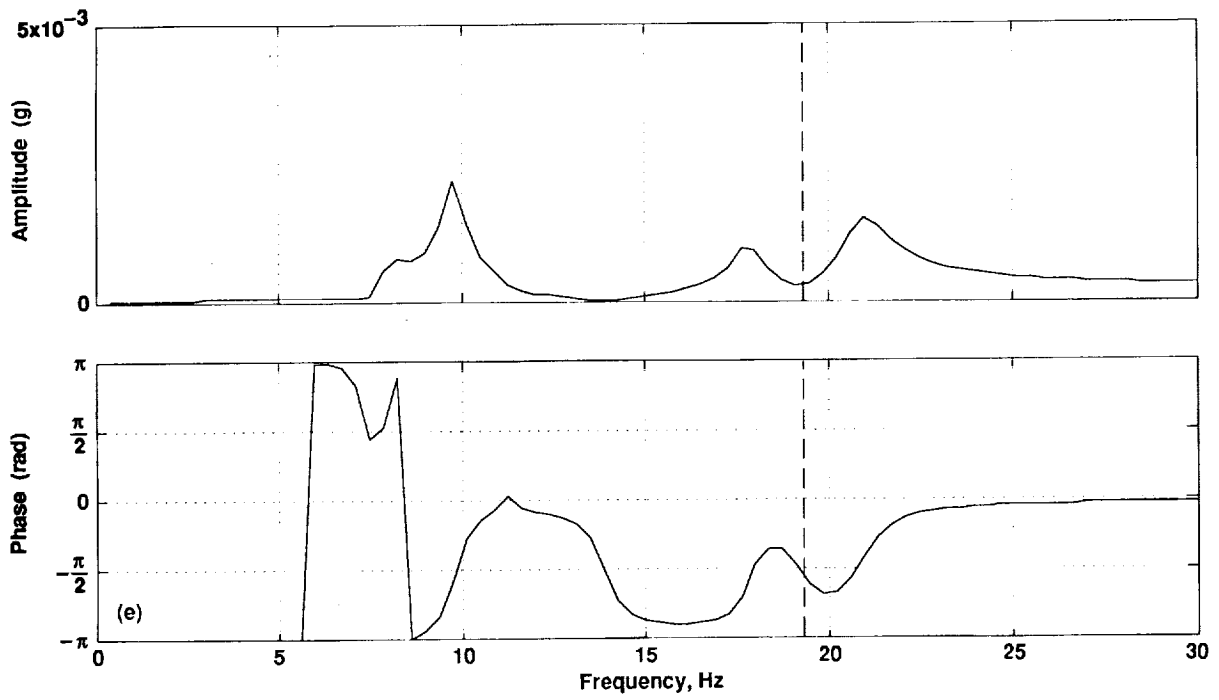


Figure 11. Concluded. e) M_y , f) Q .

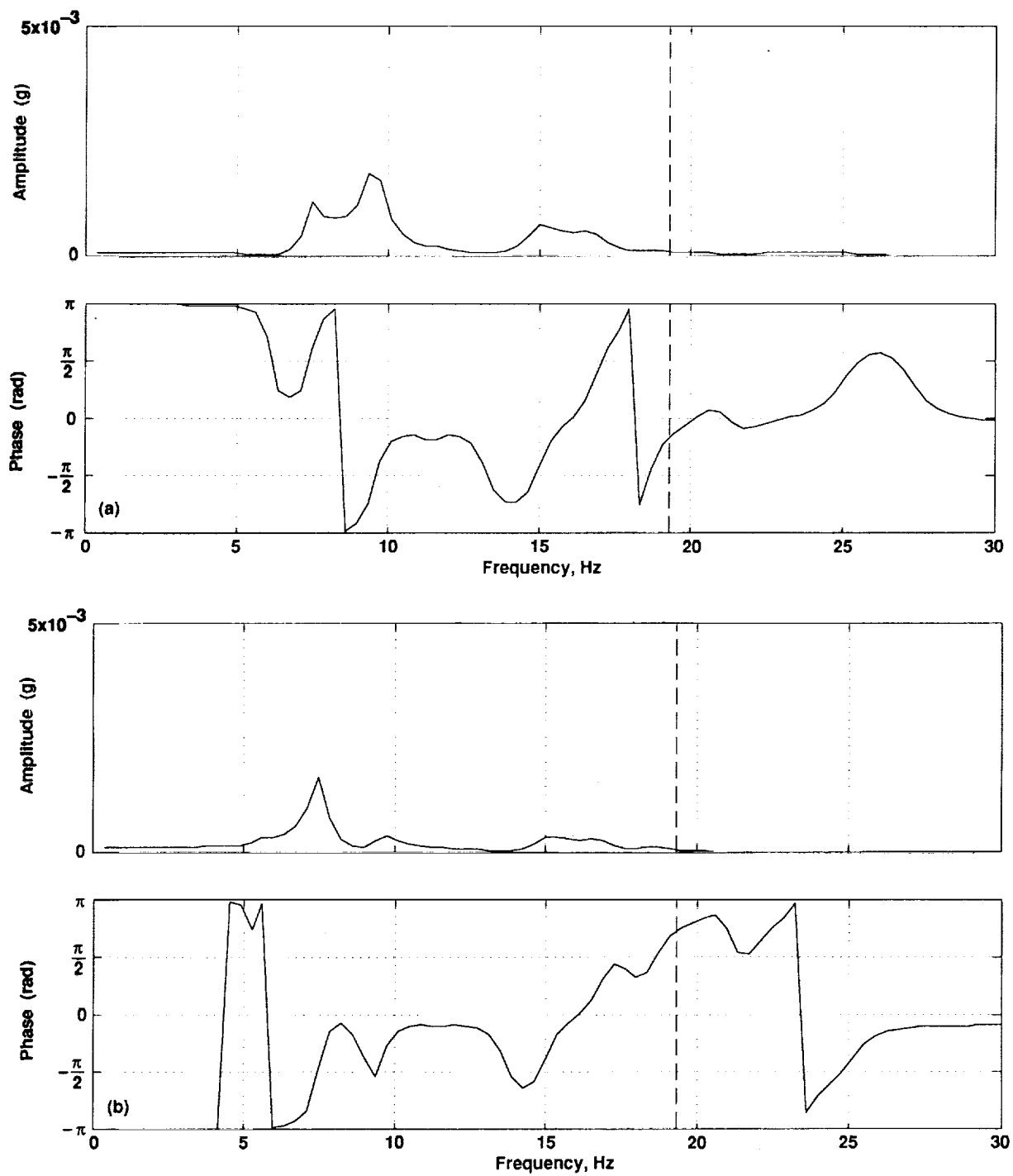


Figure 12. Frequency response (magnitude and phase) of the SAMCEF model to unit hub forces and moments. a) H, b) Y.

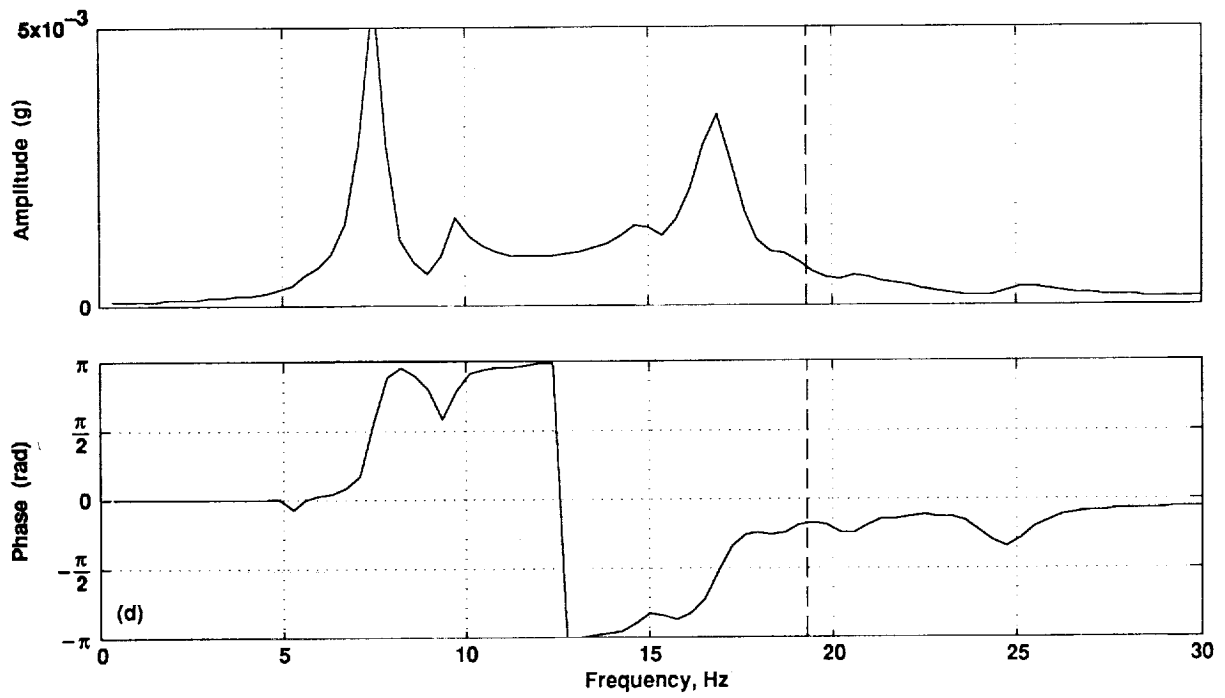
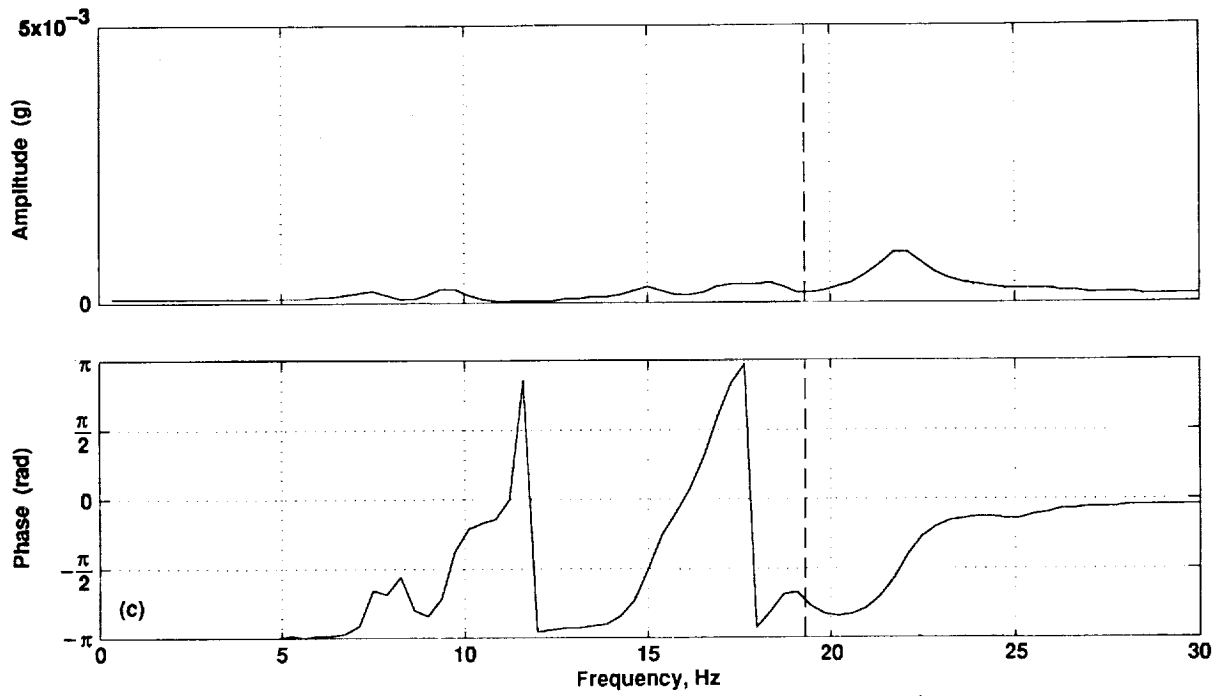


Figure 12. Continued. c) T, d) M_x .

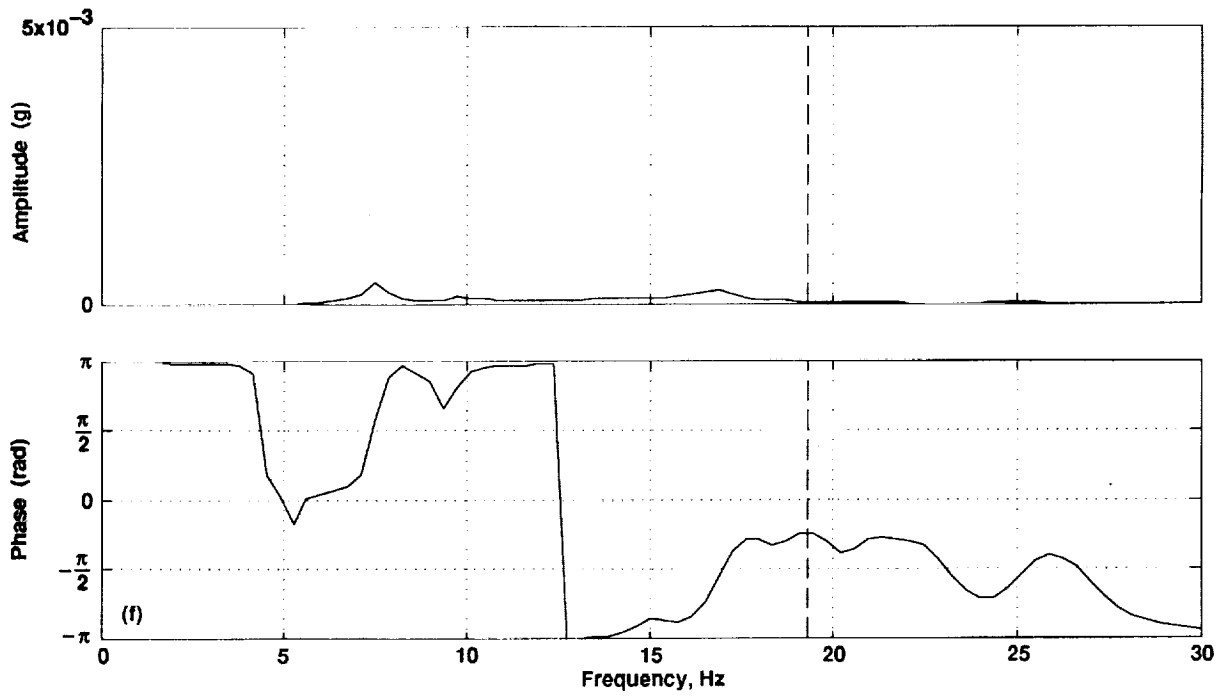
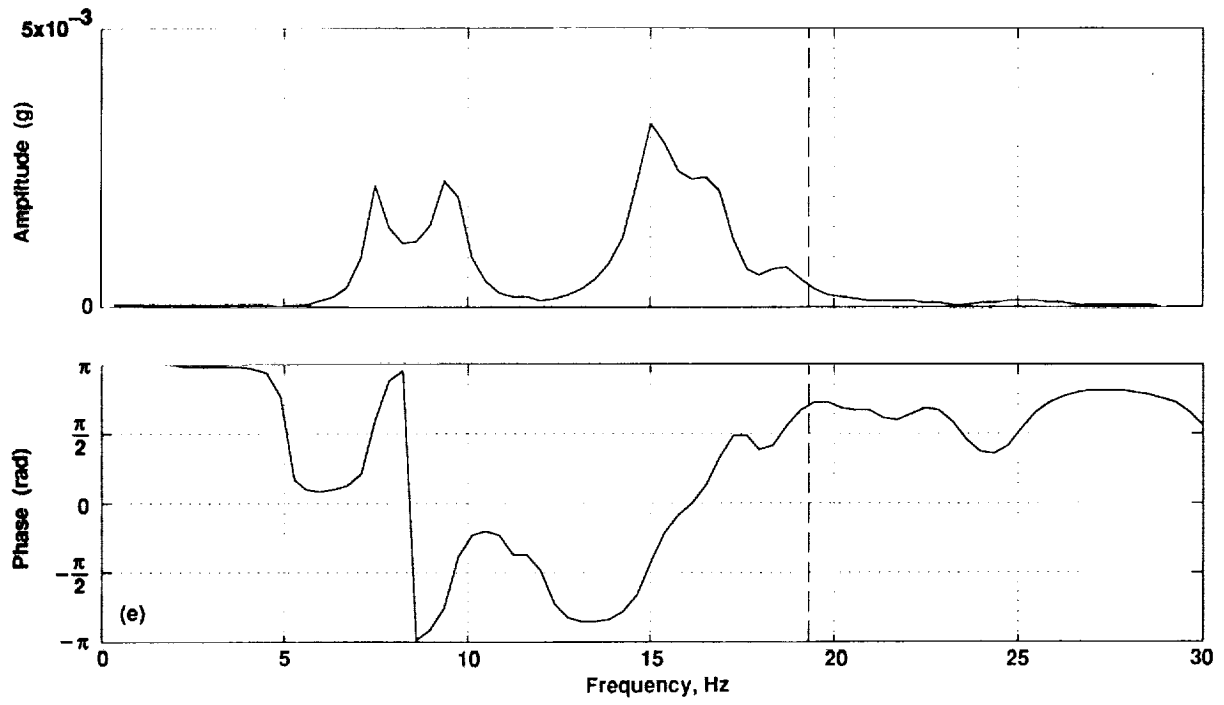


Figure 12. Concluded. e) M_y , f) Q .

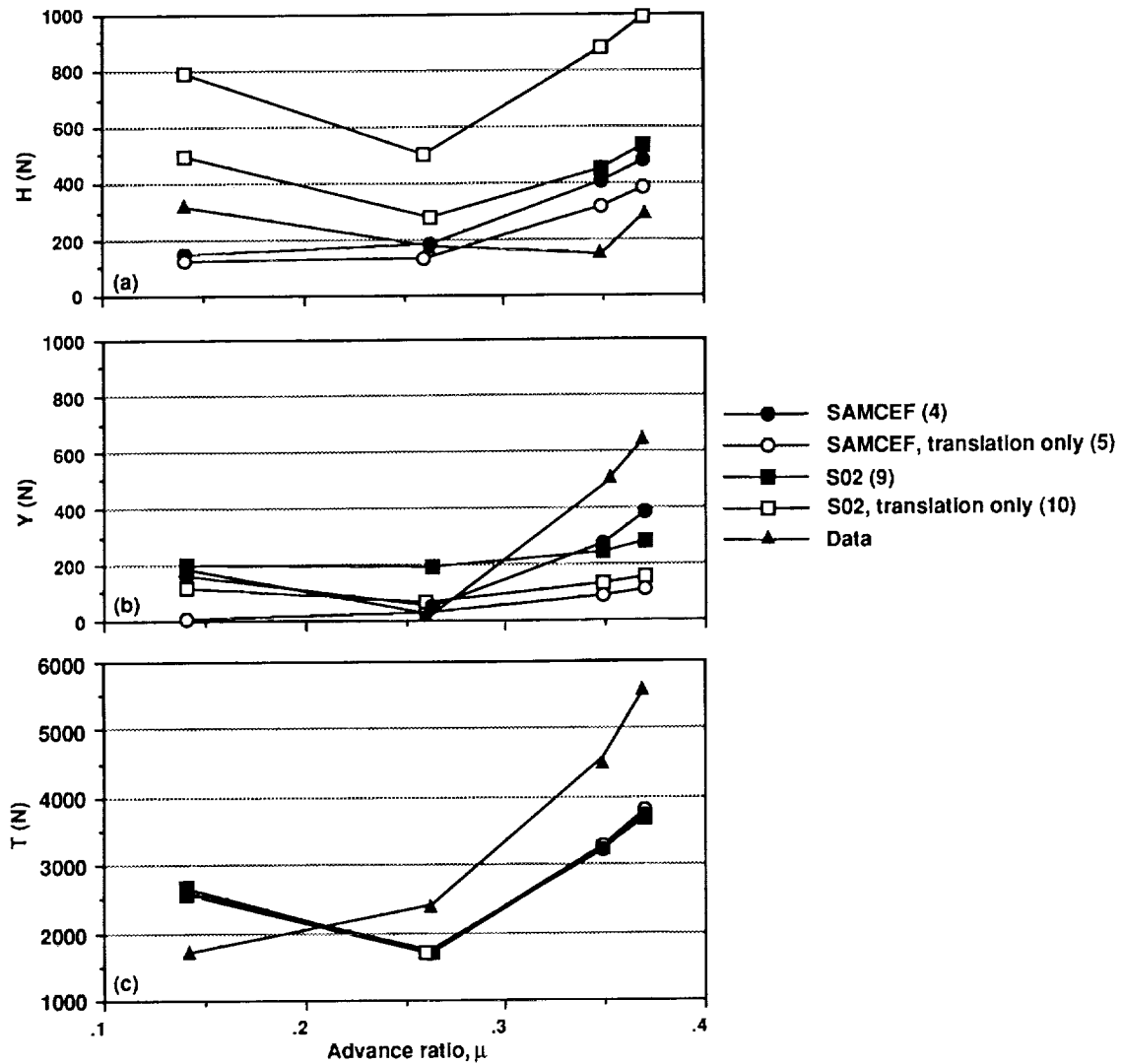


Figure 13. Correlation of measured and predicted 3/rev hub loads. Magnitudes only. Hub loads were predicted using the S02 and SAMCEF models, with and without rotation mode shapes, for the four level flight conditions. Numbers in () indicate model configuration (see table 6). a) H, b) Y, c) T.

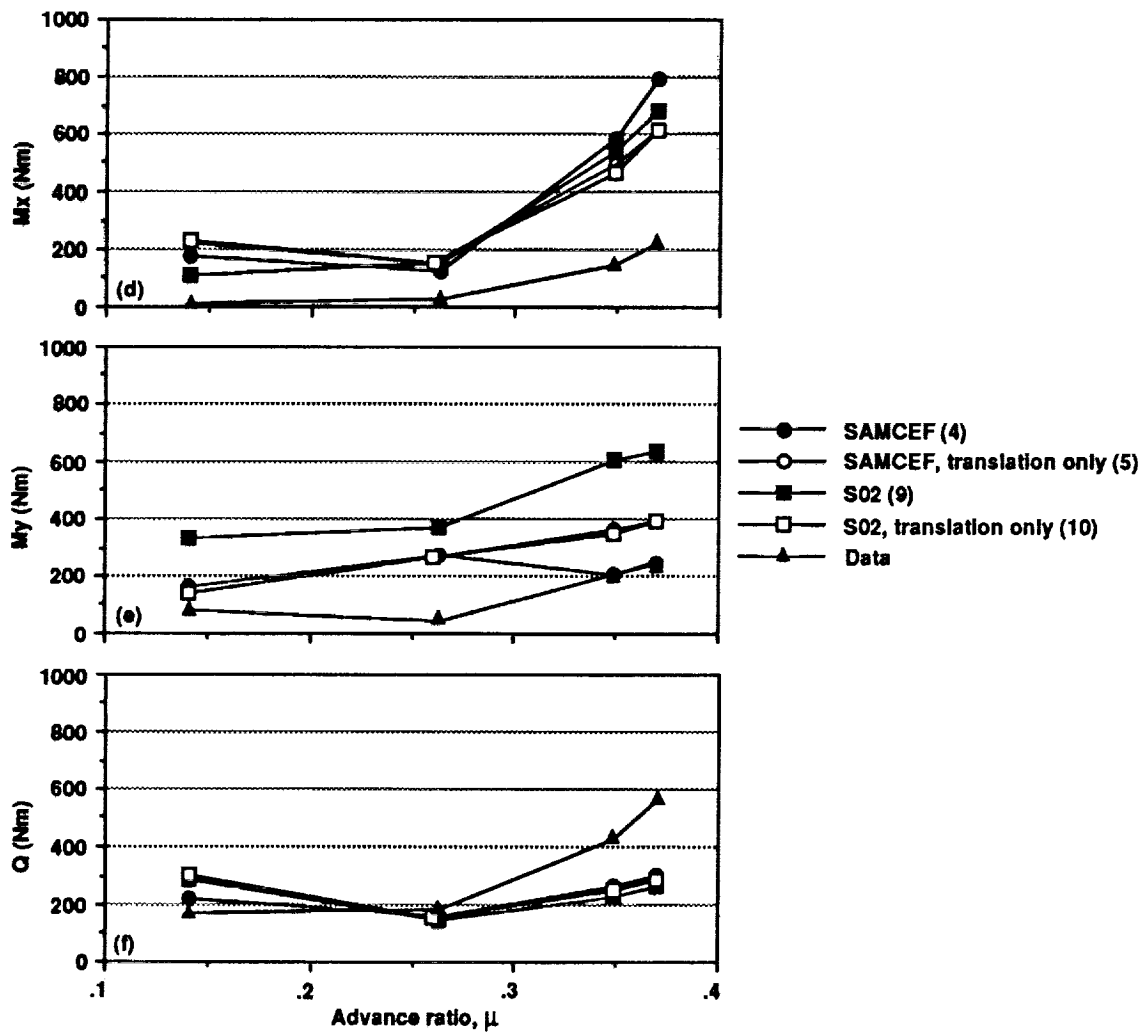


Figure 13. Concluded. d) M_x , e) M_y , f) Q .

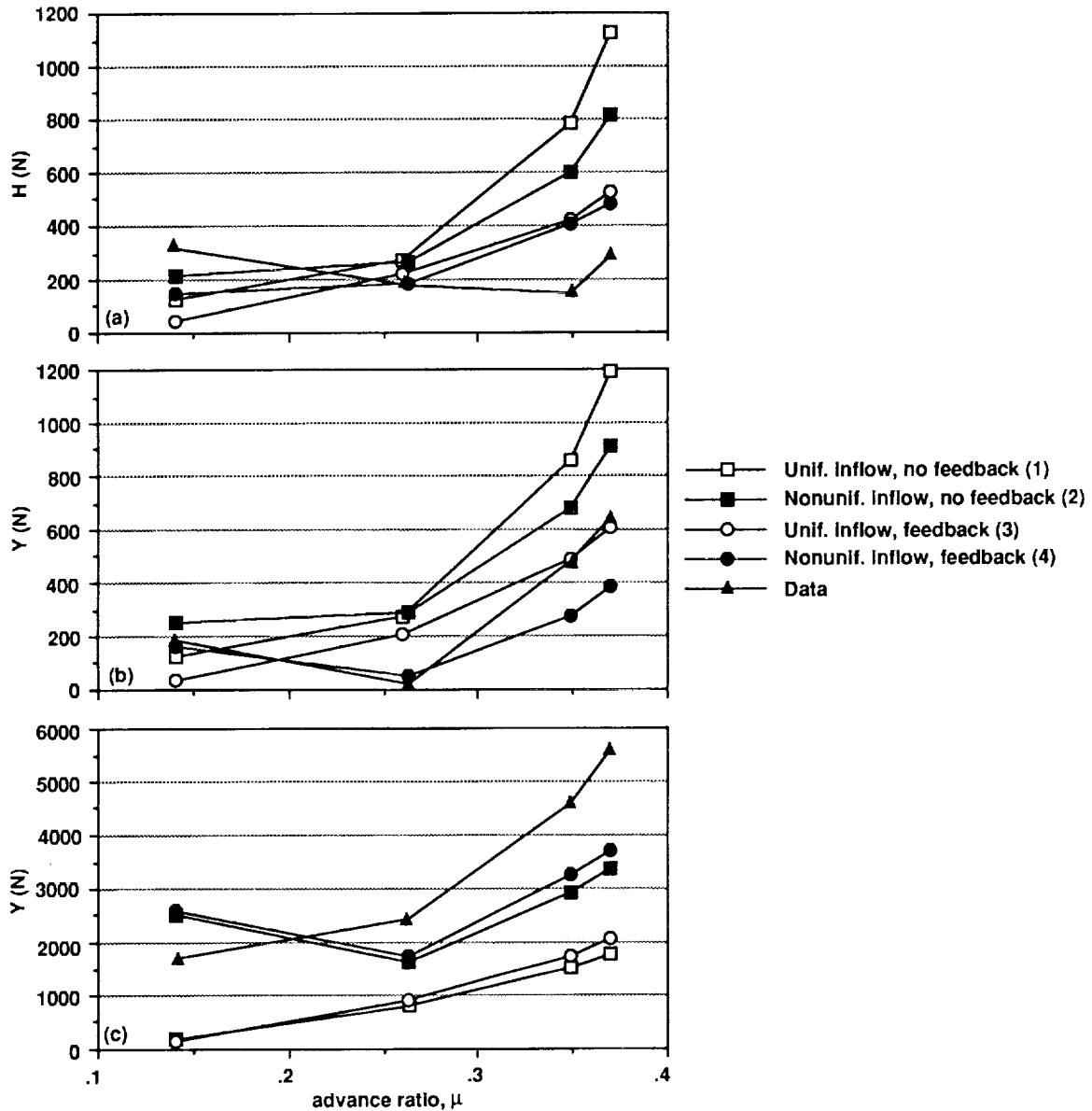


Figure 14. Correlation of measured and predicted 3/rev hub loads. Magnitudes only. Hub loads were predicted using the SAMCEF model with uniform and nonuniform inflow wake analyses, both with and without feedback, as a function of advance ratio. Numbers in () indicate model configuration (see table 6). a) H, b) Y, c) T.

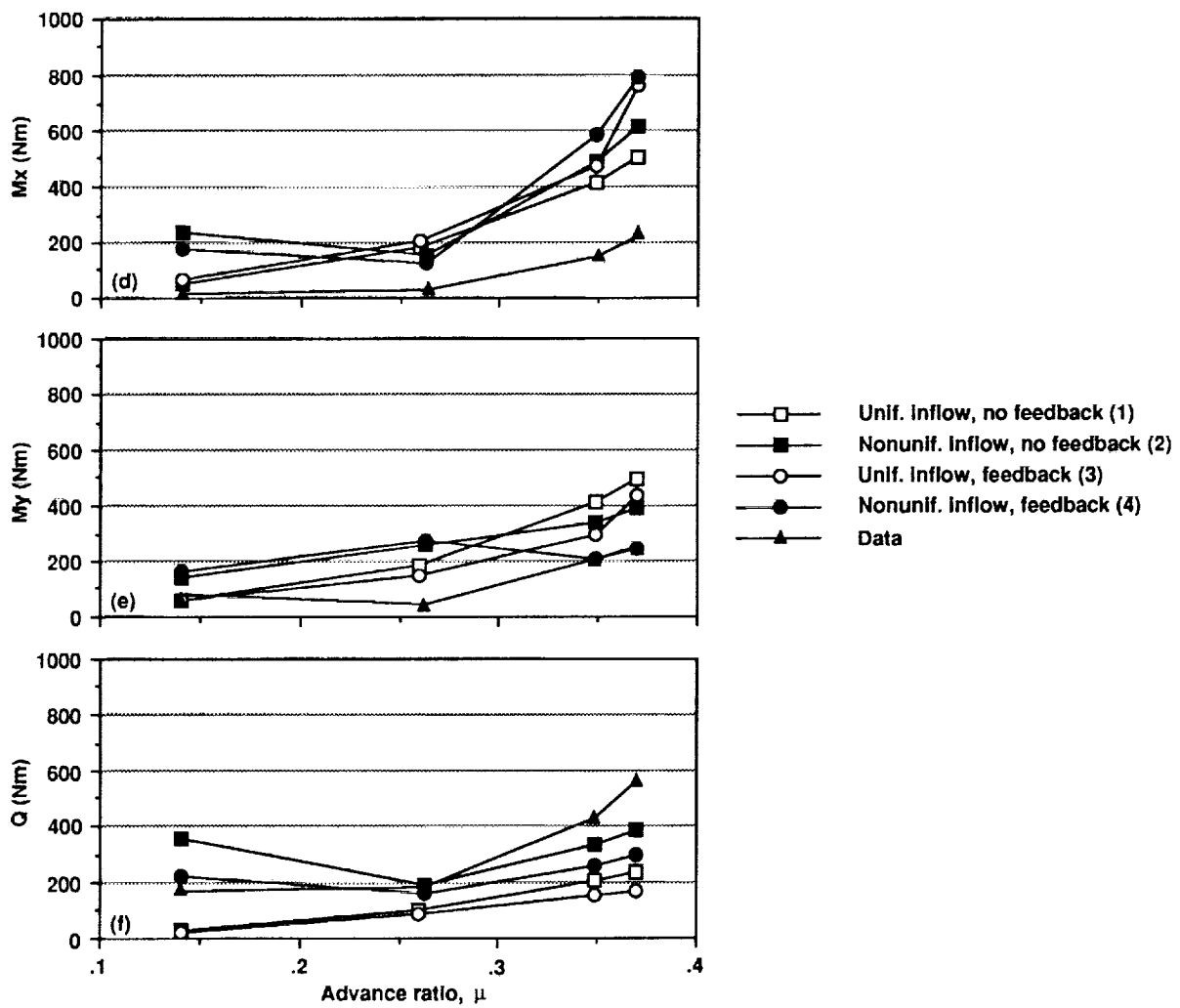


Figure 14. Concluded. d) M_x , e) M_y , f) Q .

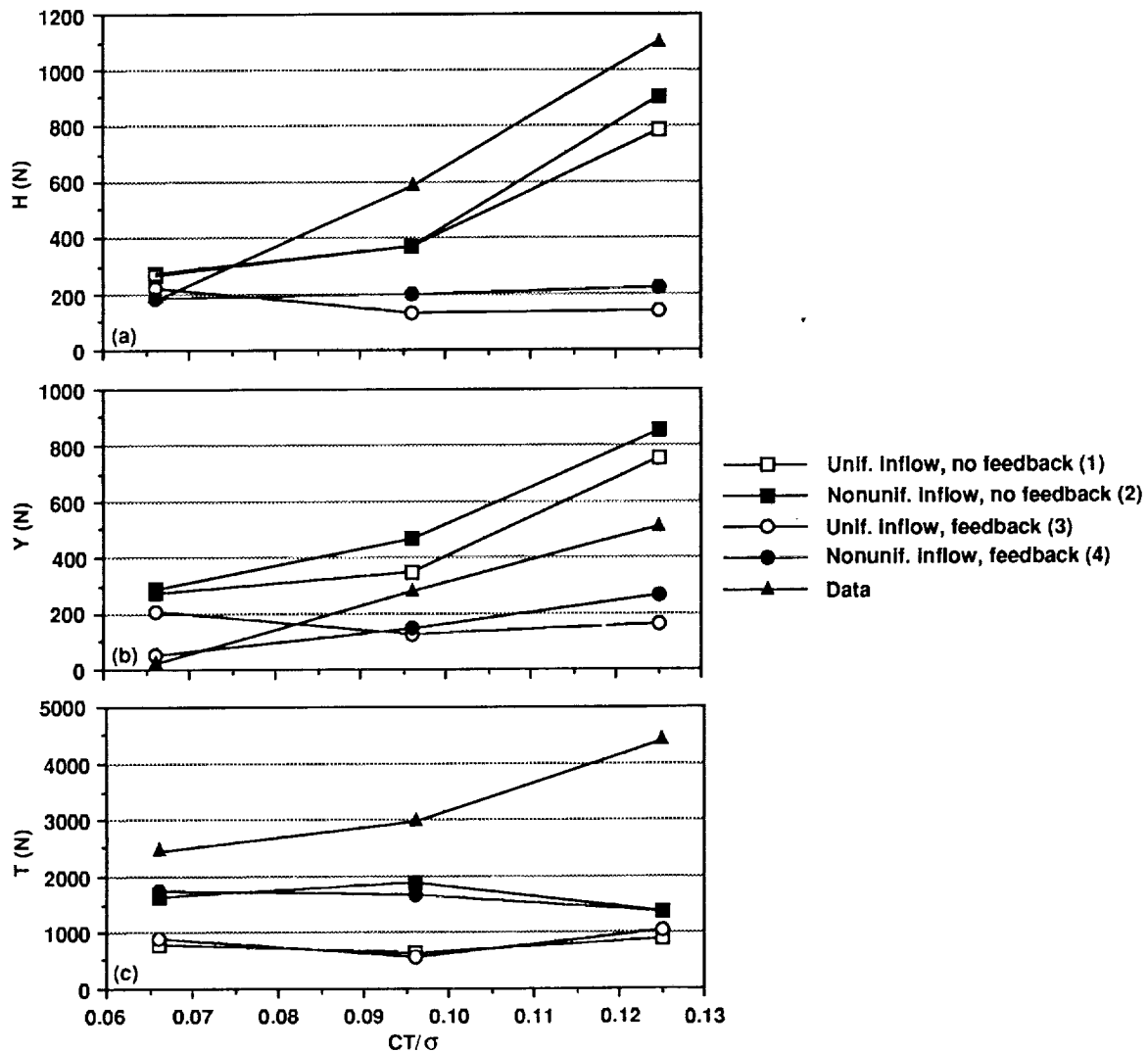


Figure 15. Correlation of measured and predicted 3/rev hub loads. Magnitudes only. Hub loads were predicted using the SAMCEF model with uniform and nonuniform inflow wake analyses, both with and without feedback, as a function of thrust-to-solidity ratio. Numbers in () indicate model configuration (see table 6). a) H, b) Y, c) T.

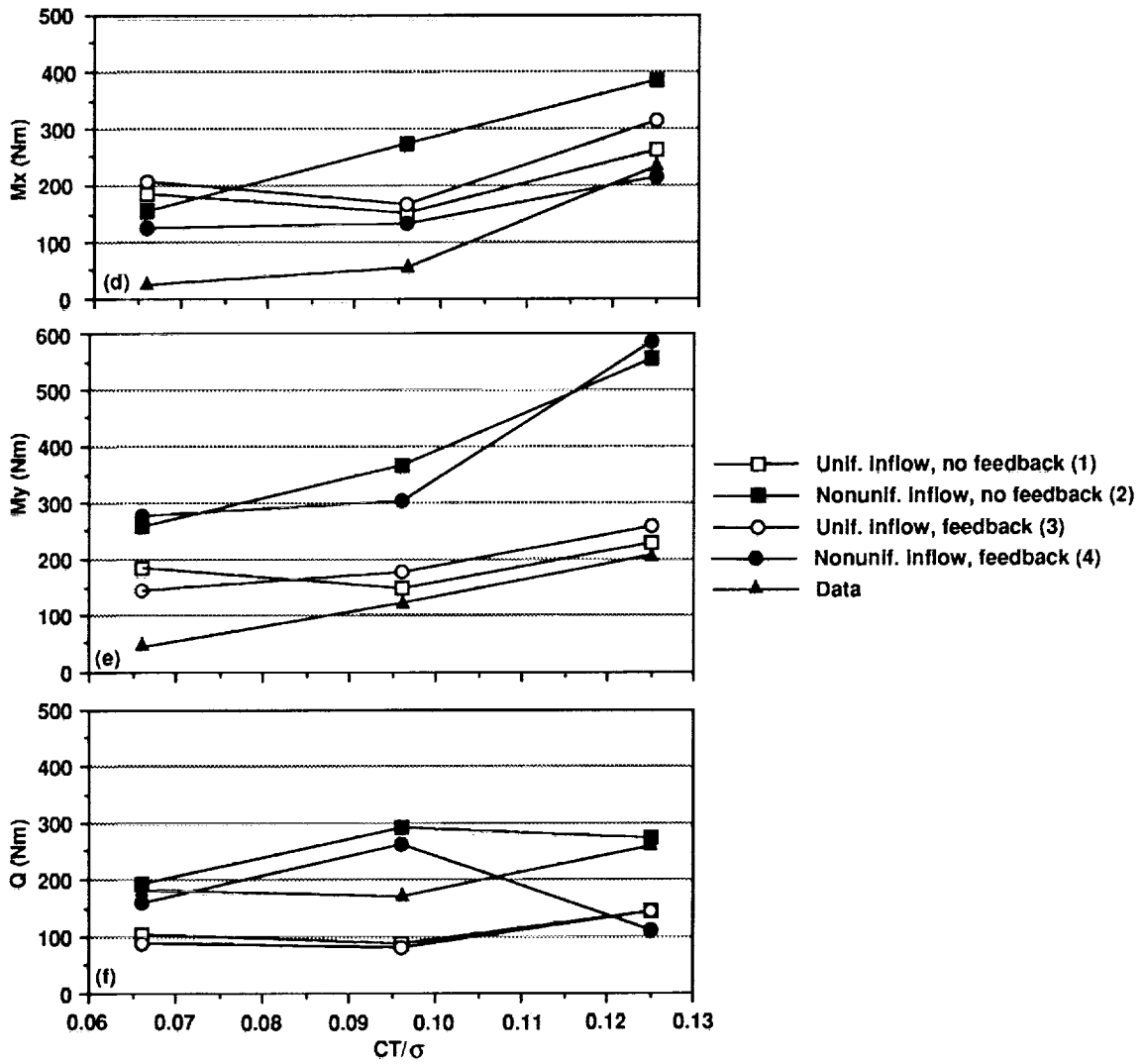


Figure 15. Concluded. d) M_x , e) M_y , f) Q .

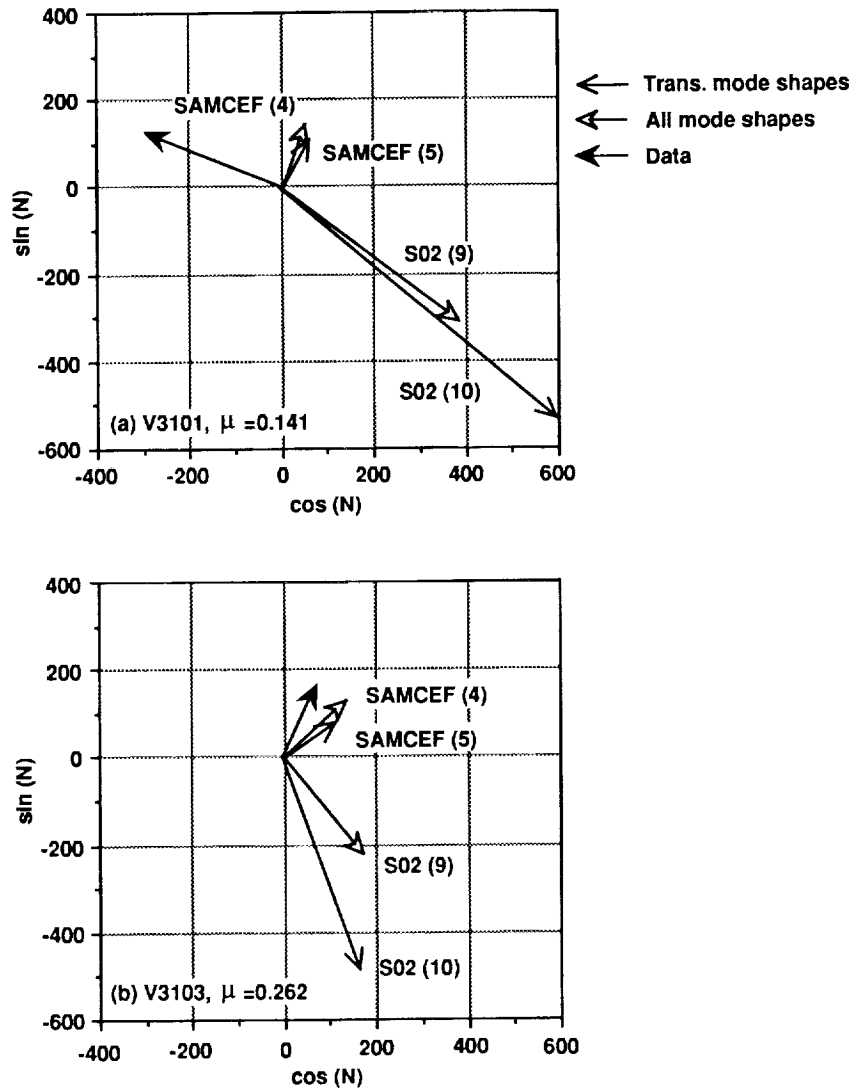


Figure 16. Magnitude and phase correlations of H, the drag force at the hub. Predictions were made using the S02 and SAMCEF models, with and without rotation mode shapes (see table 6), for the four level flight conditions. a) $\mu = 0.14$, b) $\mu = 0.26$.

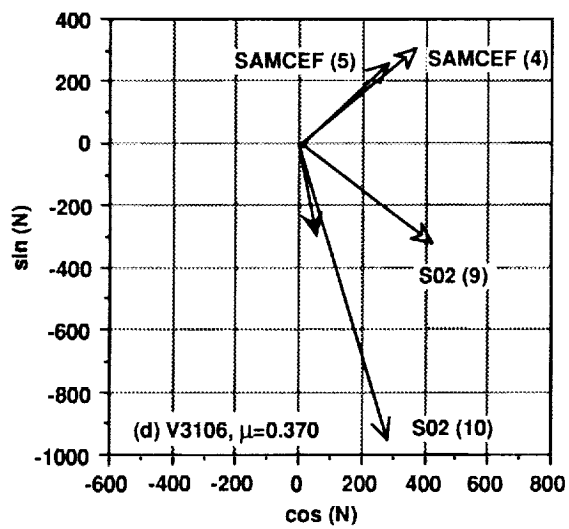
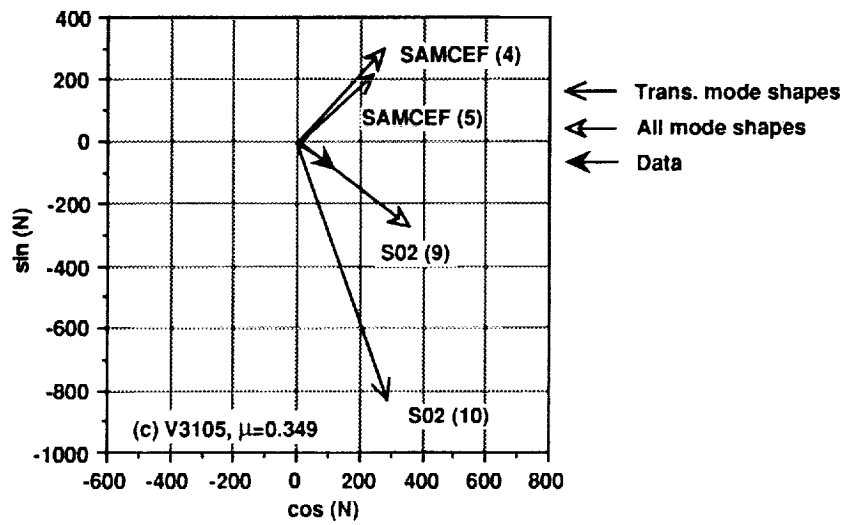


Figure 16. Concluded. c) $\mu = 0.35$, d) $\mu = 0.37$.

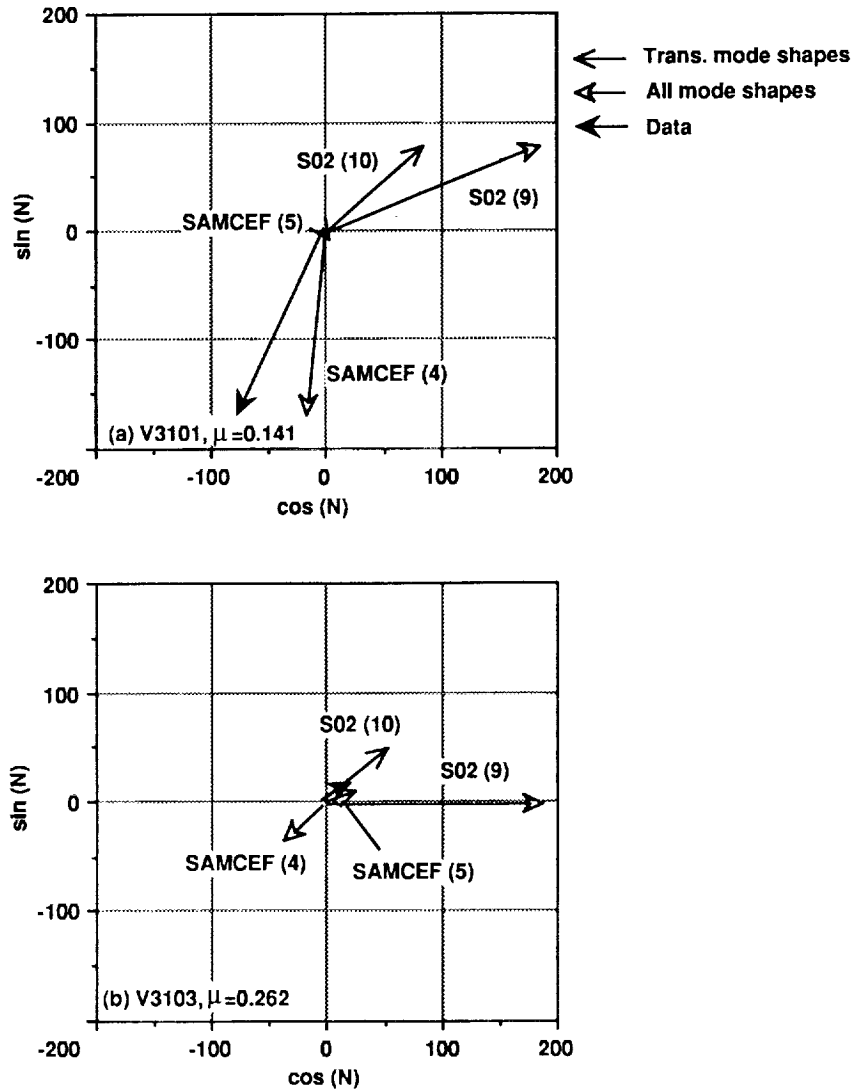


Figure 17. Magnitude and phase correlations of Y , the side force at the hub. Predictions were made using the S02 and SAMCEF models, with and without rotation mode shapes (see table 6), for the four level flight conditions. a) $\mu = 0.14$, b) $\mu = 0.26$.

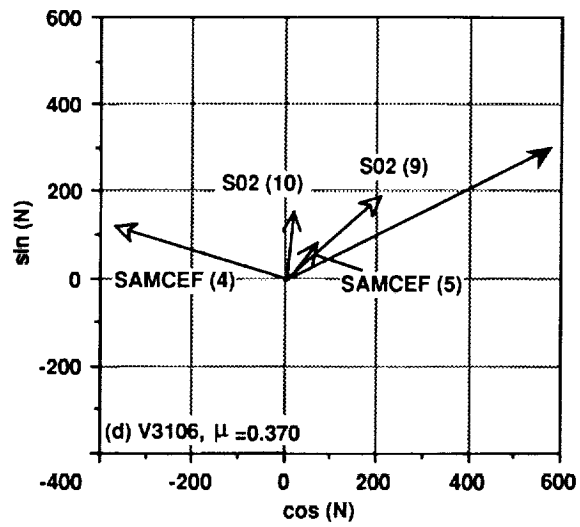
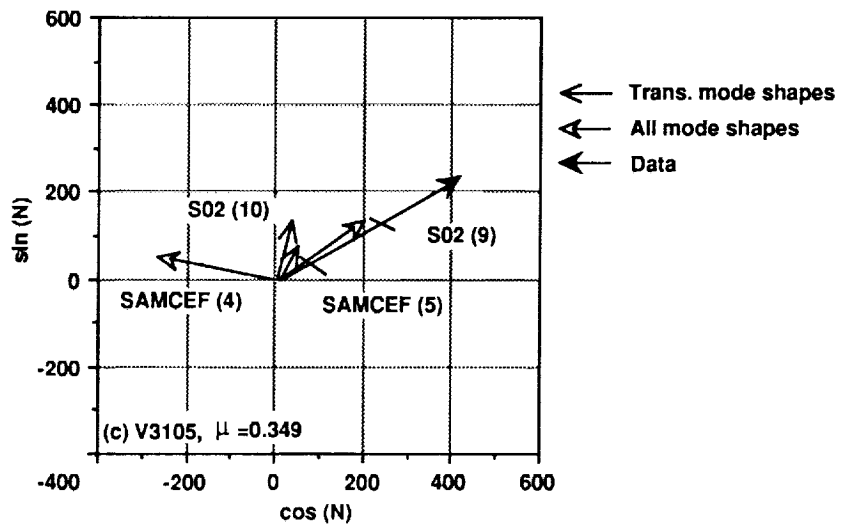


Figure 17. Concluded. c) $\mu = 0.35$, d) $\mu = 0.37$.

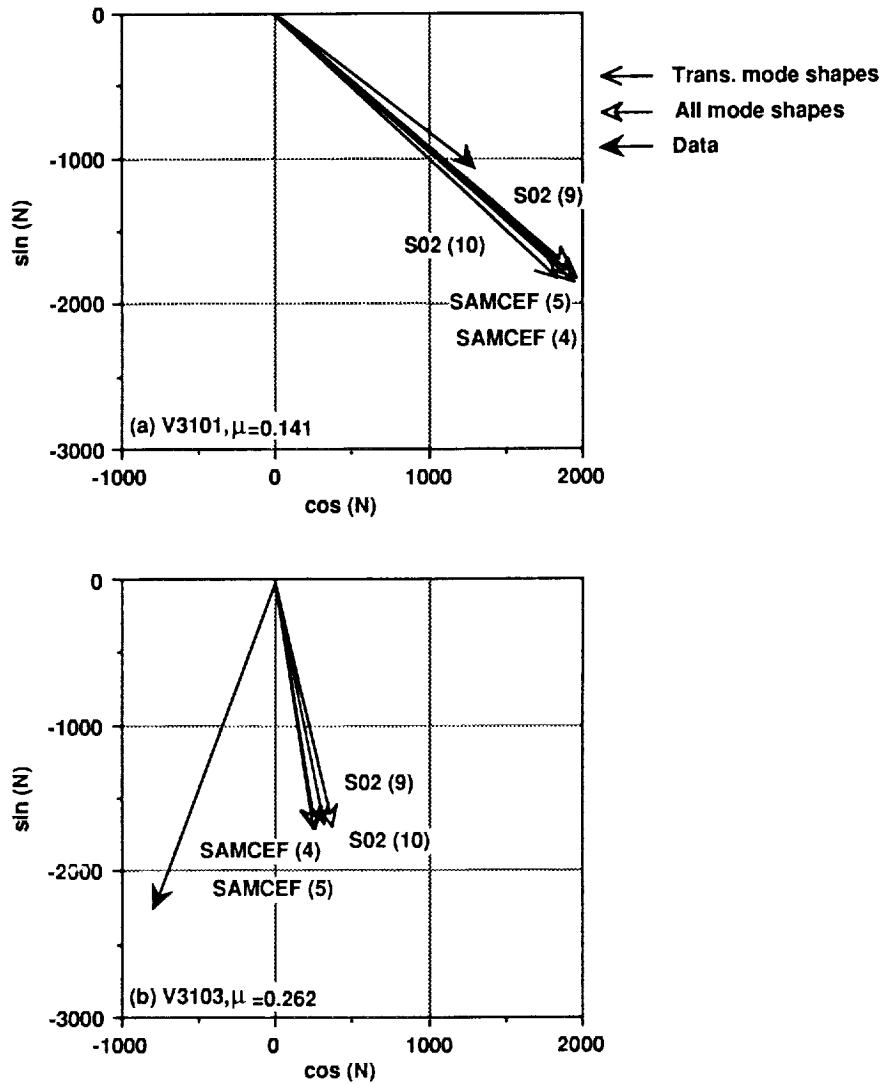


Figure 18. Magnitude and phase correlations of T, the thrust. Predictions were made using the S02 and SAMCEF models, with and without rotation mode shapes (see table 6), for the four level flight conditions. a) $\mu = 0.14$, b) $\mu = 0.26$.

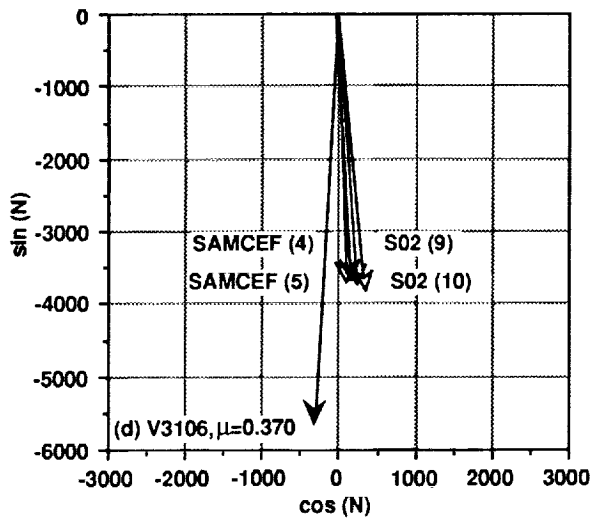
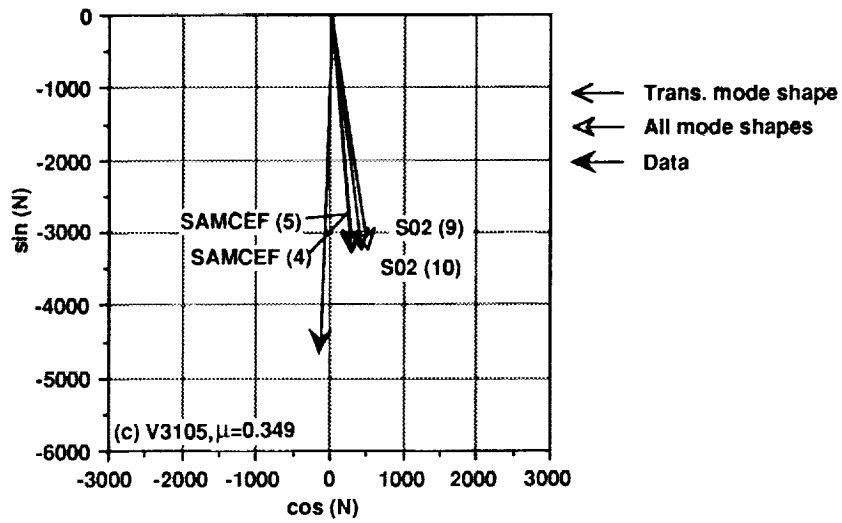


Figure 18. Concluded. c) $\mu = 0.35$, d) $\mu = 0.37$.

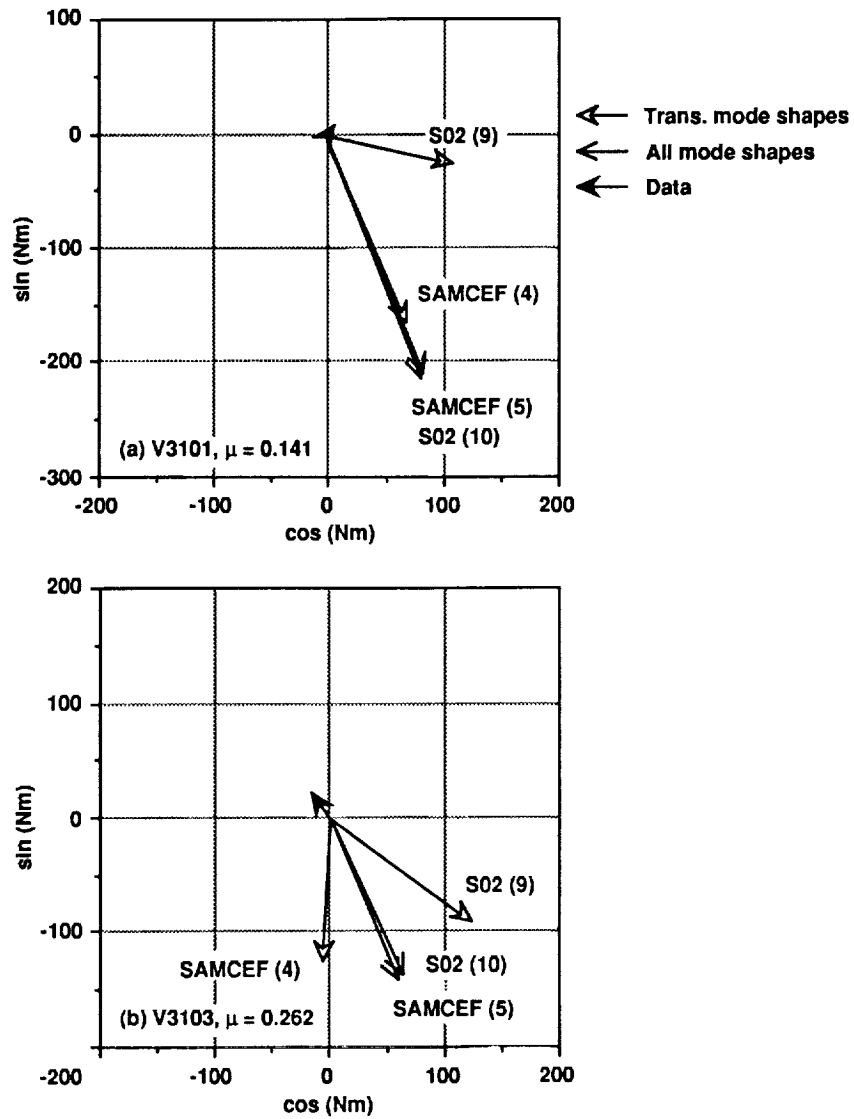


Figure 19. Magnitude and phase correlations of M_x , the rolling moment. Predictions were made using the S02 and SAMCEF models, with and without rotation mode shapes (see table 6), for the four level flight conditions. a) $\mu = 0.14$, b) $\mu = 0.26$.

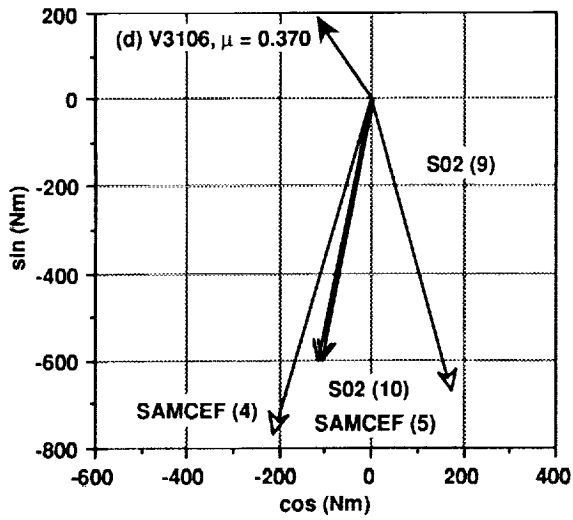
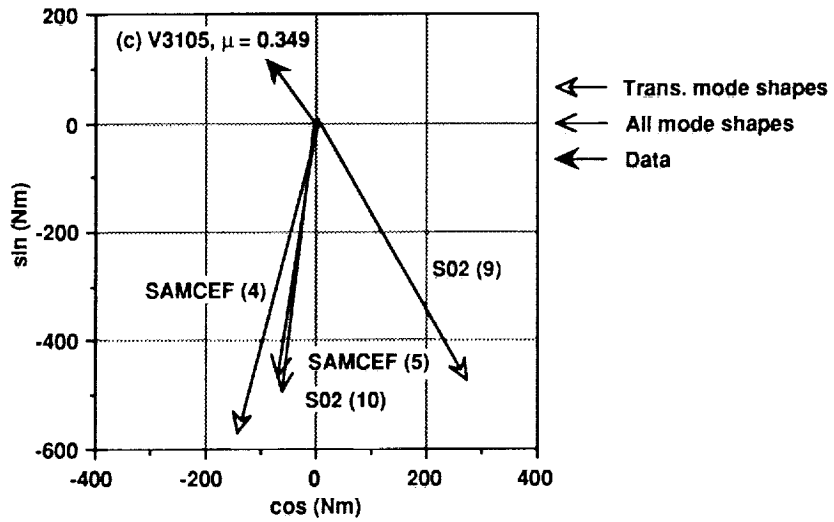


Figure 19. Concluded. c) $\mu = 0.35$, d) $\mu = 0.37$.

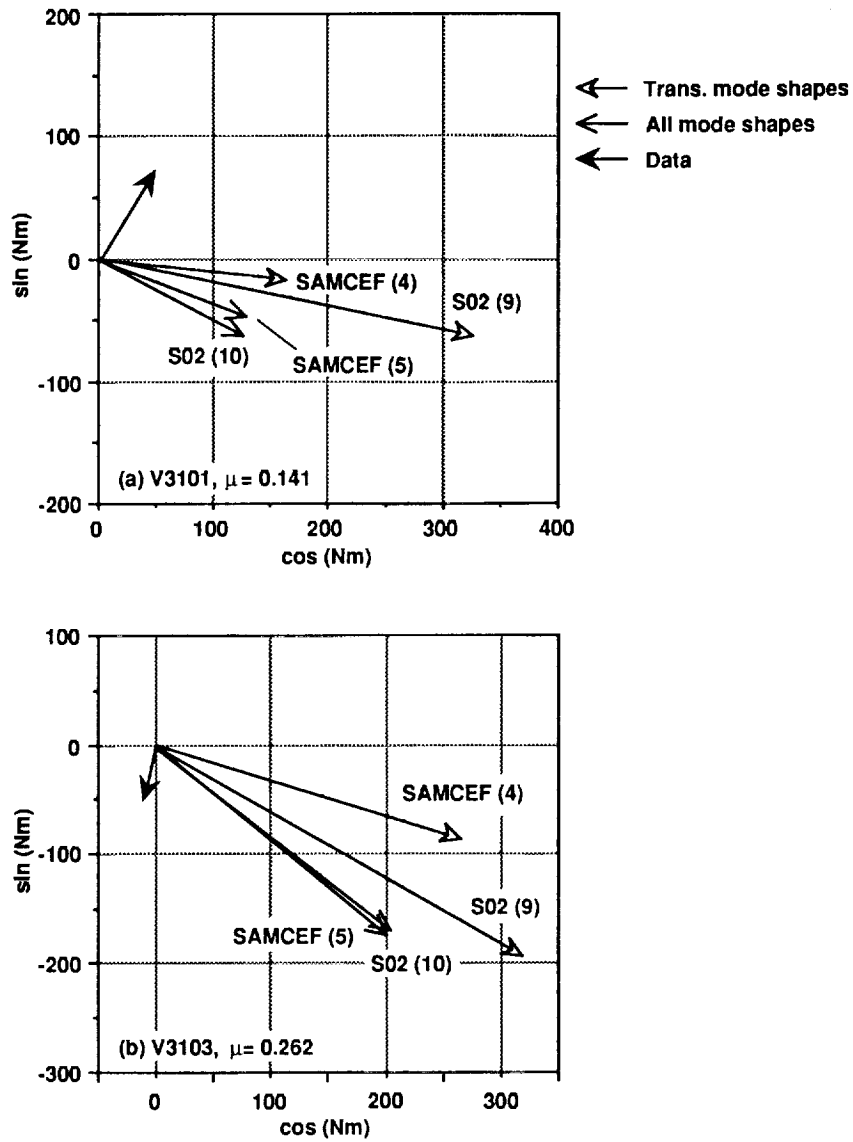


Figure 20. Magnitude and phase correlations of M_y , the pitching moment. Predictions were made using the S02 and SAMCEF models, with and without rotation mode shapes (see table 6), for the four level flight conditions. a) $\mu = 0.14$, b) $\mu = 0.26$.

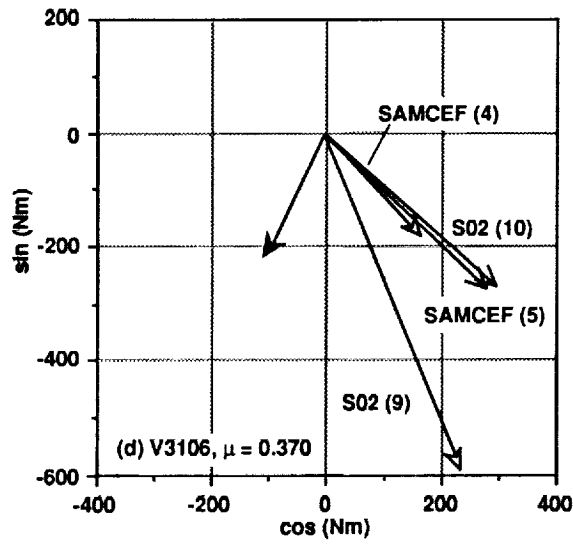
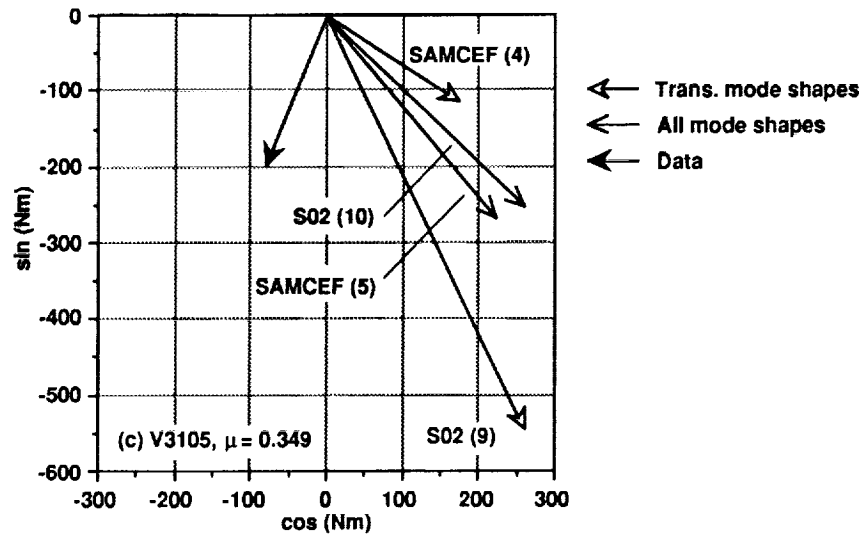


Figure 20. Concluded. c) $\mu = 0.35$, d) $\mu = 0.37$.

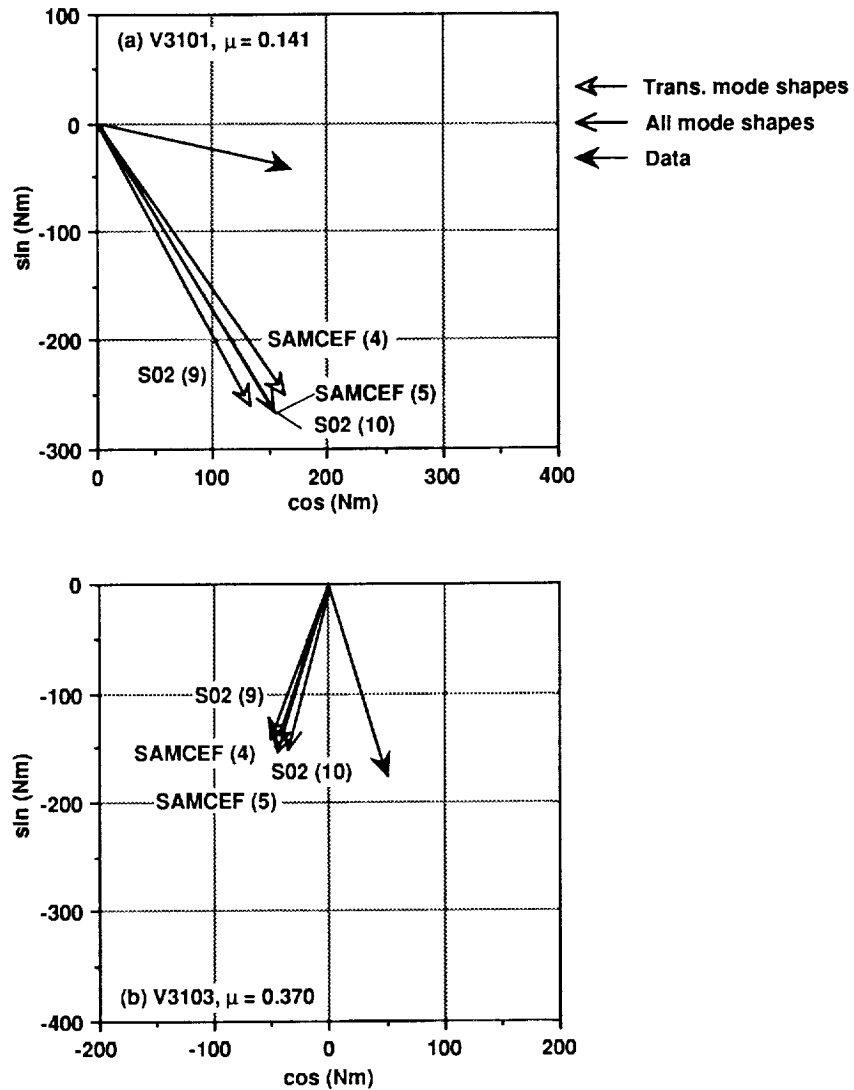


Figure 21. Magnitude and phase correlations of Q , the rotor torque. Predictions were made using the S02 and SAMCEF models, with and without rotation mode shapes (see table 6), for the four level flight conditions. a) $\mu = 0.14$, b) $\mu = 0.26$.

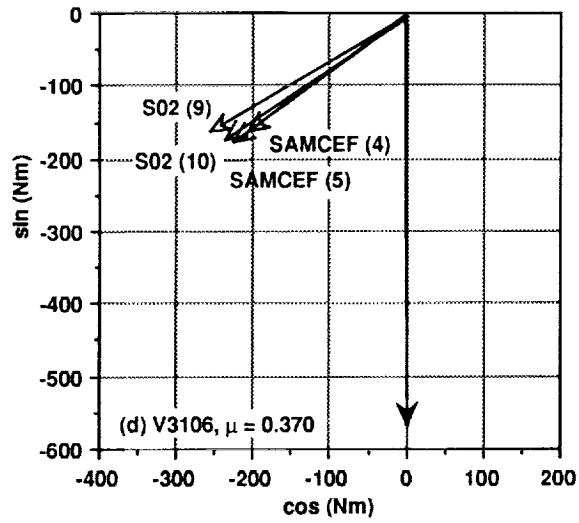
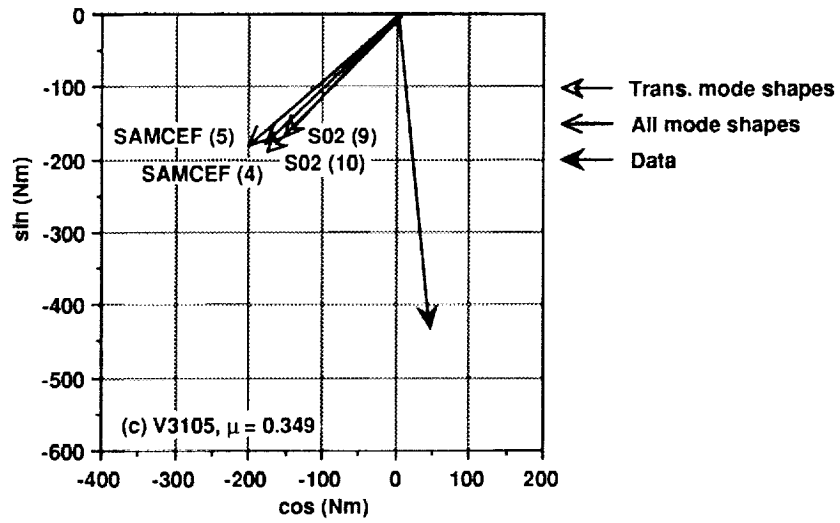


Figure 21. Concluded. c) $\mu = 0.35$, d) $\mu = 0.37$.

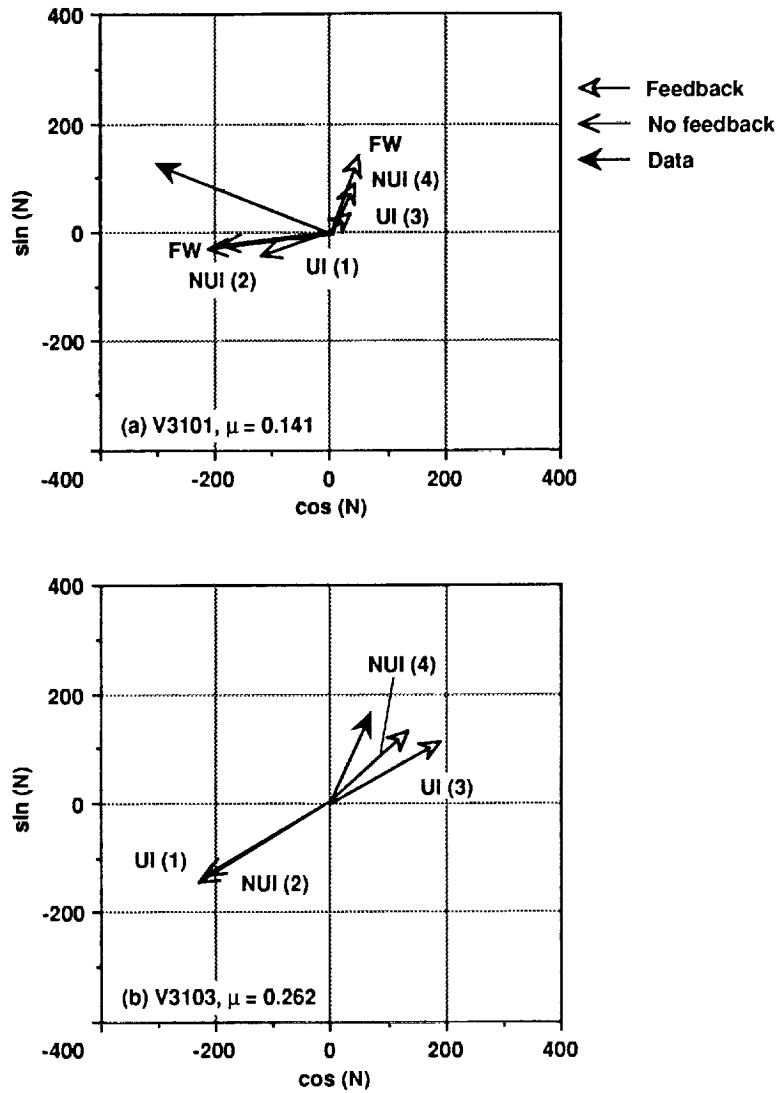


Figure 22. Magnitude and phase correlations of H , the drag at the hub. Predictions were made using the SAMCEF model with uniform (UI) and nonuniform (NUI) inflow wake analyses (a free wake analysis (FW) was used for the lowest speed condition), both with and without feedback, for the four level flight conditions (see table 6). a) $\mu = 0.14$, b) $\mu = 0.26$.

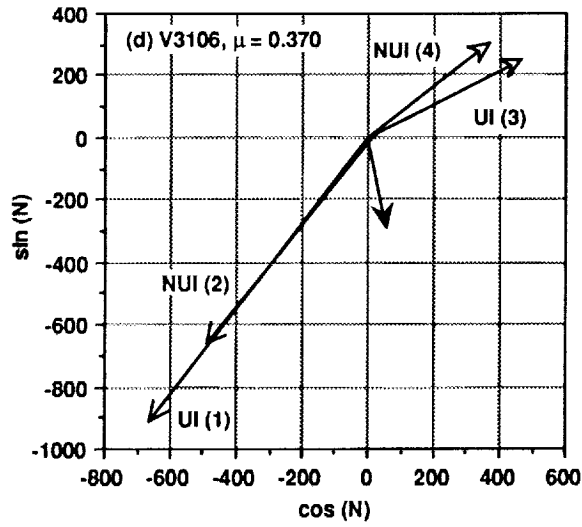
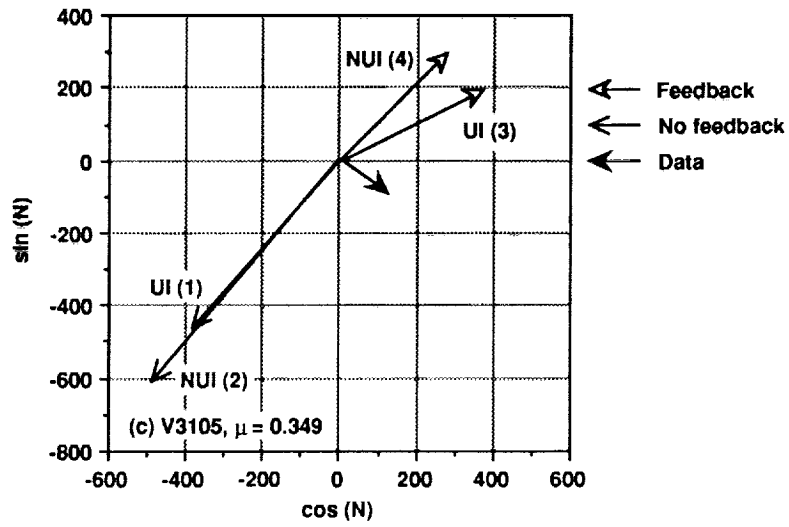


Figure 22. Concluded. c) $\mu = 0.35$, d) $\mu = 0.37$.

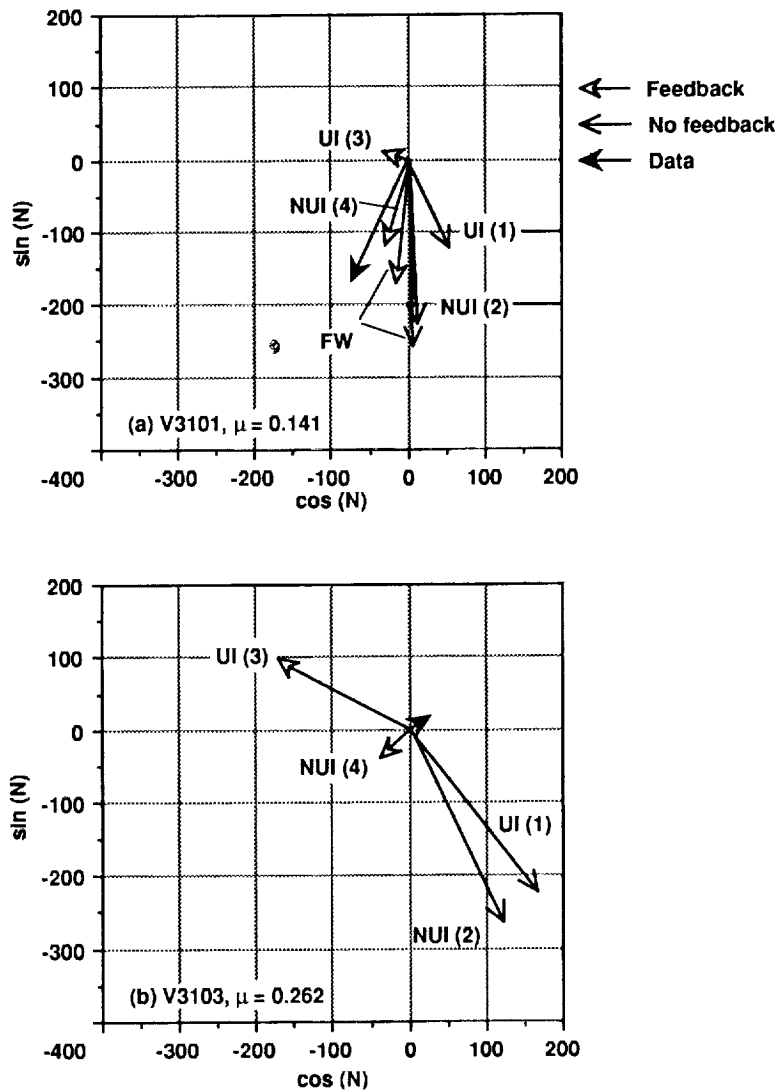


Figure 23. Magnitude and phase correlations of Y , the side force at the hub. Predictions were made using the SAMCEF model with uniform (UI) and nonuniform (NUI) inflow wake analyses (a free wake analysis (FW) was used for the lowest speed condition), both with and without feedback, for the four level flight conditions(see table 6). a) $\mu = 0.14$, b) $\mu = 0.26$.

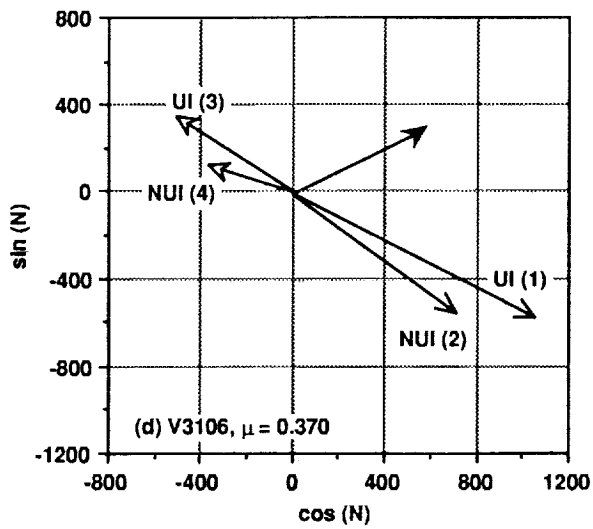
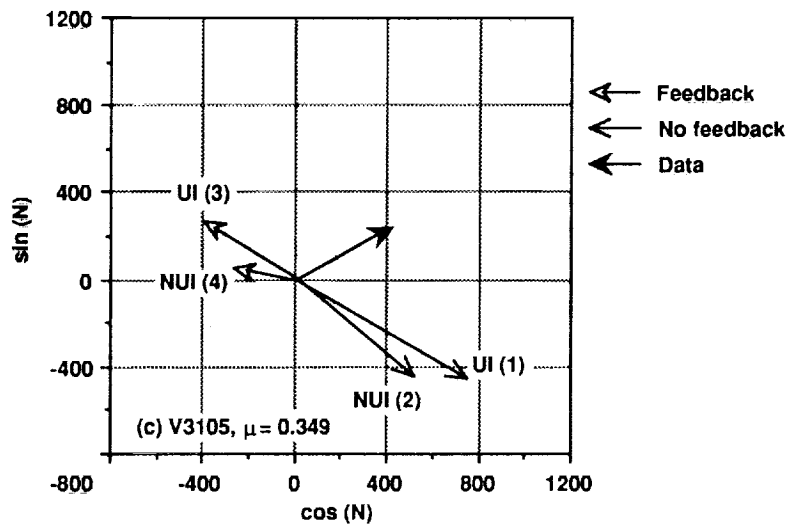


Figure 23. Concluded. c) $\mu = 0.35$, d) $\mu = 0.37$.

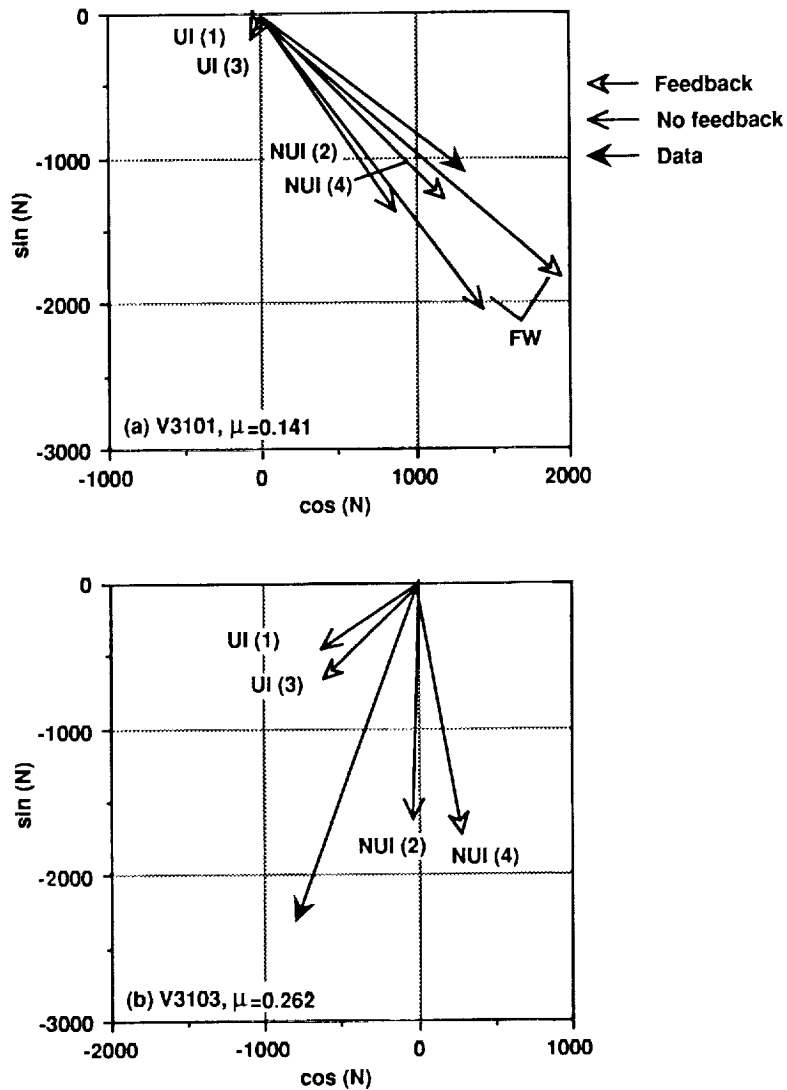


Figure 24. Magnitude and phase correlations of T , the thrust. Predictions were made using the SAMCEF model with uniform (UI) and nonuniform (NUI) inflow wake analyses (a free wake analysis (FW) was used for the lowest speed condition), both with and without feedback, for the four level flight conditions (see table 6). a) $\mu = 0.14$, b) $\mu = 0.26$.

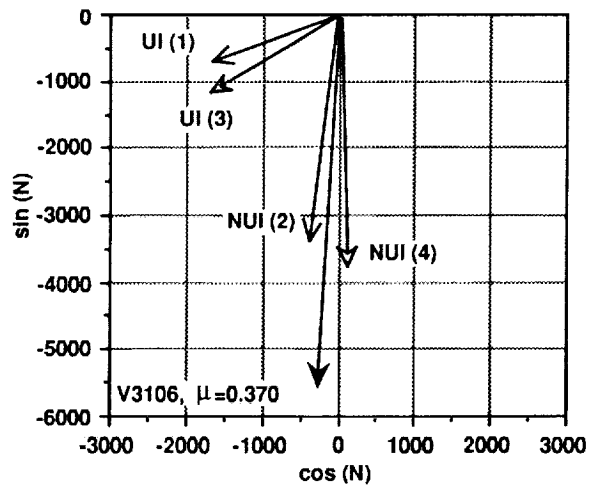
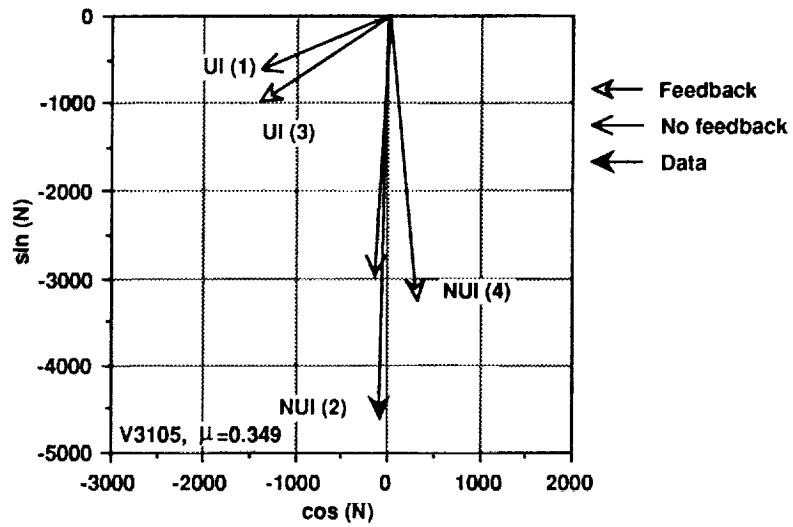


Figure 24. Concluded. c) $\mu = 0.35$, d) $\mu = 0.37$.

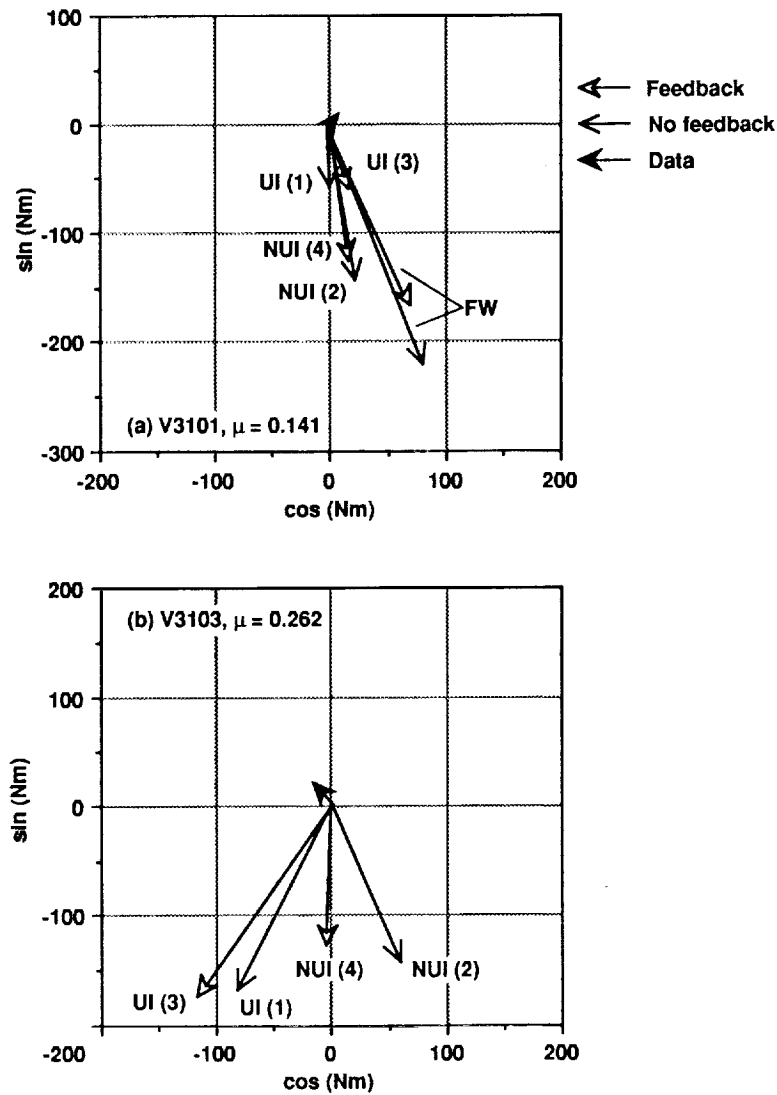


Figure 25. Magnitude and phase correlations of M_x , the rolling moment. Predictions were made using the SAMCEF model with uniform (UI) and nonuniform (NUI) inflow wake analyses (a free wake analysis (FW) was used for the lowest speed condition), both with and without feedback, for the four level flight conditions (see table 6). a) $\mu = 0.14$, b) $\mu = 0.26$.

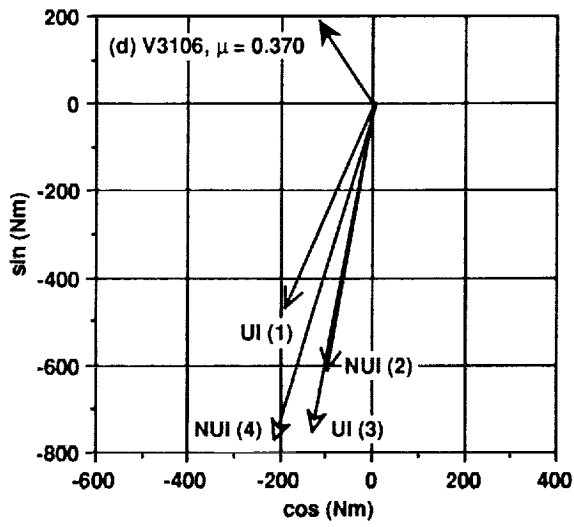
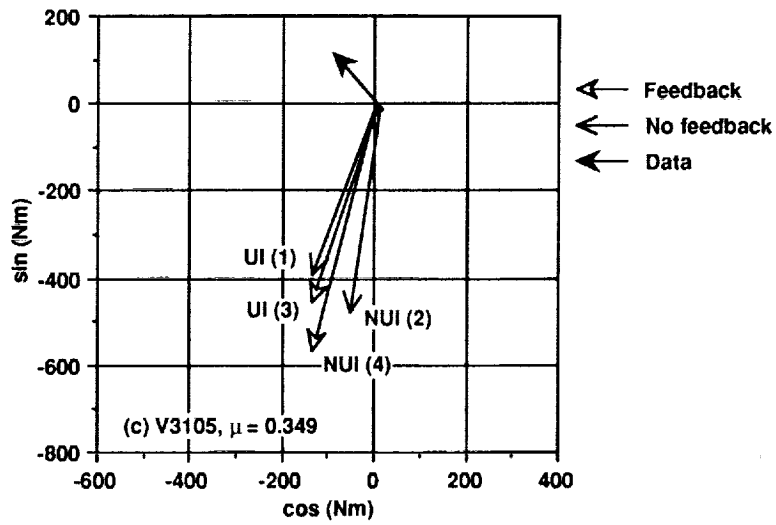


Figure 25. Concluded. c) $\mu = 0.35$, d) $\mu = 0.37$.

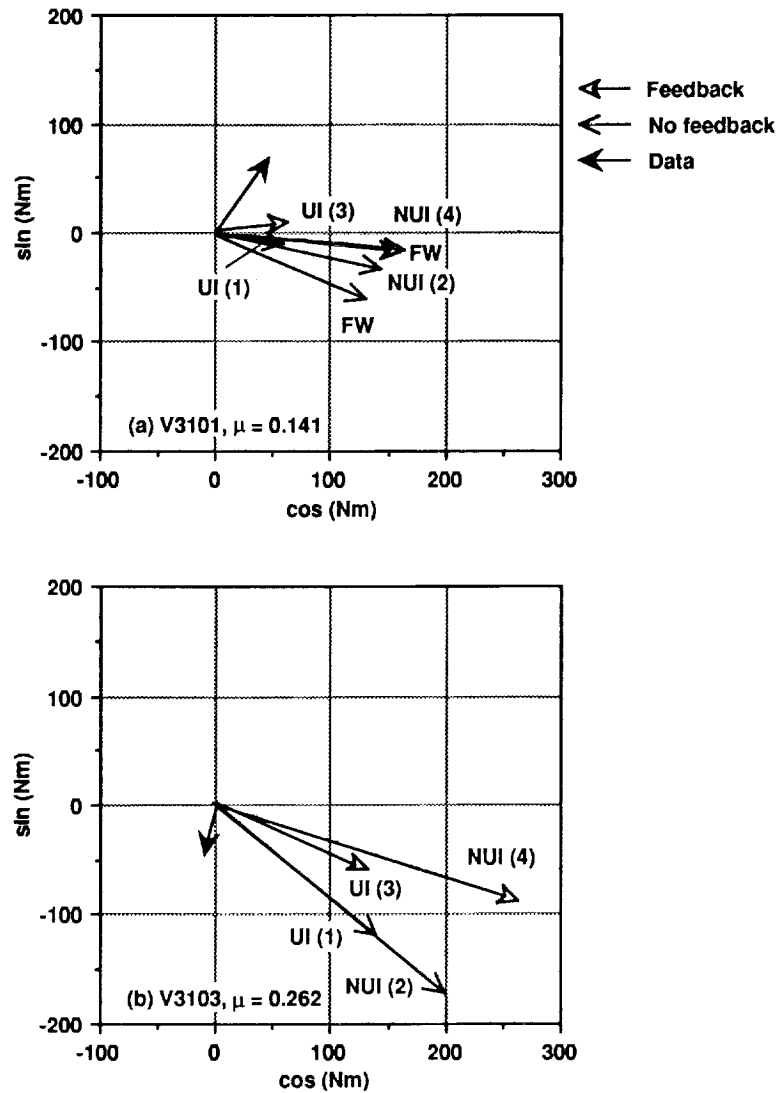


Figure 26. Magnitude and phase correlations of M_y , the pitching moment. Predictions were made using the SAMCEF model with uniform (UI) and nonuniform (NUI) inflow wake analyses (a free wake analysis (FW) was used for the lowest speed condition), both with and without feedback, for the four level flight conditions (see table 6). a) $\mu = 0.14$, b) $\mu = 0.26$.

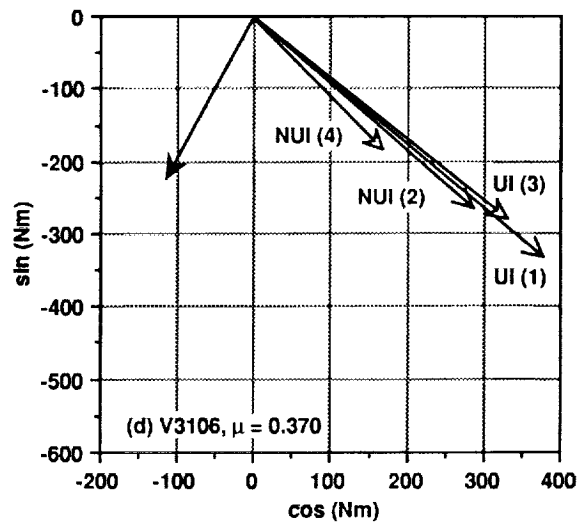
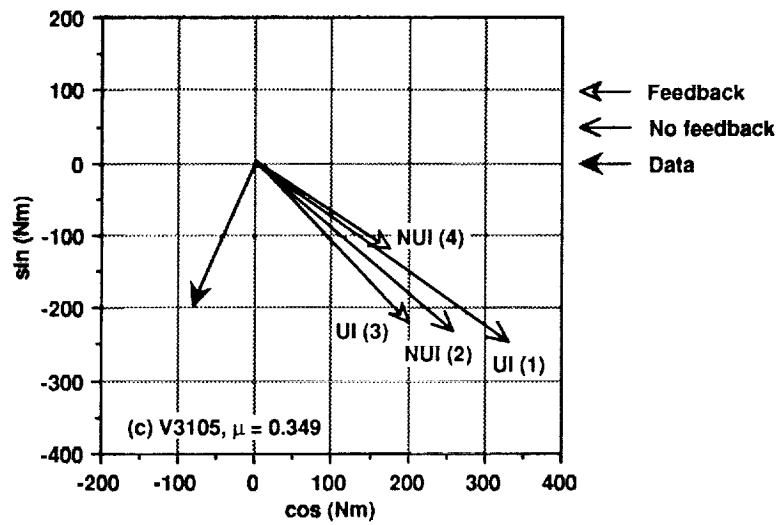


Figure 26. Concluded. c) $\mu = 0.35$, d) $\mu = 0.37$.

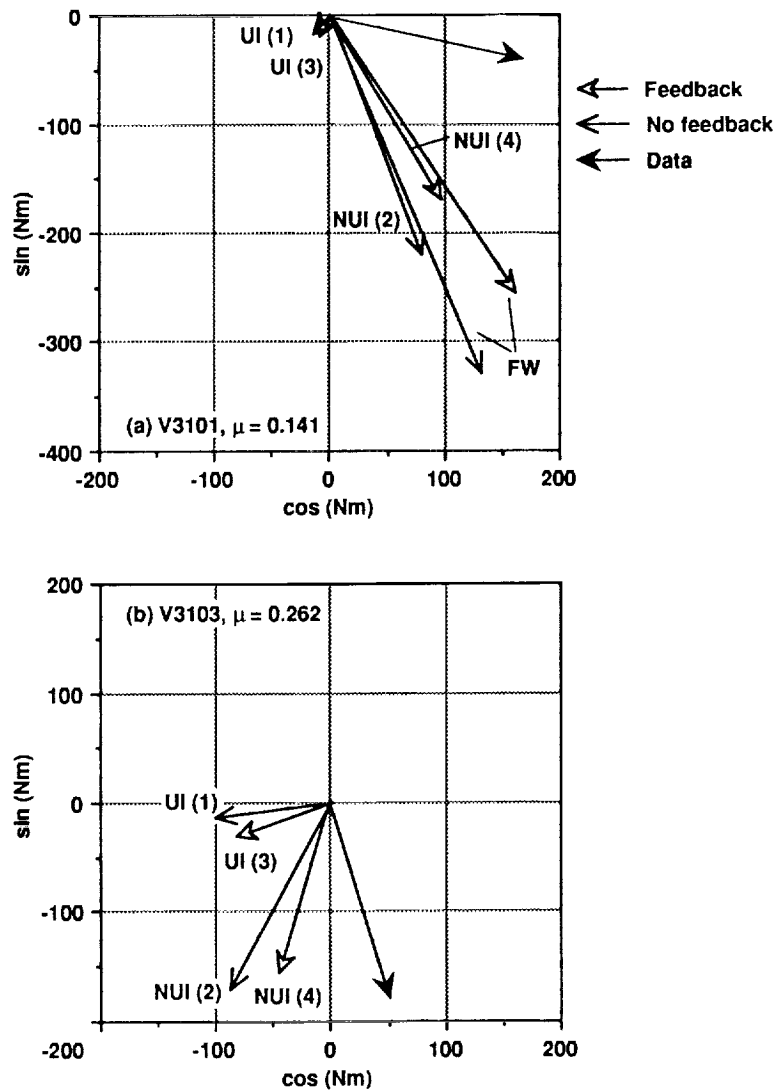


Figure 27. Magnitude and phase correlations of Q , the rotor torque. Predictions were made using the SAMCEF model with uniform (UI) and nonuniform (NUI) inflow wake analyses (a free wake analysis (FW) was used for the lowest speed condition), both with and without feedback, for the four level flight conditions (see table 6). a) $\mu = 0.14$, b) $\mu = 0.26$.

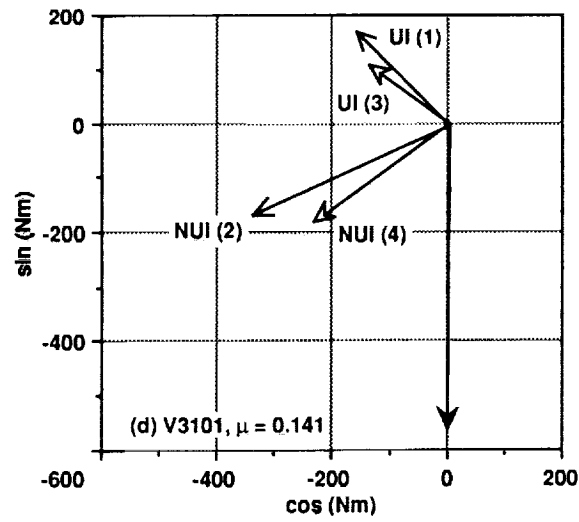
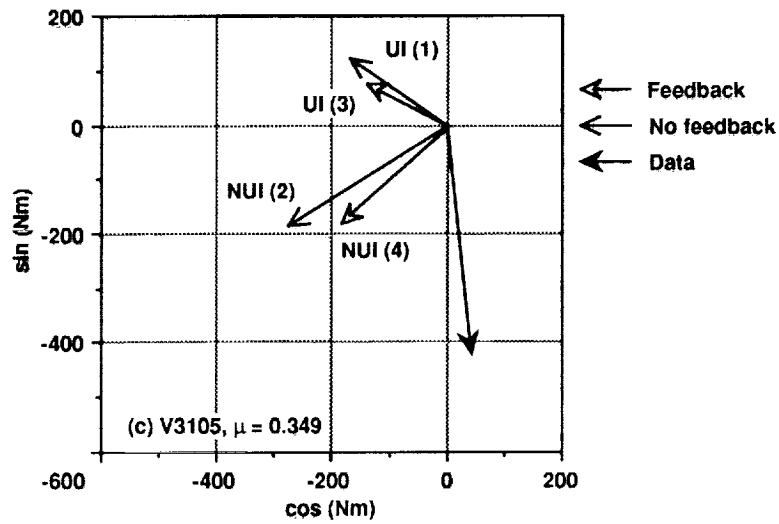


Figure 27. Concluded. c) $\mu = 0.35$, d) $\mu = 0.37$.

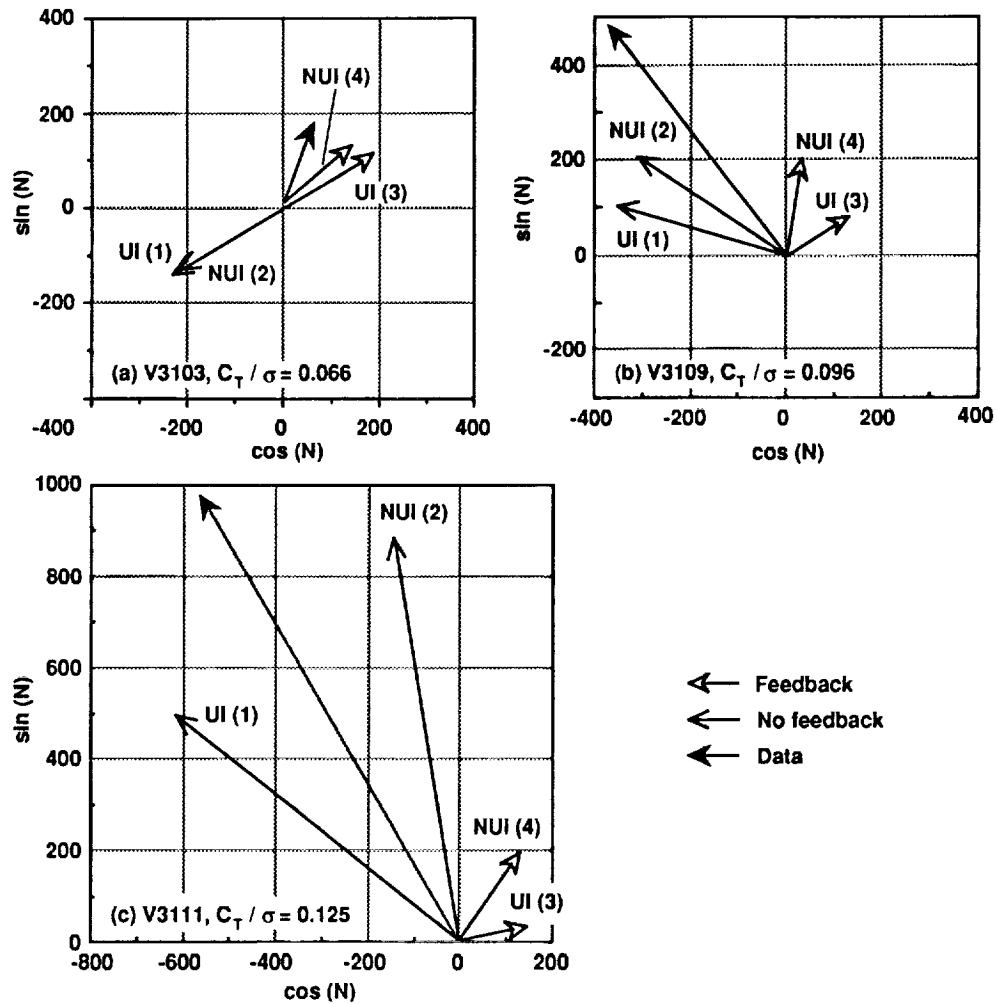


Figure 28. Magnitude and phase correlations of H , the drag at the hub. Predictions were made using the SAMCEF model with uniform (UI) and nonuniform (NUI) inflow wake analyses (a free wake analysis (FW) was used for the lowest speed condition), both with and without feedback (see table 6), for the three constant speed conditions. a) $C_T/\sigma = 0.066$, b) $C_T/\sigma = 0.096$, c) $C_T/\sigma = 0.125$.

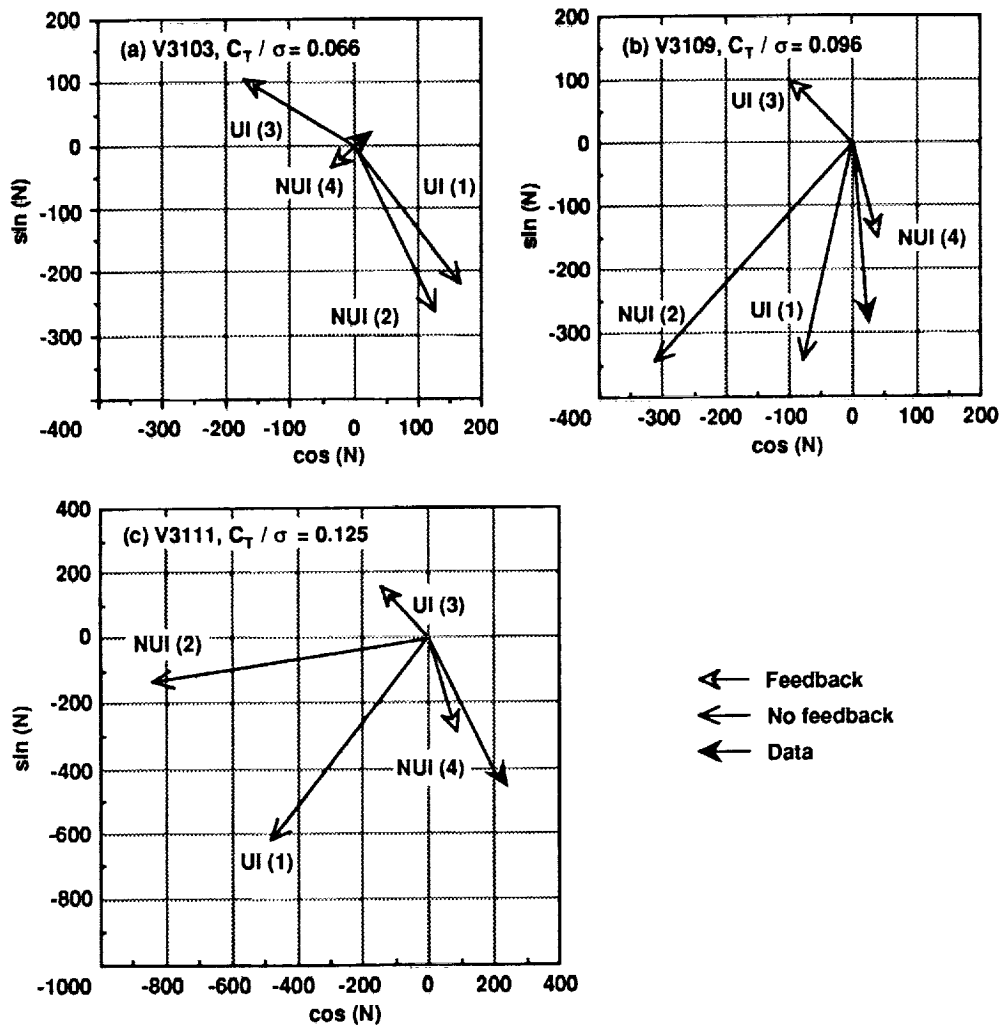


Figure 29. Magnitude and phase correlations of Y , the side force at the hub. Predictions were made using the SAMCEF model with uniform (UI) and nonuniform (NUI) inflow wake analyses (a free wake analysis (FW) was used for the lowest speed condition), both with and without feedback (see table 6), for the three constant speed conditions. a) $C_T/\sigma = 0.066$, b) $C_T/\sigma = 0.096$, c) $C_T/\sigma = 0.125$.

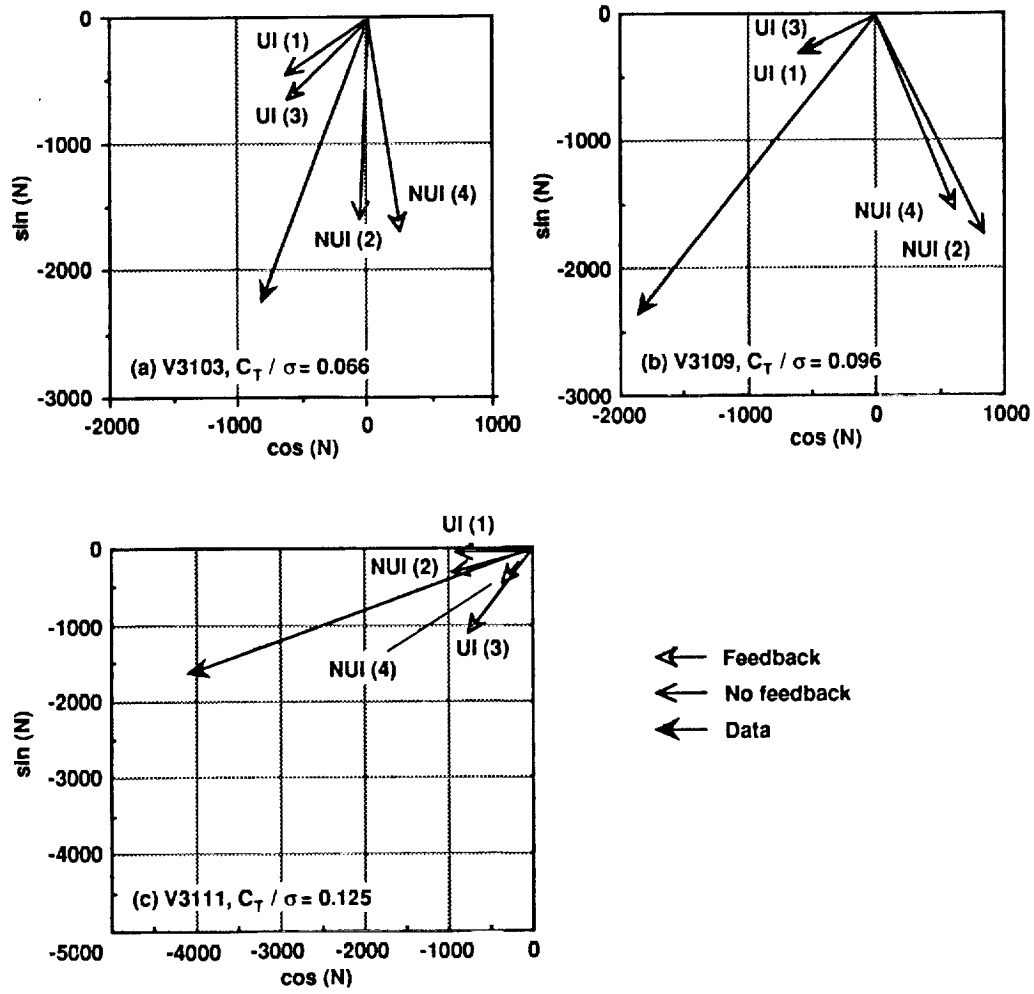


Figure 30. Magnitude and phase correlations of T , the thrust. Predictions were made using the SAMCEF model with uniform (UI) and nonuniform (NUI) inflow wake analyses (a free wake analysis (FW) was used for the lowest speed condition), both with and without feedback (see table 6), for the three constant speed conditions. a) $C_T/\sigma = 0.066$, b) $C_T/\sigma = 0.096$, c) $C_T/\sigma = 0.125$.

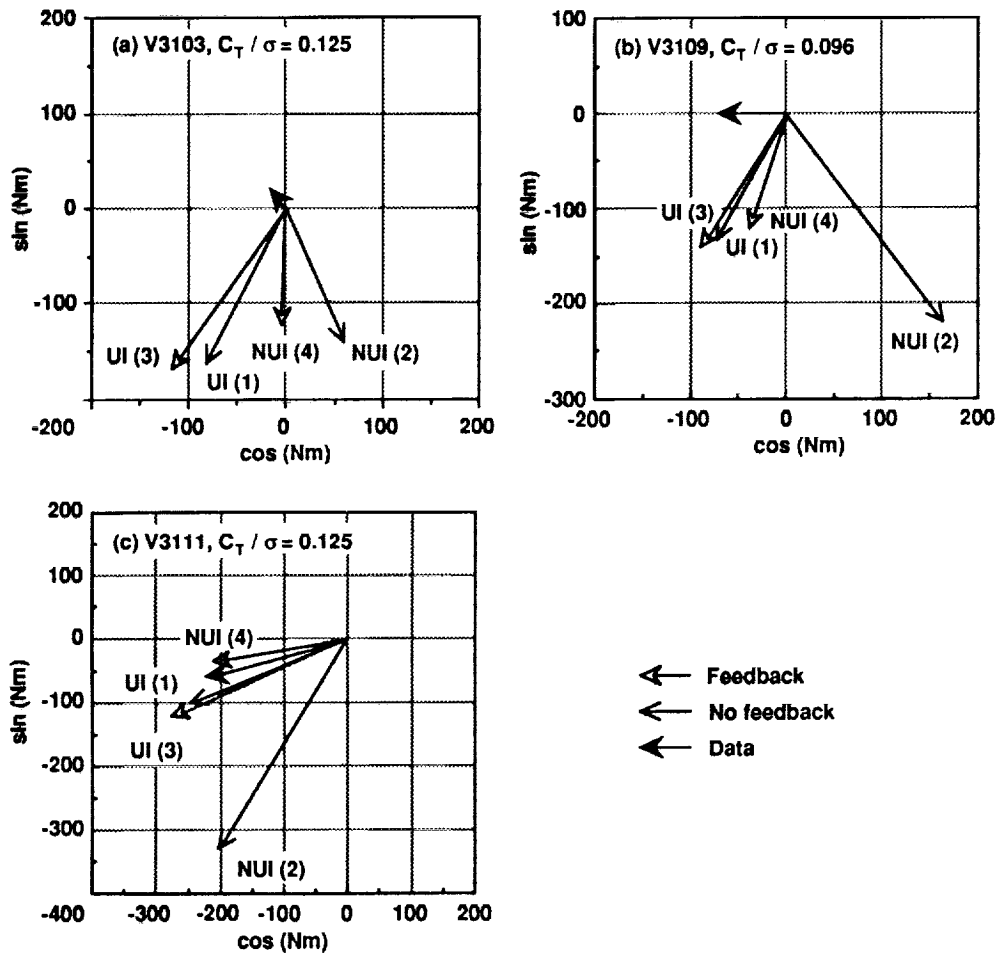


Figure 31. Magnitude and phase correlations of M_x , the rolling moment. Predictions were made using the SAMCEF model with uniform (UI) and nonuniform (NUI) inflow wake analyses (a free wake analysis (FW) was used for the lowest speed condition), both with and without feedback (see table 6), for the three constant speed conditions. a) $C_T/\sigma = 0.066$, b) $C_T/\sigma = 0.096$, c) $C_T/\sigma = 0.125$.

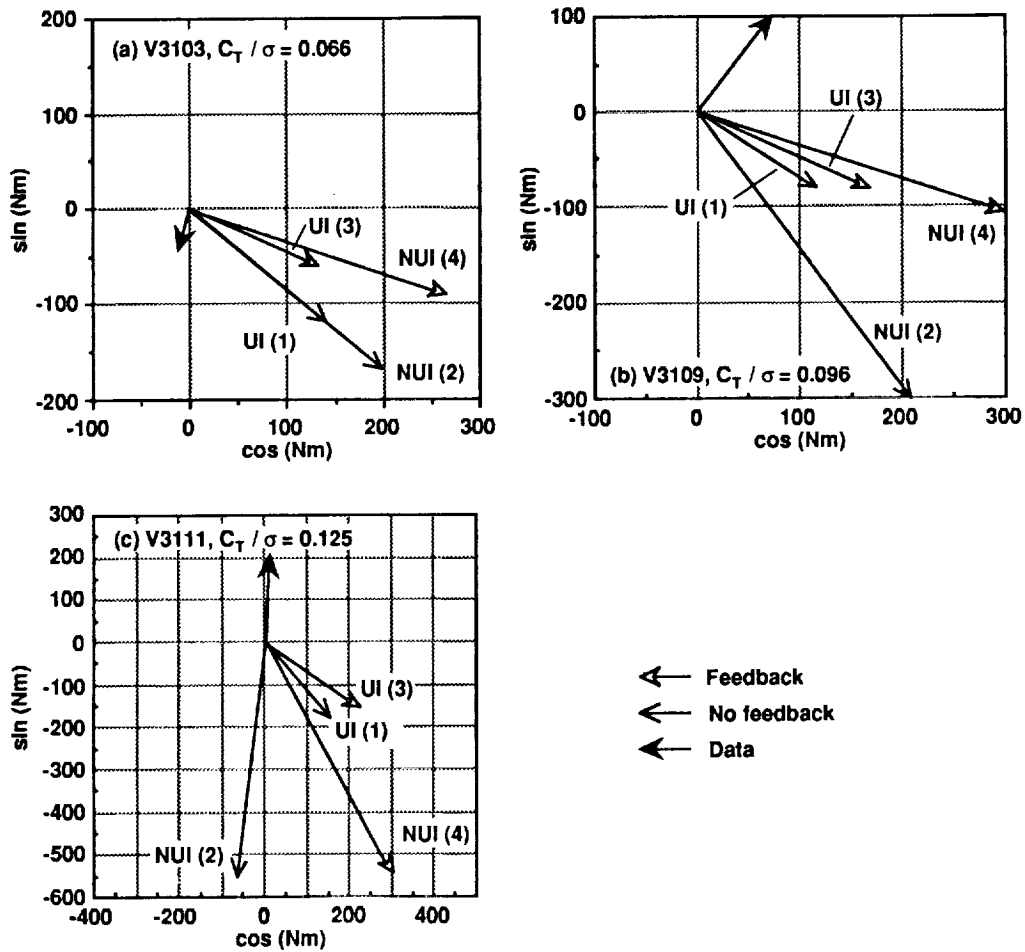


Figure 32. Magnitude and phase correlations of M_y , the pitching moment. Predictions were made using the SAMCEF model with uniform (UI) and nonuniform (NUI) inflow wake analyses (a free wake analysis (FW) was used for the lowest speed condition), both with and without feedback (see table 6), for the three constant speed conditions. a) $C_T/\sigma = 0.066$, b) $C_T/\sigma = 0.096$, c) $C_T/\sigma = 0.125$.

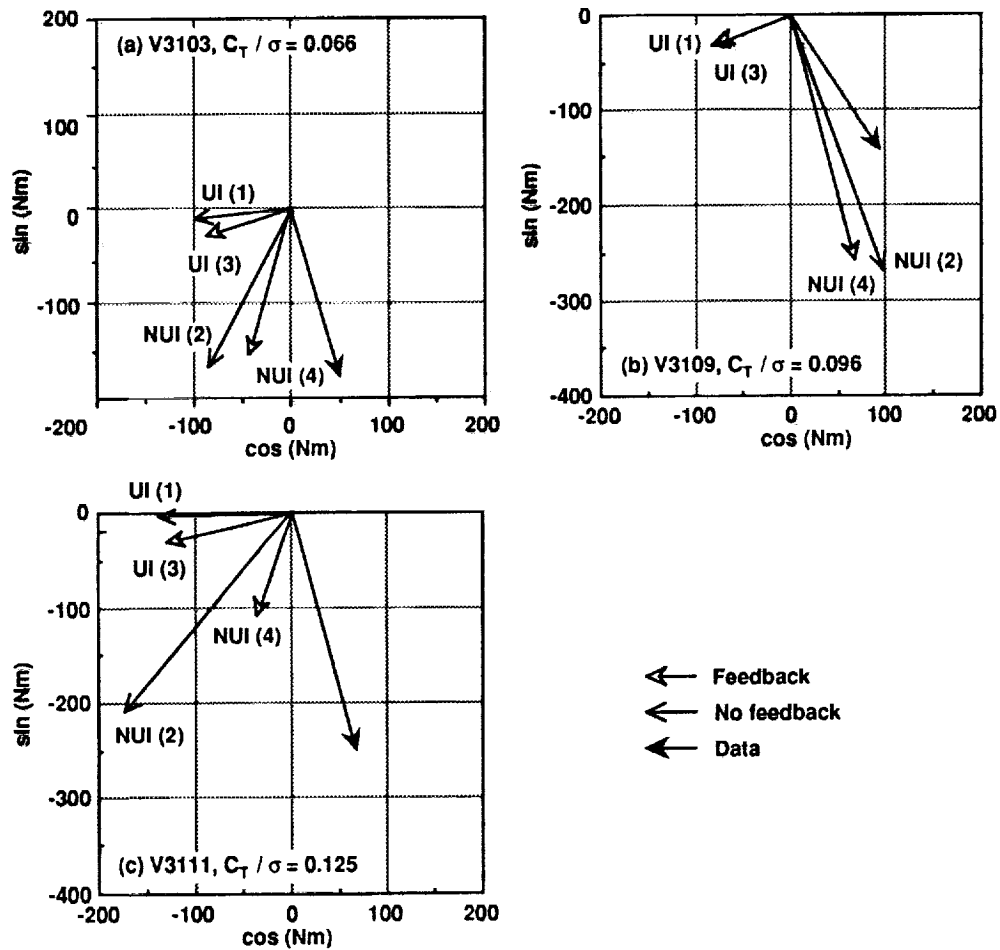


Figure 33. Magnitude and phase correlations of Q , the torque. Predictions were made using the SAMCEF model with uniform (UI) and nonuniform (NUI) inflow wake analyses (a free wake analysis (FW) was used for the lowest speed condition), both with and without feedback (see table 6), for the three constant speed conditions. a) $C_T/\sigma = 0.066$, b) $C_T/\sigma = 0.096$, c) $C_T/\sigma = 0.125$.

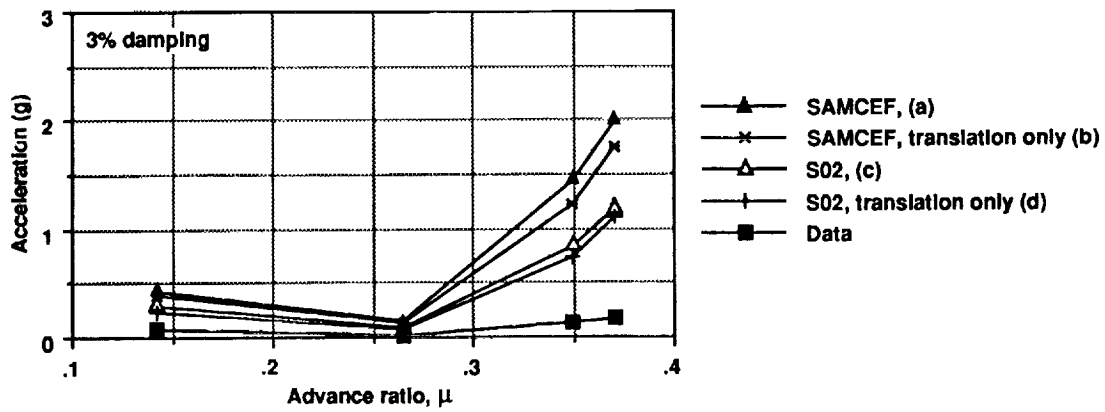


Figure 34. Correlation of measured and predicted acceleration. Magnitude only. Acceleration was predicted from the measured hub loads using the S02 and SAMCEF models in the forced response analysis. Letters in () indicate model configuration (see table 7).

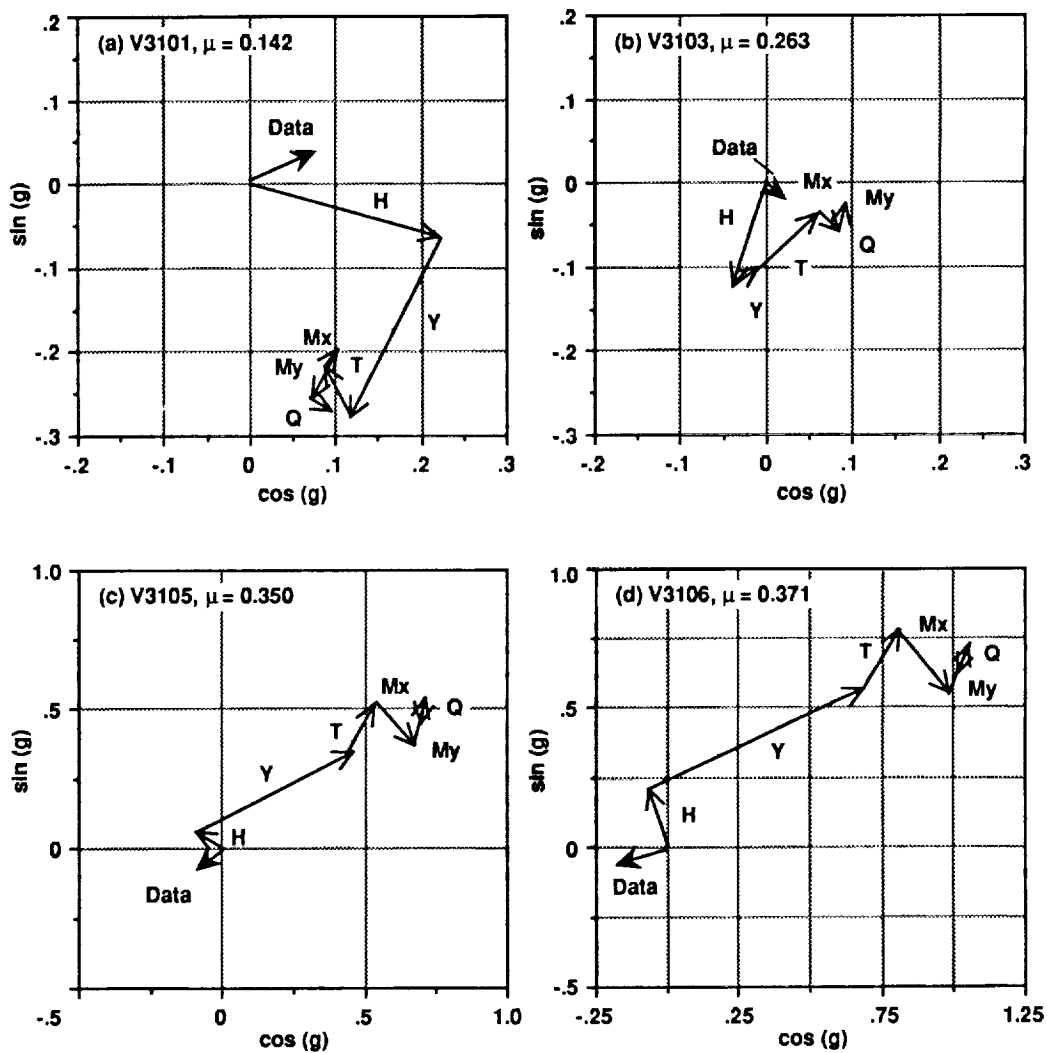


Figure 35. Magnitude and phase contributions of each measured hub load to the acceleration for the S02 model. a) $\mu = 0.14$, b) $\mu = 0.26$, c) $\mu = 0.35$, d) $\mu = 0.37$.

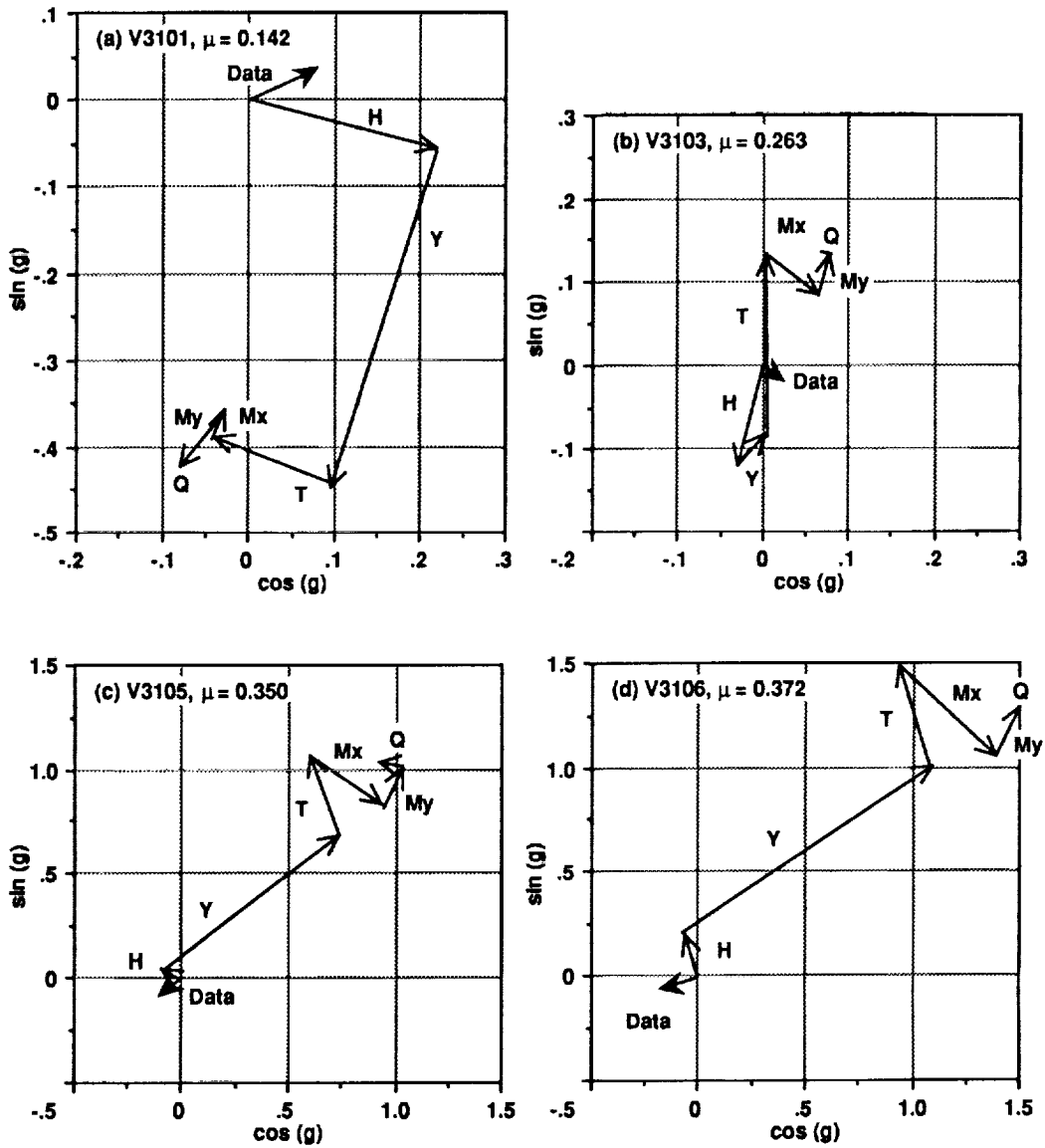


Figure 36. Magnitude and phase contributions of each measured hub load to the acceleration for the SAMCEF model. a) $\mu = 0.14$, b) $\mu = 0.26$, c) $\mu = 0.35$, d) $\mu = 0.37$.

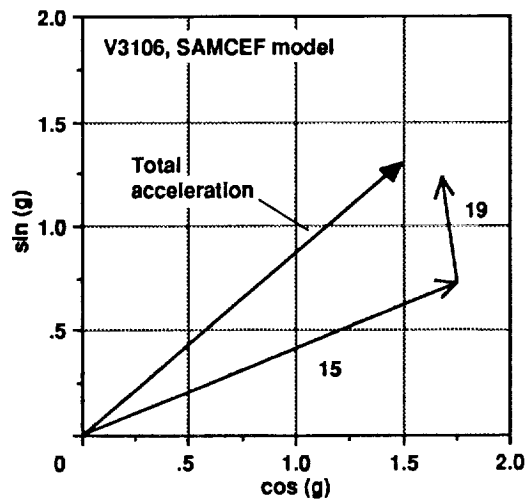


Figure 37. Contribution of the major modes to the acceleration predicted from the measured hub loads. Condition V3106.

V3106, SAMCEF model, effect of shifting the damping

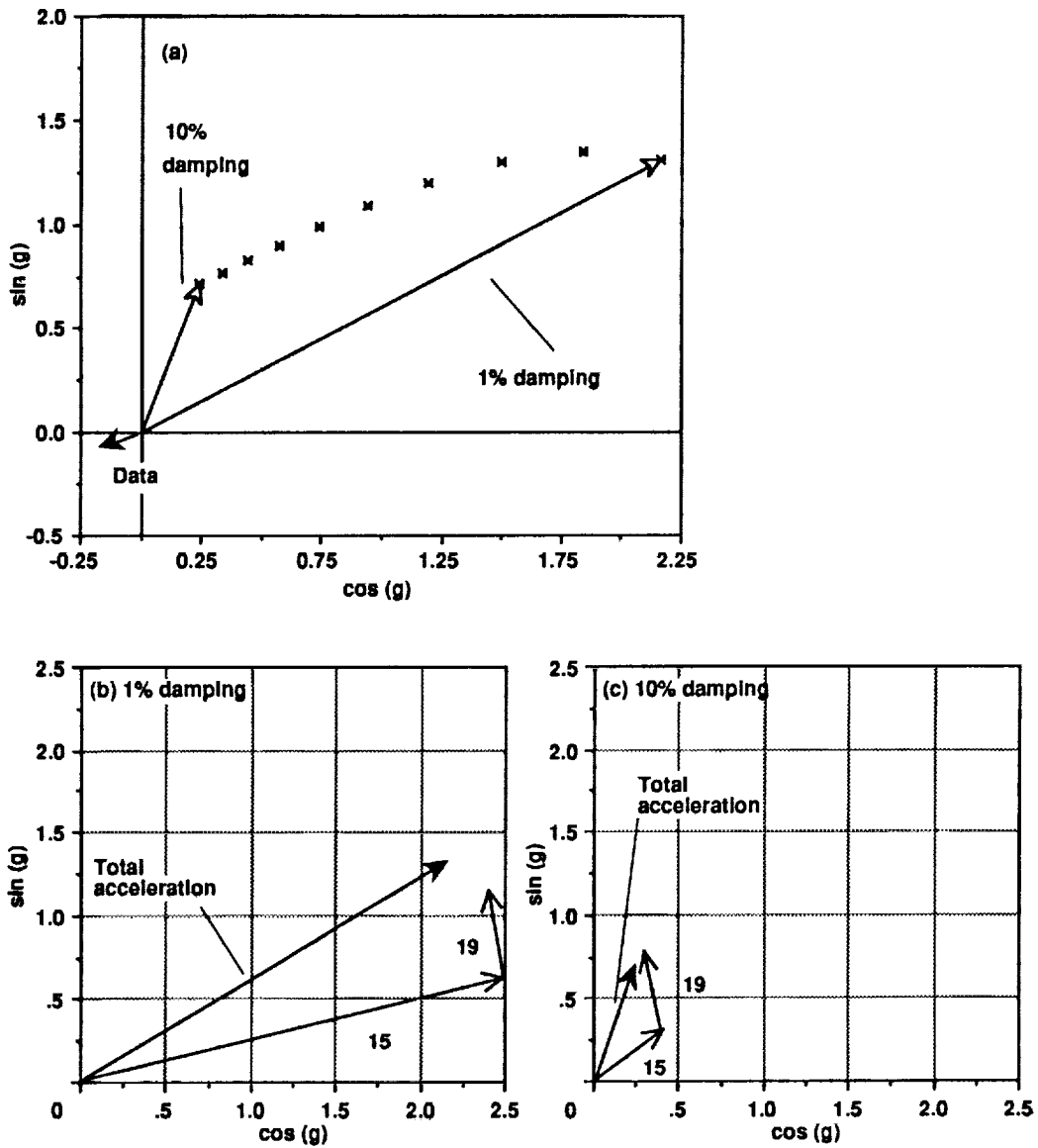


Figure 38. Effect on the acceleration predicted from measured hub loads of varying the damping from 1 to 10% critical. Condition V3106. a) Overall change in magnitude and direction, b) modal contributions for 1% damping, c) modal contributions for 10% damping.

V3106, SAMCEF model, effect of shifting the modal frequency.

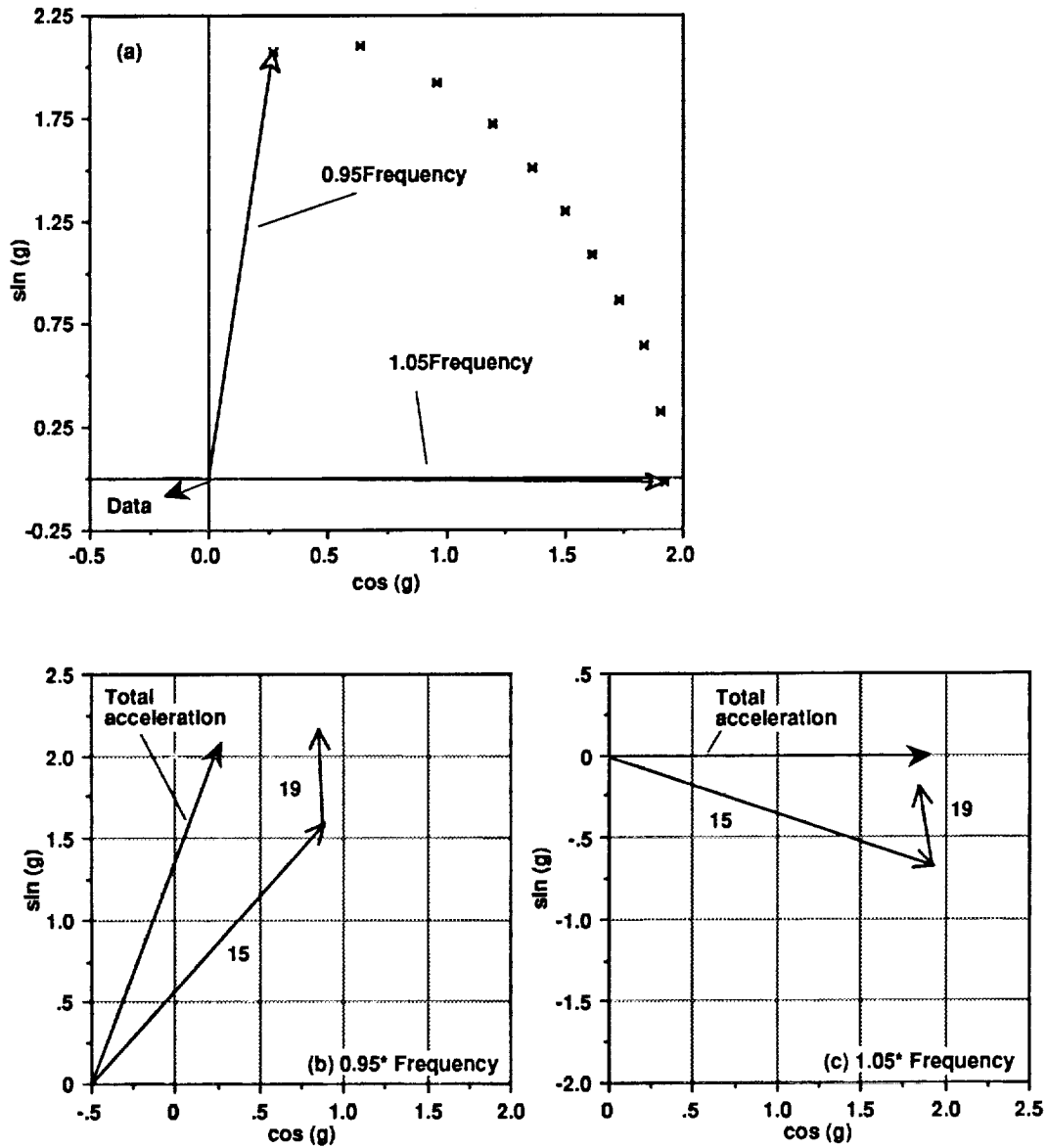


Figure 39. Effect on the acceleration predicted from measured hub loads of varying the frequencies from 95 to 105% of the baseline values. Condition V3106. a) Overall change in magnitude and direction, b) modal contributions for 95% frequencies, c) modal contributions for 105% frequencies.

V3106, SAMCEF model

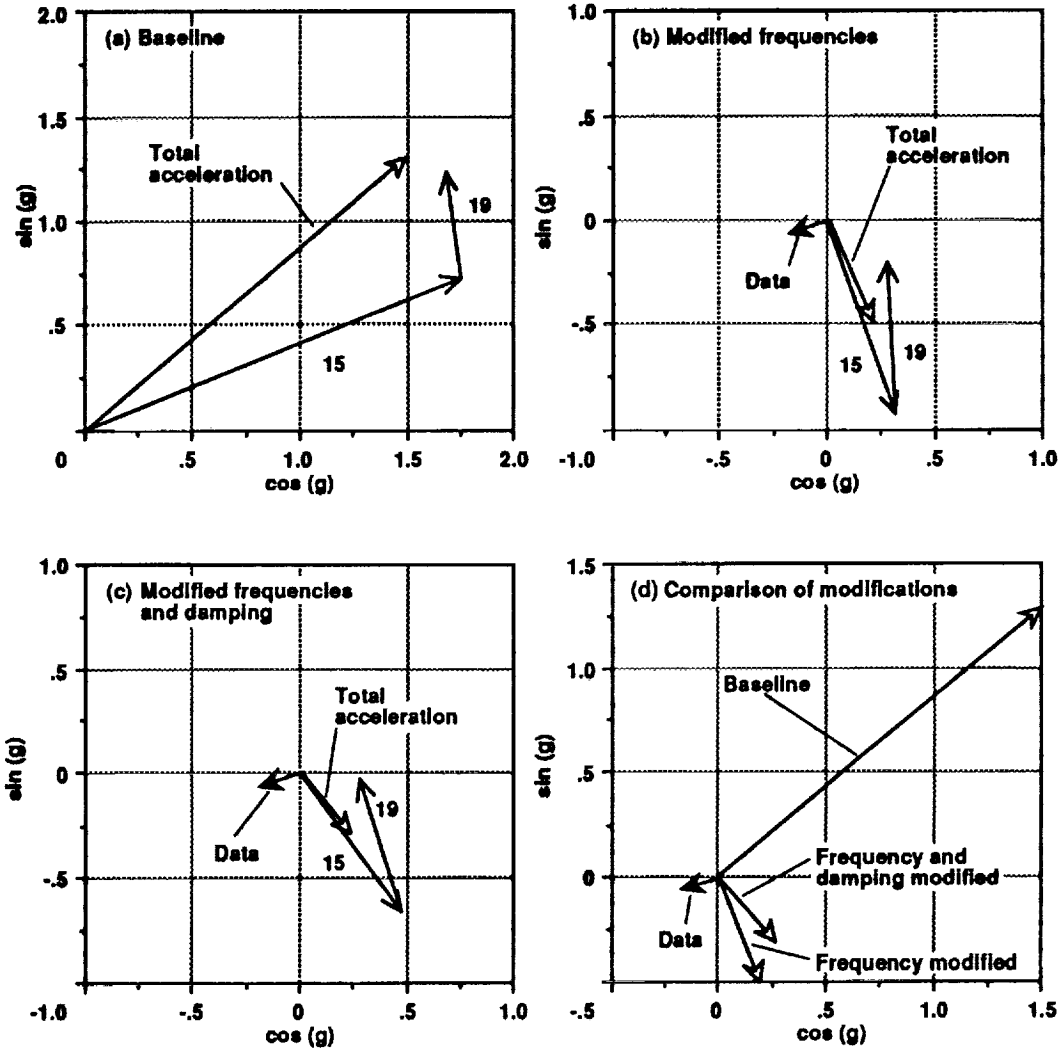


Figure 40. Effect on the acceleration predicted from the measured hub loads of strategically altering the finite element model. a) baseline acceleration, b) frequency modified, c) frequency and damping modified, d) total vectors for each step compared with the data. Condition V3106.

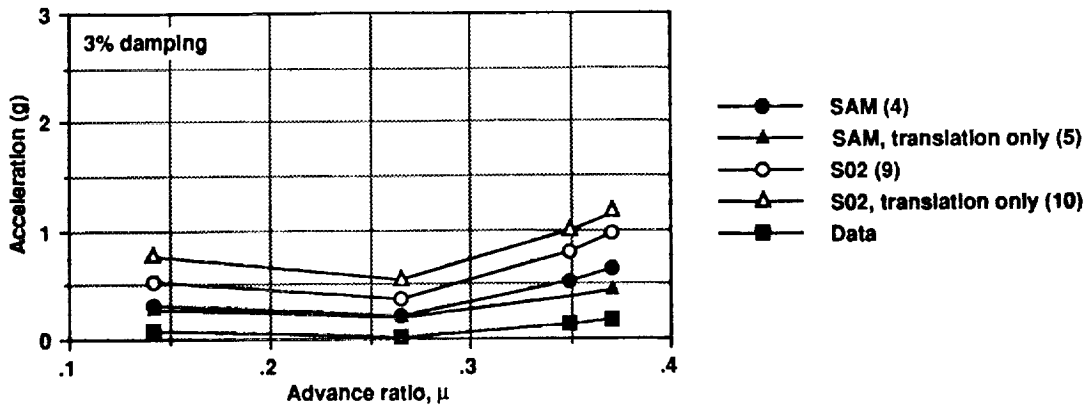


Figure 41. Correlation of measured and predicted acceleration. Magnitude only. Acceleration was predicted from the CAMRAD/JA hub loads using the S02 and SAMCEF models. Numbers in () indicate model configuration (see table 6).

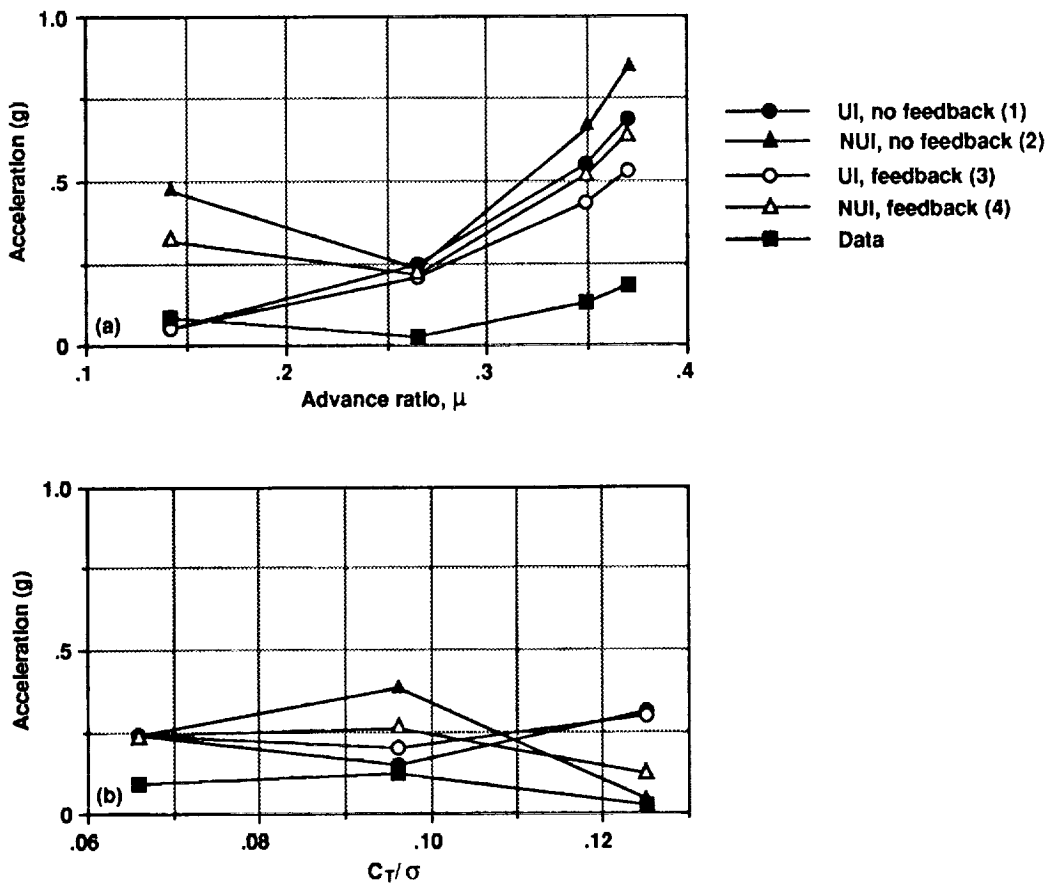


Figure 42. Correlation of measured and predicted acceleration. Magnitude only. Acceleration was predicted from the CAMRAD/JA hub loads using the SAMCEF model with and without feedback. a) speed sweep, b) thrust sweep. Numbers in () indicate model configuration (see table 6).

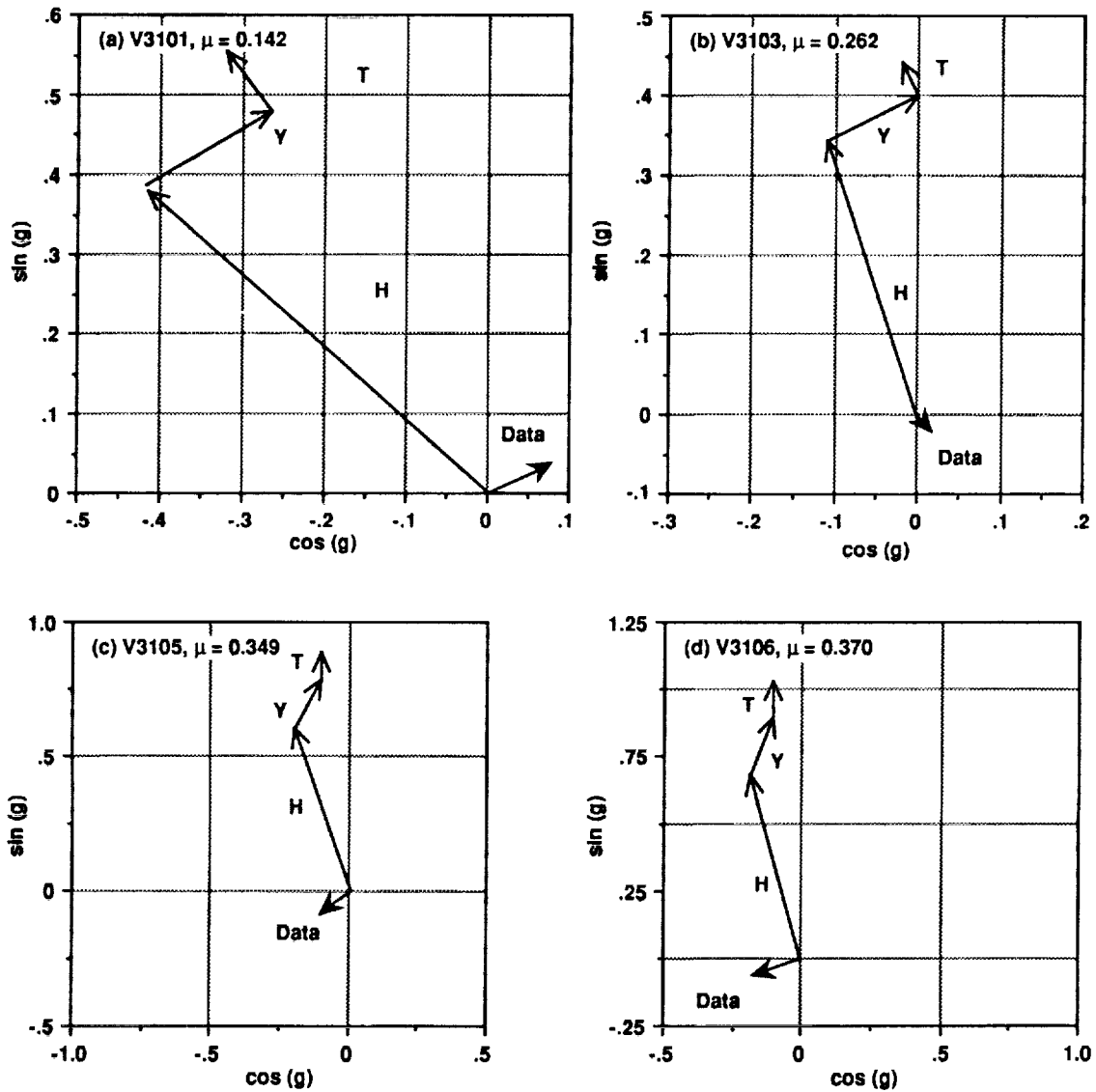


Figure 43. Magnitude and phase contributions of each calculated hub load (configuration 5 of Table 6) to the acceleration for the S02 model. a) $\mu = 0.14$, b) $\mu = 0.26$, c) $\mu = 0.35$, d) $\mu = 0.37$.

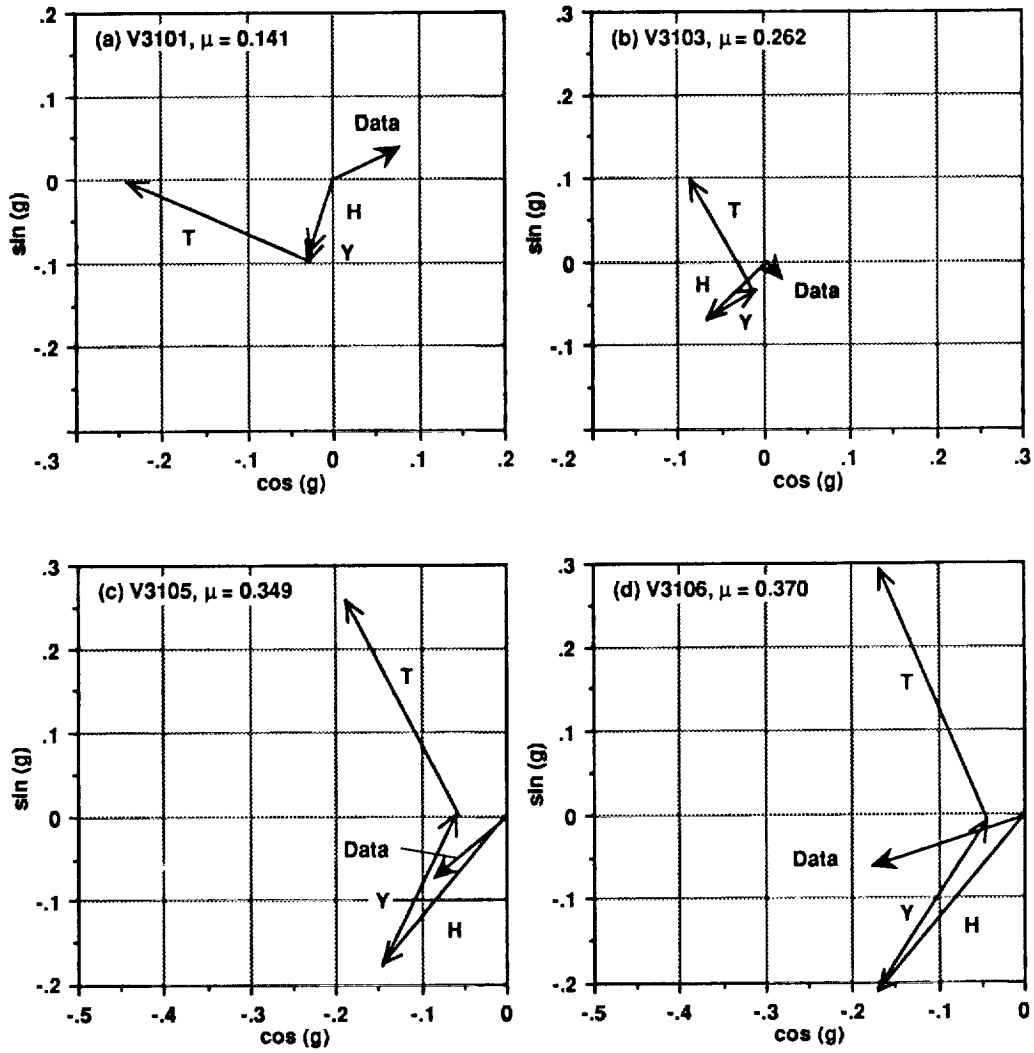


Figure 44. Magnitude and phase contributions of each calculated hub load (configuration 5 of Table 6) to the acceleration for the SAMCEF model. a) $\mu = 0.14$, b) $\mu = 0.26$, c) $\mu = 0.35$, d) $\mu = 0.37$.

V3106, SAMCEF model, effect of shifting the damping

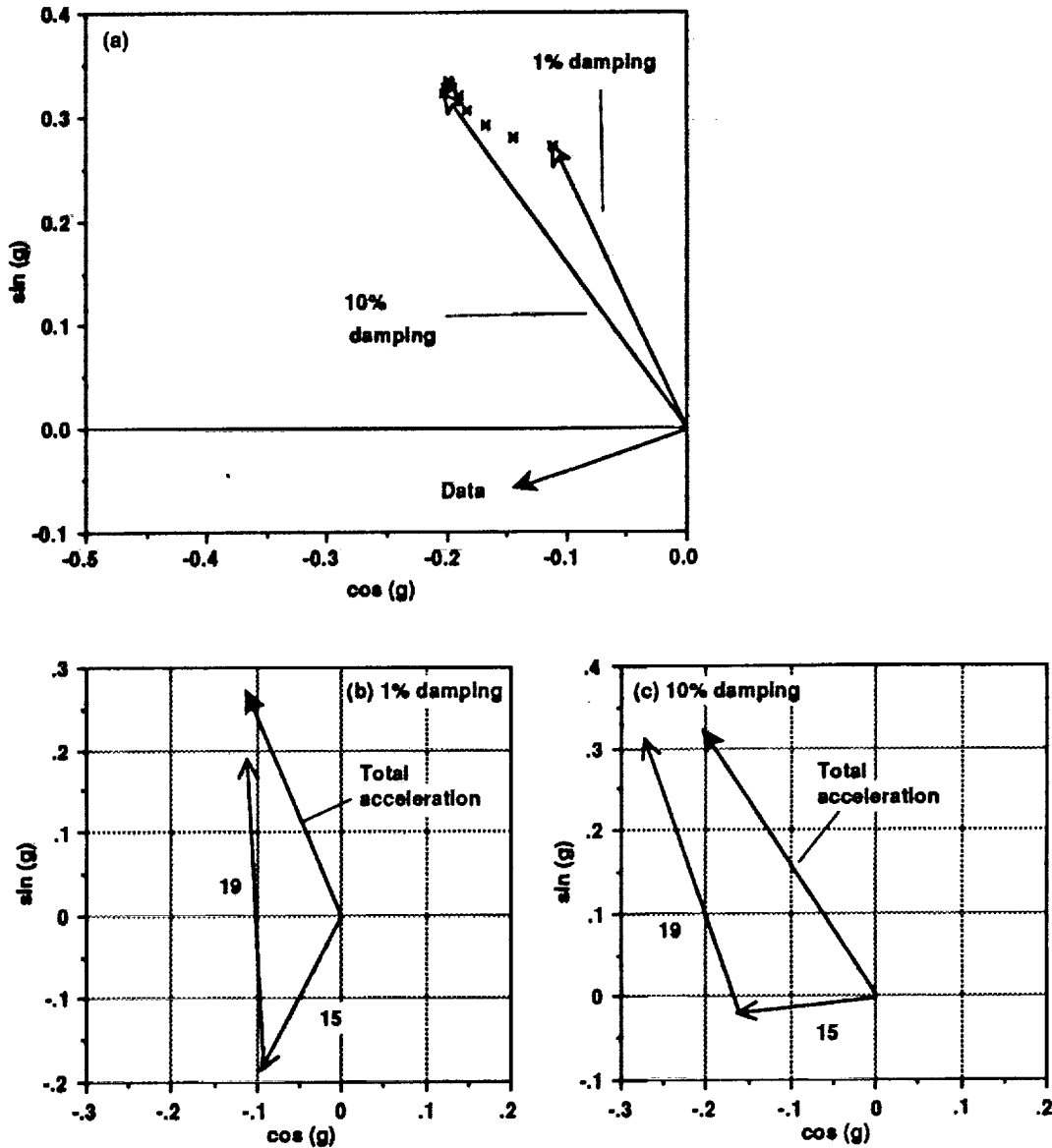


Figure 45. Effect on the acceleration predicted from CAMRAD/JA hub loads of varying the damping from 1 to 10% critical. Condition V3106. a) Overall change in magnitude and direction, b) modal contributions for 1% damping, c) modal contributions for 10% damping.

V3106, SAMCEF model, effect of shifting the modal frequency.

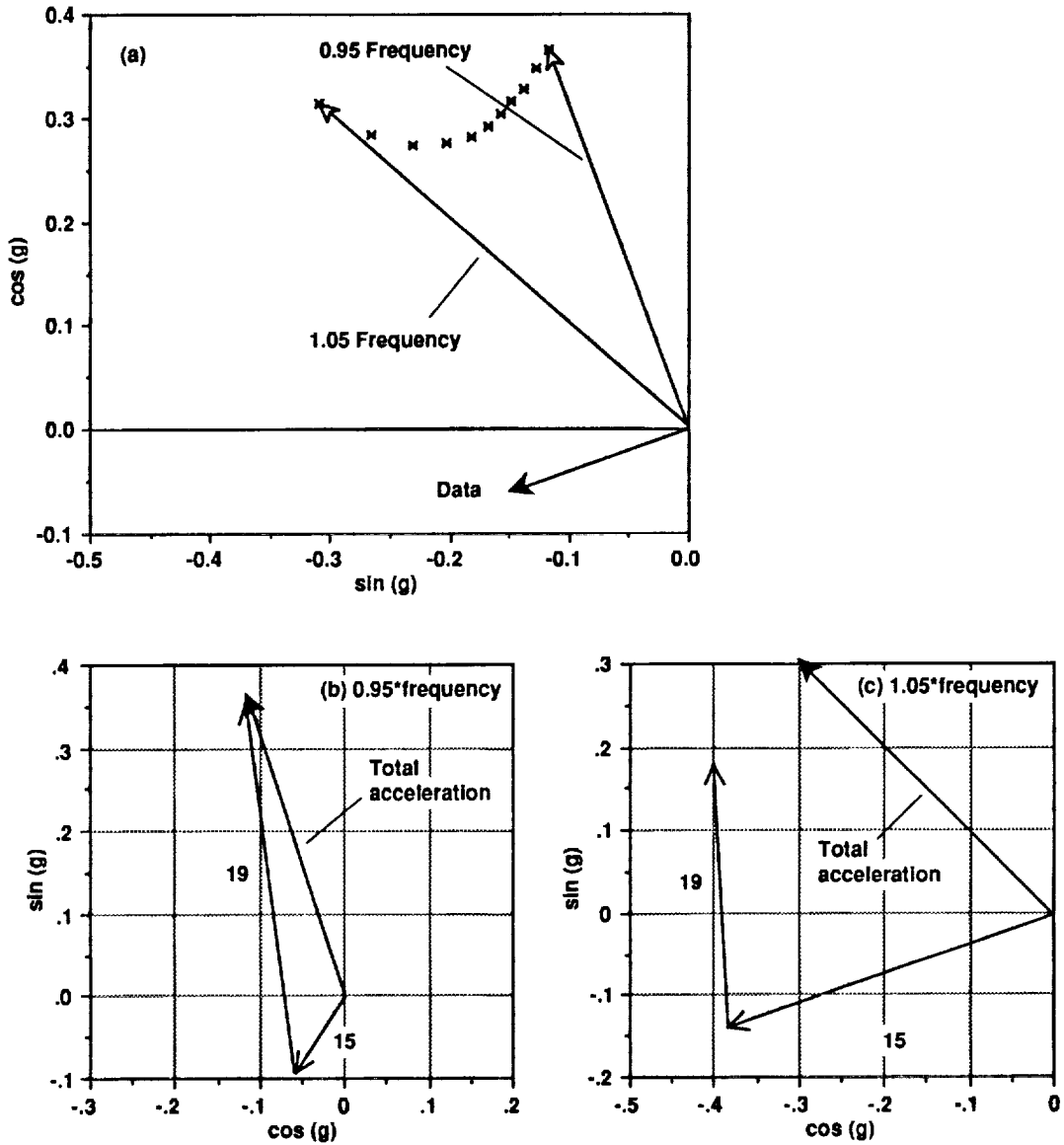


Figure 46. Effect on the acceleration predicted from CAMRAD/JA hub loads of varying the frequencies from 95 to 105% of the baseline values. Condition V3106. a) Overall change in magnitude and direction, b) modal contributions for 95% frequencies, c) modal contributions for 105% frequencies.

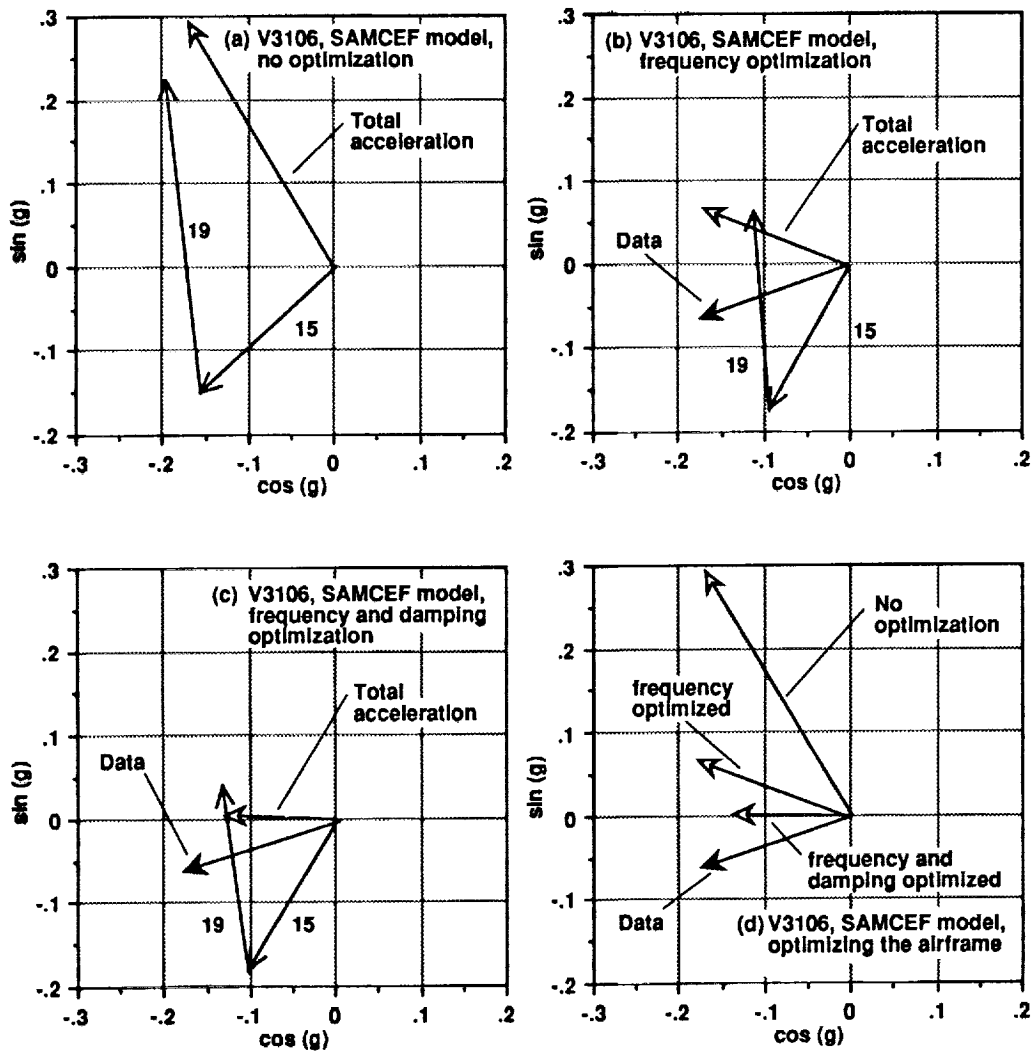


Figure 47. Effect on the acceleration predicted from the CAMRAD/JA hub loads of strategically altering the finite-element model. a) baseline acceleration, b) frequency optimized, c) frequency and damping optimized, d) total vectors for each step compared with the data. Condition V3106.

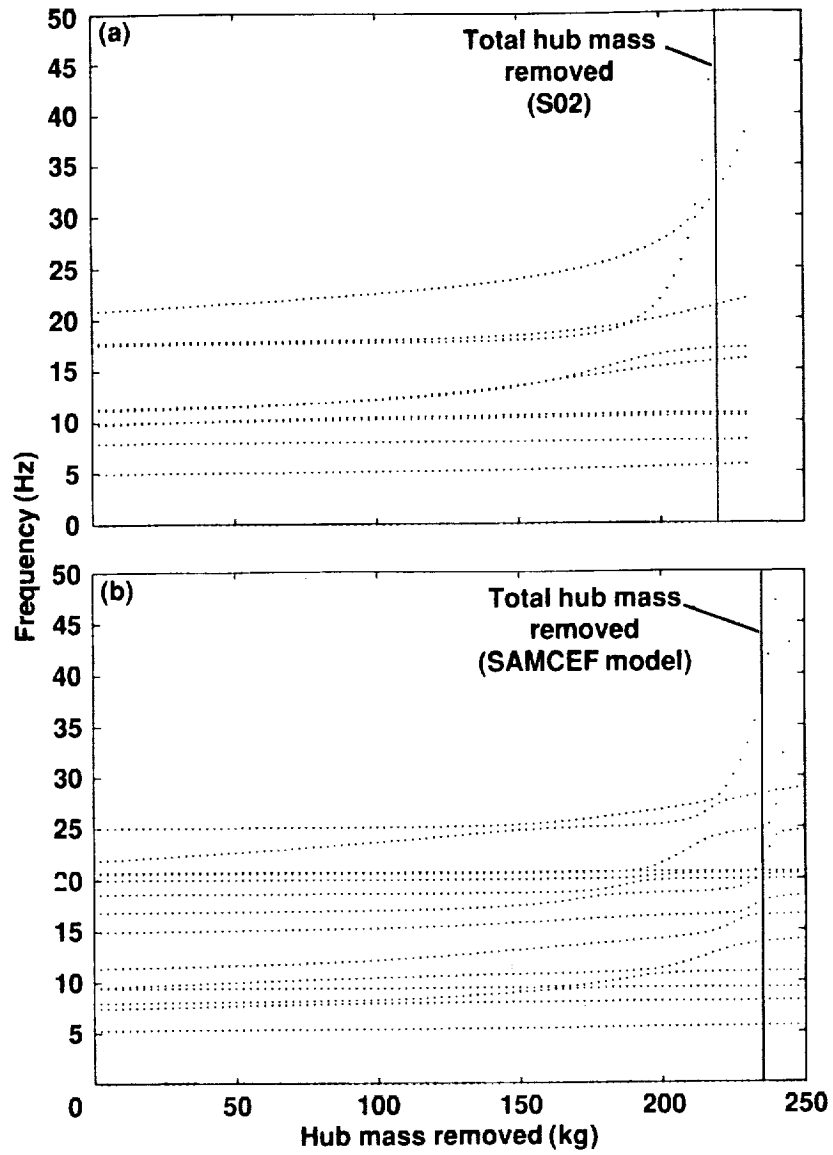


Figure A1. Effect on modal frequencies of reducing hub mass. a) Effect of removing hub mass from SO2 model, b) effect of removing hub mass from SAMCEF model.



Report Documentation Page

1. Report No. NASA TM-102794		2. Government Accession No.		3. Recipient's Catalog No.	
4. Title and Subtitle Vibration Analysis of the SA349/2 Helicopter			5. Report Date January 1991		
			6. Performing Organization Code		
7. Author(s) Ruth Heffernan, Dominique Precetti (Service Technique des Programmes Aéronautiques, Toulouse, France), and Wayne Johnson (Johnson Aeronautics, Palo Alto, California)			8. Performing Organization Report No. A-90083		
			10. Work Unit No. 505-61-51		
9. Performing Organization Name and Address Ames Research Center Moffett Field, CA 94035-1000			11. Contract or Grant No.		
			13. Type of Report and Period Covered Technical Memorandum		
12. Sponsoring Agency Name and Address National Aeronautics and Space Administration Washington, DC 20546-0001			14. Sponsoring Agency Code		
			15. Supplementary Notes Point of Contact: Ruth Heffernan, Ames Research Center, MS-T42, Moffett Field, CA 94035-1000 (415) 604-5043 or FTS 464-5043		
16. Abstract <p>Helicopter airframe vibration is examined using calculations and measurements for the SA349/2 research helicopter. The hub loads, which transmit excitations to the fuselage, are predicted using a comprehensive rotorcraft analysis and correlated with measured hub loads. The predicted and measured hub loads are then coupled with finite element models representing the SA349/2 fuselage. The resulting vertical acceleration at the pilot seat is examined. Adjustments are made to the airframe structural models to examine the sensitivity of predicted vertical acceleration to the model. Changes of a few percent to the damping and frequency of specific modes lead to large reductions in predicted vibration and to major improvements in the correlations with measured pilot-seat vertical acceleration.</p>					
17. Key Words (Suggested by Author(s)) Vibration Rotorcraft Airframe structural model			18. Distribution Statement Unclassified-Unlimited Subject Category - 01		
19. Security Classif. (of this report) Unclassified		20. Security Classif. (of this page) Unclassified		21. No. of Pages 102	22. Price A06